PREPARATION, CHARACTERIZATION, SOLID STATE AND CATALYTIC STUDIES ON SELECTED PEROVSKITES AND MIXED METAL OXIDES

THESIS

Submitted to the

GOA UNIVERSITY

For the degree of

DOCTOR OF PHILOSOPHY

IN

CHEMISTRY

By

RAMCHANDRA G. SHETKAR

Department of Chemistry

Goa University

GOA 403206

April 2007

(R. G. Shetkar)

(Dr C. V. V. Satyanarayana
NCL - Pune

DECLARATION

I, Mr. Ramchandra G. Shetkar, hereby declare that this thesis entitled "Preparation, Characterization, Solid state and Catalytic studies on selected perovskites and mixed metal oxides" for the degree of Doctor of Philosophy in chemistry, is the outcome of my own study undertaken under the guidance of Dr. A.V. Salker, Department of Chemistry, Goa University. It has not previously formed the basis for the award of any degree, diploma or certificate of this or any other University. I have duly acknowledged all the sources used by me in the preparation of this thesis.
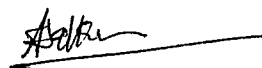
Date: 12 · 04 · 2007

Place: Taleigao – plateau
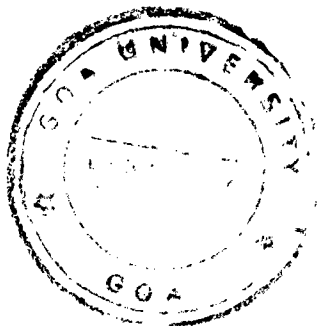
Ramchandra G. Shetkar

(Candidate)

CERTIFICATE

This is to certify that the thesis entitled "Preparation, Characterization, Solid state and Catalytic studies on selected perovskites and mixed metal oxides" submitted by the candidate Shri Ramchandra G. Shetkar, for the award of the degree of Doctor of Philosophy in Chemistry is based on the literature survey / laboratory experiments carried out by him during the period of study under my guidance. I further state that the research work presented in the thesis has been carried out independently by him and due acknowledgement has been made whenever outside facilities has been availed of.

Date: 12·04·2007

Dr. A.V. Salker,

Research Guide,

Department of Chemistry,

Goa University.

ACKNOWLEDGEMENT

CONTENTS

CHAPTER					page no

CHAPTER 1

INTRODUCTION

INTRODUCTION

For the last several decades, the field of transition metal oxides (TMO) and mixed metal oxides has served as a source of interesting and challenging research problems to technologists, chemists and material scientists[1]. Transition metal oxides constitute the most fascinating class of materials, exhibiting a variety of structures and properties[2]. TMO have become an area of active research for catalytic studies and efforts are being made to replace the conventional noble metal catalysts by oxide catalysts[3-5] which are equally efficient, thermally stable and economical.

Most of the environmental pollution is caused due to the combustion of fossil fuels giving out toxic gases causing serious global problems. Automobiles, factories and industrial exhausts contain harmful gases such as carbon monoxide (CO), low weight hydrocarbons, nitrogen oxides (NOx) etc. It is essential to catalyze their conversions into non toxic products[6-7]. CO oxidation study has a long history. This reaction is essential in terms of practical importance and as a model reaction. It is associated with the reduction of atmospheric pollution.

There is a growing demand for pollution control catalysts which should be viable, more effective, stable and economical. Complex oxides containing two or

more cations have attracted the attention in recent times because of their growing demands in variety of technological and scientific fields. These are used in many heterogeneous oxidation catalysis reactions and found to be active in oxidation-reduction reactions without poisoning. There is an appearance of new phase of ternary oxides identified as perovskites and spinels above certain critical concentrations of the active metal ions[8]. The study of catalytic activity of these perovskites and spinel phases showed that they are better catalysts in regards of their activity and stability as compared with individual oxides[9-11].

The perovskite type mixed oxides (ABO_3) occupy a prominent place under all the known ternary systems[12]. These materials have well defined bulk structures, and the compositions of cations at both A and B sites can be variously changed[13]. Therefore these mixed oxides are suitable materials for the study of structure-property relationship.

An important feature of rare earth perovskites is the possibility of varying the dimensions of unit cell by changing the A-site or B-site ions by different metal ions, which make them to behave as chemical chameleons[14] with a wide variety of solid state and catalytic properties. The rare earth and transition metal oxidic perovskites are found to be good catalysts for several oxidation reactions. Some perovskite compositions with rare earth and first row transition series metals show a high catalytic activity for total oxidation of CO[15-16]. Moreover their activities are not significantly affected by poisons like Pb and S present in automotive exhaust gases, thus making these materials as promising anti contamination catalysts[17-18].

Following Wolkenstein's theory of catalysis[19], there is a growing awareness of the role of solid state properties in the catalytic phenomena. Since then many correlations of catalytic activity with defects in solids, electrical and magnetic properties have appeared in literature[20-24]. The knowledge of the relation between the catalytic and solid state properties of catalysts is crucial for systematic design of efficient preparations.

Ternary oxides chosen in the present investigation are series of perovskite systems. The stable structure of the perovskites has attracted the attention in the study of structure and electronic factors in catalysis. The structures of these oxides are flexible and many metal ions with variable valency can be incorporated in them. Many perovskites find potential applications such as thermoelectric, ceramic, magnetic material, electrode for fuel cells, host for laser systems and gas sensor in addition to being good catalysts[2, 25-29]. Therefore a great concern through research is devoted to these properties to understand and extrapolate the obtained data to design new materials to suit the specific purposes. The perovskite oxides have distinct structural features which play vital role in determining their magnetic, electrical as well as catalytic properties. The study of these systems is much useful in understanding the technological and fundamental aspects to provide a rational basis for catalyst selection.

A series of perovskite compounds containing first row transition metals and supported transition metal oxides discussed in this investigations are prepared by co-precipitation technique in order to achieve homogeneity and low temperature

formation with more surface areas, unlike ceramic method which require high temperature for their formation leading to the loss of surface area. A series of perovskites with rare earths is also prepared by combustion method for the comparative account of properties and catalytic activity. In the present investigations attempts are made to study the catalytic CO oxidation on these compositions with respect to activity, selectivity, catalyst life, stability, kinetics and solid state properties.

The present investigation includes:

1. Preparation of series of perovskites and supported metal oxides such as

   (i) $Zn_{1-x}Ni_xMnO_3$, (Where x = 0.0, 0.2, 0.4, 0.6, 0.8 and 1.0)

   (ii) (a) $SrMnO_3$ (b) $SmMnO_3$ (c) $NdMnO_3$ (d) $BaCeO_3$ and (e) $ZnSnO_3$,

   (iii) Fe_2O_3/ZnO (Where Fe_2O_3 = 0%, 5%, 10%, 20% and 100%) and

   (iv) NiO/ZnO (Where NiO = 0%, 5%, 10%, 20% and 100%).

2. Characterization of the compositions by different techniques such as X-ray powder diffraction (XRD), Vibrational spectroscopy (FTIR), Atomic absorption spectroscopy (AAS), B.E.T. Surface area measurement and Thermal analysis (TGA/DSC) were done.

3. Studies of solid state and spectroscopic properties such as Electrical resistivity, Magnetic susceptibility, Electron spin resonance (ESR), Scanning electron microscopy (SEM) and Diffuse reflectance spectroscopy (DRS) were recorded.

4. Study of temperature dependent CO conversion efficiency and kinetic parameters over the catalysts were undertaken.

5. Study of CO oxidation cycles and catalyst life of the prepared compositions.

6. Identification of the various factors such as valency of cations, oxygen non-stoichiometry, binding energy, tolerance factor, surface area, structure and solid state properties contributing to the observed catalytic activity of the different compounds were attempted.

CHAPTER 2

REVIEW OF LITERATURE

REVIEW OF LITERATURE

Among all the known ternary systems of compositions, perovskites (ABO$_3$) containing transition metals and rare earth metals ions occupy a prominent place. This is because of their wide occurrence and series of interesting and useful properties associated with their structures. Due to the increasing technical importance of these perovskite type materials, a number of books, monographs and review articles on different aspects of their properties and structural characteristics have been published in recent years[30-36].

In this chapter it is aimed to bring together the diverse data about the aspects like structural, electrical, magnetic and catalytic properties of the perovskite oxides that is relevant to the present investigation.

2.1 METAL OXIDES AND MIXED METAL OXIDES

Transition metal oxides (TMO) and mixed metal oxides possess interesting material properties. These have become an area of active research for solid state and the catalysts used to eliminate the atmospheric pollution. Different authors have studied the transition metal oxides in the supported or mixed forms for their catalyzing actions on CO oxidation reaction. Mergler et. al.[37] have reported the CO

oxidation by O_2 over platinum catalyst promoted by MnO_x and CoO_x oxides. Yao and Kummer[38] studied the catalytic oxidation of CO, C_2H_4, C_2H_6, C_3H_6 and C_3H_8 using NiO micro crystals, exposing predominantly their (111) face as the catalyst. Laitao et. al.[7] used successfully a series of $LaSrCo_{0.9}B'_{0.1}O_4$ (B' = Mn, Fe, Ni, Cu) mixed oxides for CO and C_3H_8 oxidation and found that the specific effects of B' ions on CO and C_3H_8 oxidation depend on their category. Shapovalov and Metiu[39] reported that in CO oxidation, doping of CeO_2 with Au allows the oxide to react readily with CO.

2.2 THE PEROVSKITES

Perovskites are named after the mineral $CaTiO_3$ that was first identified and described by the famous Russian mineralogist Count Lev Aleksevich Van Perovski in 1830 and named by the geologist Gustav Rose. The name perovskite was retained for the idealized cubic structure. The rare mineral $CaTiO_3$, which was thought of having simple cubic structure, was later on demonstrated as of pseudo - cubic type and its real structure is orthorhombic[40]. Hundreds of materials of stoichiometry ABO_3 adopt the perovskite structure or a slightly distorted version. In the notation ABO_3, the A cation is conventionally larger of the two.

2.2.1 The ideal perovskite structure

The crystal structure of all ABO_3 perovskites consists of essentially close packed layers of stoichiometry AO_3 with the transition metal ion (B) occupying
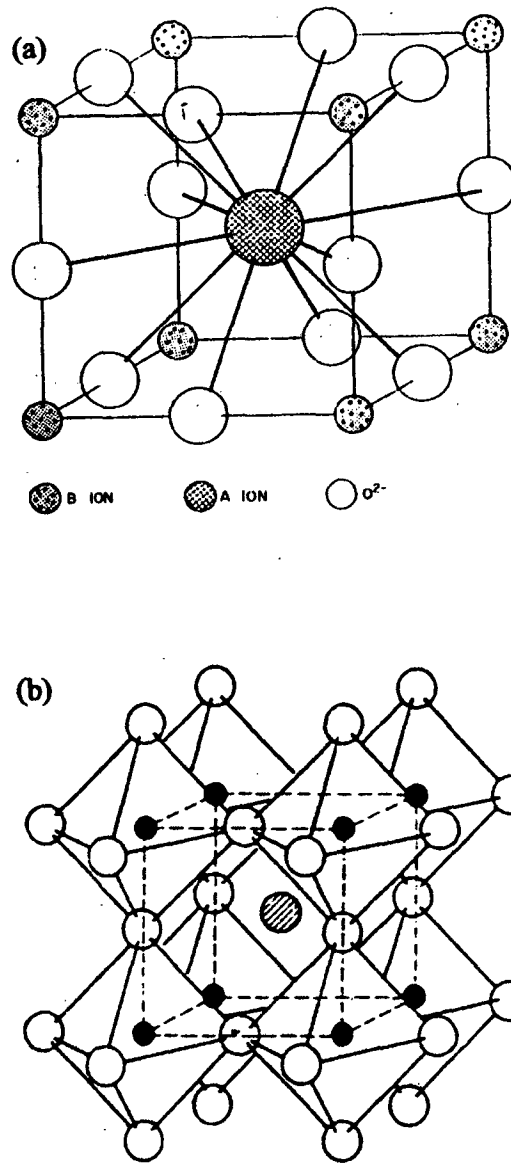
Fig. 2.1 The Perovskite structure ABO_3 with one formula unit:
(a) A ion coordinated by twelve oxygen ions. (b) Oxygen ions
belong to eight BO_6 octahedra sharing corners.

8

octahedral holes between the layers. Successive AO_3 sheets can be stacked in either hcp or ccp arrangements, and several mixed stackings are possible.

The consequence of this for the B-site cations is that their coordination octahedra can be linked by either corner sharing or face sharing. Only corner sharing is present in $CaTiO_3$ whereas face sharing is present in $BaMnO_3$[41]. Fig. 2.1 (a) shows the crystal structure of a simple perovskite with one formula unit ABO_3 with the A ion coordinated by twelve oxygen ions which in turn belongs to eight BO_6 octahedra sharing corners as shown in fig. 2.1 (b). This leads to a cubic structure with B cations at the corners and the oxygen anions framed at the centre of edges. The stability is achieved primarily from the Madelung energy of the stacking of rigid BO_6 octahedra. This suggests that B-cation should have a preference for octahedral coordination. The A ion occupying the larger dodecahedral interstices should have an appropriate size. The edge of the simple cube is approximately 4 A°.

Thus the characteristics of a perovskite oxide structure are (1) the total charge of A and B cations is six, (2) a dodecahedral stable A ion, (3) an octahedral coordinated B ion and (4) corner shared octahedral BO_3 sub array.

2.2.2 Stoichiometric aspects

On the basis of cation valencies, for simple ABO_3 oxide systems the following classification can be made:

$[1+5] = A^I B^V O_3$; $[2+4] = A^{II} B^{IV} O_3$; $[3+3] = A^{III} B^{III} O_3$. These three types alone cover a large range of compounds. Goodenough and Longo[32] listed approximately 300 of

such perovskites giving detailed crystallographic and magnetic data. When mixed cation structures of the type $(AA')(BB')O_3$; $A_2(BB')O_3$; $A_3B_2B'O_9$; $A(B_xB'_yB''_z)O_3$ etc. are considered, a great number of other possibilities arises.

2.2.3 Polymorphism

A number of perovskite like materials show several polymorphic modifications. Some of these are very important in relation to their applications and physical properties. For example in $BaTiO_3$ and $KNbO_3$ the following transformations are observed with increasing temperature:

Rhombohedral $\leftrightarrow$ orthorhombic $\leftrightarrow$ tetragonal $\leftrightarrow$ cubic.

These phase changes are reversible and all the polymorphic forms possess a pseudo-cubic unit cell with edge of 4 A°. Fig. 2.2 (a) show the perovskite structure ABO_3 where in the axis of primitive rhombohedral cell are indicated and the comparison drawn in a nondistorted perovskite structure of the orthorhombic and the rhombohedral unit cell are shown in fig. 2.2 (b).

The O ions in the orthorhombic structure are found to be in a position mostly favourable to rhombohedral transition and also at high temperatures, orthorhombic structure may be initially transformed to rhombohedral and then to the ideal cubic structure. Phase transformations observed in $LaMnO_3$[42], with the rise in temperature is from orthorhombic $\leftrightarrow$ cubic at around 327°C and cubic $\leftrightarrow$ rhombohedral at 527°C. Wold et el[43] also reported orthorhombic $\leftrightarrow$ rhombohedral transition in $LaMnO_3$.

(a)

—————— = Perovskite sub-cell   ◐ - A

— — — = Orthorhombic   ○ - B

- - - - - = Rhombohedral   ● - O

(b)
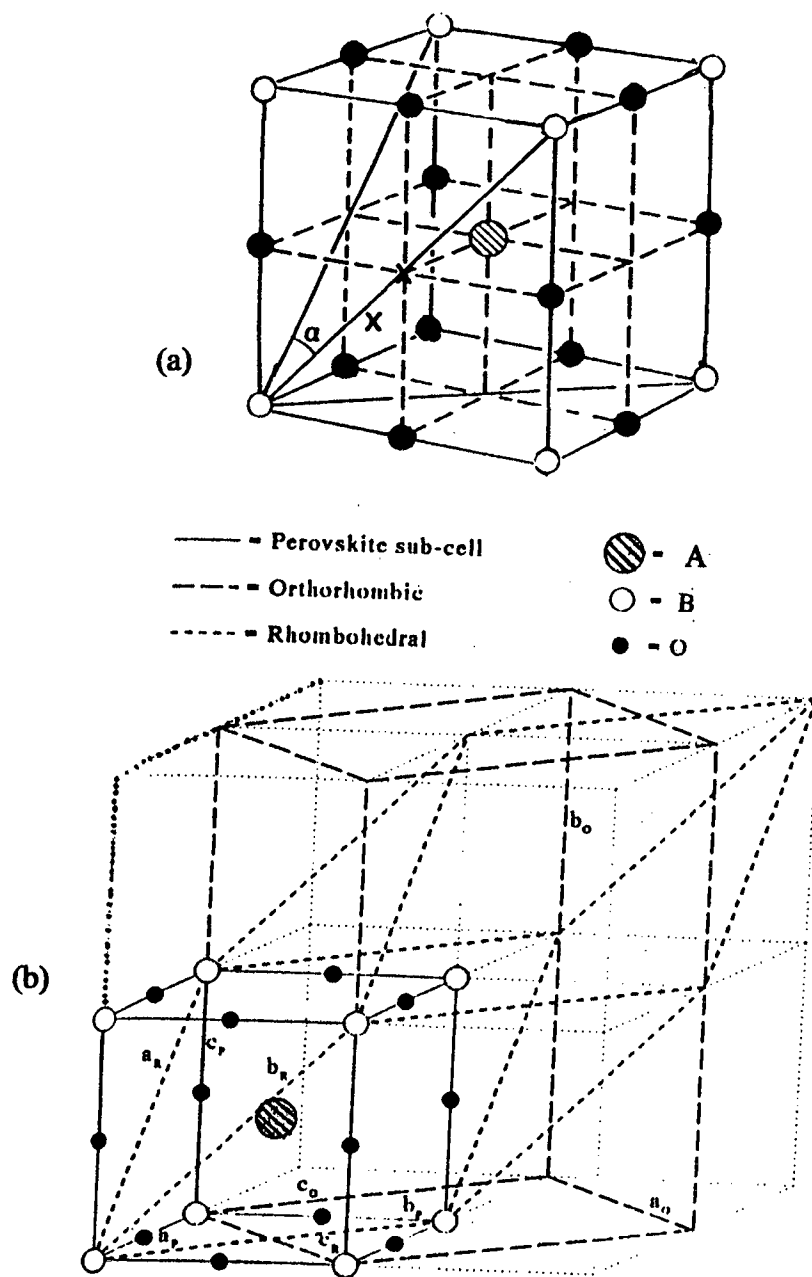
Fig. 2.2   a) The Perovskite structure ABO_3 wherein the axis of primitive rhombohedral cell are indicated. (b) Comparison of the orthorhombic and rhombohedral unit cell, drawn in a nondistorted perovskite structure.

Geller[44]showed that only a very few orthorhombic compounds may actually be transformed into rhombohedral and also a very few of rhombohedral can get transformed to a cubic phase at high temperatures.

2.2.4 Defect perovskites

Defects in perovskite compositions can arise from cation deficiency in the A or B sites as well as from oxygen deficiency. The subject has been nicely reviewed in brief in a recent book of Rao and Gopalakrishnan[45].

2.2.5 Distorted perovskites

When cationic radii in perovskite compositions deviate from the requisite values there is a distortion in the ideal cubic structure of the compositions. If the cation is too large for a dodecahedral void, for the optimization of B-O bond length a distortion to a hexagonal stacking with face shared octahedral is favoured. The unstable twelve-fold coordination reduces to lower coordination if the cation A is too small. The ionic size effect on the structures is the main reason why the anions preferred for the perovskite formation are oxides and fluorides and not chlorides or sulfides. The larger radii require much larger A site cations. So that usually they form layered structured compounds when the A cations are missing.

The atomic displacements in the structures along the cube axis, face diagonal or cube diagonal might resort to tetragonally, orthorhombically and rhombohedrally modified crystal structures respectively. Geller[46] pointed out that orthorhombic and rhombohedral modifications are observed to be common in the perovskites as shown

in fig. 2.2. Both the types involve the rotation of BO_6 octahedra occurring to different extents. The metal-oxygen bond can vary from highly ionic to covalent or metallic.

2.2.5.1 Orthorhombic perovskites

The first identified orthorhombically distorted perovskite is $GdFeO_3$ [47]. In this structure, FeO_6- octahedra are tilted and distorted. GdO_{12}- polyhedron is also distorted, showing (8+4) coordination. A large number of rare earth compounds exhibiting orthorhombic distorted structure[36] are $LnRhO_3$, $LnCrO_3$, $LnFeO_3$, $LnGaO_3$, $LnMnO_3$ etc.

2.2.5.2 Rhombohedral perovskites

Examples of rhombohedral perovskites are $LaAlO_3$, $LaNiO_3$ and $LaCoO_3$. In these compositions, cubic cell show a small deformation to rhombohedral symmetry. If this deformation does not enlarge unit cell, it is possible to index it on a unit cell containing either one or two formula units with rhombohedral angles $\alpha \sim 90°$ or $\alpha \sim 60°$ respectively. However, the anions that are generally displaced require the larger unit cell with $\alpha \sim 60°$.

At room temperature $LaCoO_3$ has rhombohedral structure. It undergoes two interesting phase transitions[48] transforming to another rhombohedral phases, in which trivalent cobalt is ordered in such a way that there are alternating (111) planes with high spin and low spin $Co^{(III)}$ ions. A second phase transition occurs at above 937°C, in which α-angle drops abruptly from 60.4° to 60.0°.

2.2.5.3 Tetragonal perovskites

The best-known example of a tetragonal perovskite is probably the room temperature form of $BaTiO_3$. In this composition barium is coordinated by four oxygen ions at 2.80 A°, four at 2.83 A° and four at 2.88A°. The TiO_6 - octahedra of the structure shows distortions.

2.2.5.4 Monoclinic and triclinic perovskites

Monoclinic and triclinic unit cells have been reported in several cases. $AgCuF_3$ and $CsPbl_3$ are the examples of monoclinic perovskites where as $BiMnO_3$ and $BiScO_3$ are triclinic perovskites.

2.2.5.5 Origin of distortion

It is a fact that a small fraction of ABO_3 oxide compositions stabilize in the ideal perovskite structure. Besides the relative ionic radii effect, other factors like covalency, Jahn-Teller effect, ordering of localized and collective electrons, ordering of B cations and the commonly prevalent nonstoichiometry also contribute to the distortion of cubic structure.

a) Ionic size effect

In lanthanide series, the ionic radius of Ln^{3+} decreases with the increase in atomic number due to lanthanide contraction. Marezio[49] reported an increasing distortion of an ideal cubic perovskite with the decreasing ionic radius, as also reported by Demazeau[50] for $LnNiO_3$ and Baiker[51] for $LnFeO_3$. Obayashi and Kudo[52]

have illustrated the importance of ionic size for the perovskite formation in the study of $M_xLn_{1-x}CoO_3$ series (where Ln stands for lanthanide ion and M for alkaline earth ions). $LaCoO_3$ shows a rhombohedral structure. Substitution of La^{3+} by smaller Ca^{2+} ions retains the perovskite structure up to a substitution of $x = 0.7$. In the lanthanide series the radii of lanthanide ion themselves decrease due to lanthanide contraction. The substitution by the smaller Ca^{2+} ions considerably decreases the effective radii of the A site. This additional decrease in the radii with the substitution of the smaller Ca^{2+} ions lowers the radii of A site below the limit of perovskite structure stabilization, such that Gd^{3+} and higher lanthanides do not form compounds with perovskite structure on Ca ion substitution. However, substitution by bigger Ba^{2+} ion out beats the lanthanide contraction so much so that even the much smaller Erbium ion stabilizes in the perovskite structure for $x = 0.7 - 0.9$ in $Er_{1-x}Ba_xCoO_3$.

For an ideal structure, when the atoms are just touching one another, A-O distance is equal to $\sqrt{2} (a/2)$ where as B-O distance is $a/2$, where 'a' is the cubic unit cell length and the following relation between the ionic radii holds:

$$(r_A + r_O) = \sqrt{2} (r_B + r_O)$$

where r_A, r_B and r_O are the ionic radii of A, B and O respectively. It was found that the cubic perovskite structure or slightly distorted modification of it was still retained in ABO_3 compounds even when this relation is not exactly obeyed. As a measure of deviation from ideality, Goldschmidt[53] introduced a 'tolerance factor' t, defined as:

$$t = (r_A + r_O) / \sqrt{2} (r_B + r_O)$$

This is applicable at room temperature to the empirical ionic radii. For an ideal perovskite, 't' is unity. However the perovskite structure is also observed for lower 't' values (0.75 < t <1). In such cases, the structure distorts to tetragonal, rhombohedral or other lower symmetries. Megaw[40] observed that in the range of 0.75 < t < 0.90, an orthorhombic distortion is favoured, while within 0.90 < t < 1.0 range, rhomboheral modification may exist. While dealing with the structural deformation, the tolerance factor limits have been widely quoted in the literature[54-59]. For example Obayashi and Kudo[52] explained the non-formation of perovskite type oxides in the $LnCoO_3$ series after Europium as due to falling of 't' value below 0.7

Many perovskite oxides are observed to be polymorphs. Besides the geometric relations for the stability, the A and B cations must in themselves be stable in twelve fold or (8+4) or (6+6) and six fold coordination respectively. This condition sets the lower limit for the cation radii. In oxide systems[32], these limits are $r_A > 0.90$ A° and $r_B > 0.51$A°. $SrTiO_3$ is the well- known typical example of the ideal cubic structure at room temperature. In this compound the TiO_6 - octahedra are undistorted with 90°angles and six equal Ti-O bonds at 1.952A°. Twelve equidistant oxygen atoms at 2.761 A° surround each Sr ion. It is also interesting to know that many compounds show ideal cubic structure only at high temperatures and generally these high temperature forms can not be quenched[36].

Yakel[60] suggested the difference between the observed and the theoretical tolerance factor as due to partial covalent bonding between the transition metal ions and oxygen ions by considering a small inter atomic distortion and the lattice

distortion. The constantly revised ionic radii also leave much uncertainty in the calculated tolerance factor values. It is observed that the tolerance factor of many perovskite compounds fall outside the admissible limits. Hence Geller[61] thought it was worthwhile to estimate the ionic sizes. By comparing even a single series of $A^{3+}B^{3+}O_3$ oxides, he found that the equilibrium distance of A^{3+}- O^{2-} and B^{3+}- O^{2-} respectively are substantially affected by A^{3+} and B^{3+} ions. Thus he concluded that the region of distortion is much more complex through the relative effective ionic size which plays an important role in distortion. Suziki et. al.[62] has reported structural phase transition of $LaMO_3$ perovskite oxides with different size of B - site ions. They observed the doping effect on the phase transition from orthorhombic to rhombohedral structure in terms of tolerance factor and B - site ion size. The transition temperature with different size B ion linearly decreased with the 't' value indicating that the perovskite with small tolerance factor is distorted resulting in the higher transition temperature.

b) Jahn-Teller, Covalency and Temperature effect

LaMnO$_3$ crystallizes in both orthorhombic and rhombohedral modifications. Mn^{3+} ion itself being a Jahn-Teller ion, a distortion to a low symmetry ordering can be expected at low temperature. But the nature and extent of distortion has been observed to depend very much on the preparative conditions. This behaviour of LaMnO$_3$ has been attributed to the fluctuating Mn^{3+}/Mn^{4+} ratio. Yakel[60] observed a change of crystal symmetry from orthorhombic to rhombohedral phase at 35% of

Mn^{4+} concentration of total Mn ions. Koehler and Wollen[63] noted from neutron diffraction studies that an antiferromagnetic $LaMnO_3$ consists of layers of Mn^{3+} ions coupled ferromagnetically via intervening oxygen ions in a given set of (001) planes but the alternate planes have antiferromagnetic spin orientations. Further, depending upon the Mn^{4+} concentration the manganite shows different type of antiferromagnetic structures. This suggests that factors other than Jahn-Teller ordering may be involved. Whangbo et. al.[64] recently studied the effect of metal-oxygen covalent bonding on the competition between Jahn-Teller distortion and charge disproportion in the high spin d^4 metal ions in $LaMnO_3$ perovskite using electronic factor. Jahn-Teller distortion is favoured over a charge disproportion because the covalent character is weak in Mn-O bond.

With the formulation of new hypothesis of covalent and semi-covalent bonding between the O and Mn ions Goodenough[65] was able to explain the several crystallographic lattices present in the manganites. Mn^{3+} ions with d^4 electronic configuration hybridize with empty s and p orbitals to give dsp^2 square planar orbitals. Mn^{4+} ion with d^3 configuration can have d^2sp^3 hybridization and the six hybridized orbitals point towards six oxygen ions in the octahedral arrangement. These two sets of hybridized orbitals can give rise to three possible Mn-O bonds.

(i)   Covalent or semi-covalent bond, if an empty orbital points towards the O^{2-} ion.

(ii)   An ionic bond, if the empty orbital points away from O^{2-} ion and

(iii) A metallic-type bond, if the O^{2-} ions are between Mn^{3+} and Mn^{4+} ions.

The first bond is stable and has the shortest Mn-O bond length. In $LaMn^{3+}O_3$, the square planar hybridized orbitals allow two third of the Mn-O bonds to be semi-covalent or covalent. These bond types lead to different Mn-Mn separation and results in the increased elastic energy of the crystal. The covalent bonds then order below a certain temperature causing lattice distortion.

Wold and Arnott[43] studied a transformation from orthorhombic to rhombohedral phase, at high temperature. Increase of lattice parameters with temperature will also have the effect of decreasing the ordering and hence the distortion. Because of the parallel effect, the magnitude of distortion and the temperature of transformation were also observed to decrease with increase in concentration of foreign ions.

c) Ordering of B, B' cations

When the same B cation exists in two distinguishable states, ordering among these is possible at low temperatures which will give rise to the additional distortion. $LaCoO_3$ at lower temperature has R3c symmetry[48] and the cobalt ion exists in low spin state. The energy difference between high spin Co^{3+} and low spin $Co^{(III)}$ being only 0.08 eV; their population becomes nearly equal at around 127°C. Relatively small size and hence increased covalent bonding with O atom through empty e_g orbitals make changes in the effective ionic charge at $Co^{(III)}$ ions, which differentiate it from Co^{3+} ions. These two distinguishable B ions affect anion displacement[66]. In anion displacement, the AO_3 (111) planes may remain equidistant from the

neighbouring B cation (111) planes, leaving all the cations equivalent. Within these planes, three A-O distances are reduced and three are enlarged through cooperative rotation of the B-cation octahedra. In $LaCoO_3$ at 127°C, the anion movement occurs within pseudo cubic (110) planes including the B-B axis. This creates two distinguishable B-positions: the B-position with a shorter B-O separation and the B'-position having a larger B'-O separation. This further reduces the symmetry to R3m.

2.3 NONSTOICHIOMETRIC EFFECT

The tendency of showing the different oxidation states of transition metal ions, generally introduces nonstoichiometry in their oxides. In perovskite oxides, nonstoichiometry may be present with respect to A, B and oxide ions[67-69]. It is expected that the A site vacancies will be more common as the A cation mainly fills the dodecahedral void. An extreme example of this type is ReO_3, wherein all the A sites are vacant. The BO_6 octahedra being the building blocks of perovskite structure, the B site vacancies will be quite rare but the ease of stabilization of B cations in different oxidation states can give rise to a good amount of anion nonstoichiometry. Oxygen nonstoichiometry can be of two types: (i) O-rich ($ABO_{3+\delta}$) and (ii) O-deficient ($ABO_{3-\delta}$).

$LaMnO_3$ is a good example of O-rich perovskite with δ as high as 0.15. Lattice parameters variation with charge of O- content in $La_{0.7}Pb_{0.3}MnO_3$ system was reported by Gallagher et. al.[70]. Conversion of Mn^{4+} to Mn^{3+} ions in reducing atmosphere is initially accompanied with O-vacancies leading to an increase in

lattice parameters. More than 5% loss of oxygen is followed by the reduction of some Mn^{3+} to Mn^{2+} ions along with the creation of additional O-vacancies. At around 20% oxygen loss, all the Pb^{2+} ions are reduced, accompanied by the separation of MnO phase and the lattice parameters of the perovskite dropping to that of $LaMnO_3$. Voorhoeve et. al.[71] reported change of crystal structure with O-content. $LaMnO_{3.01}$ is orthorhombic, where as $LaMnO_{3.15}$ is rhombohedral. The manganites of higher lanthanides were prepared by Mc Carthy et. al.[72] in air and were found to be O-deficient with a small but significant variation in their lattice parameters. Gonen et. al.[73] reported the nonstoichiometry in $LaMnO_{3+\delta}$ which is most likely accommodated by creating vacancies both at A and B sites of the perovskite structure. Jorge et. al.[74] prepared perovskite samples by two different methods and found that the formation of perovskite phase was significantly influenced by the synthesis route and processing conditions. Samples prepared by the citrate method have a less distorted structure and are always more oxidized and consequently have a higher Mn-ion content than those prepared by ceramic method.

The nonstoichiometry study has also thrown light on the stability of these oxides. Gallagher et. al.[70] reported that cobaltites were less stable than manganites, while alkali earth substituted manganites were more stable than lead substituted ones. Nakamura et. al.[75] explained the instability of $LaCoO_3$ and $LaNiO_3$ on the basis of the existence stable K_2NiF_4 type stable compounds.

The stability of the $LaMO_3$ compounds was in the order of $LaCrO_3 > LaVO_3 > LaFeO_3 > LaMnO_3 > LaCoO_3 > LaNiO_3$.

2.4 GENERAL PROPERTIES OF PEROVSKITES

The ABO_3 perovskites show several interesting properties such as ferromagnetism, ferroelectric, pyro-and piezoelectric, superconductivity, large thermal conductivity, fluorescence and catalytic activity.

2.4.1 Electrical properties

Perovskites posses interesting electrical properties ranging from insulators to metallic conductors. Many perovskite oxides exhibit high electrical resistivities, which make them useful as dielectric materials. A group of perovskite materials, which contain B-ions in an oxidation state lower than their most stable one or which contain B-ions in two different oxidation states are fairly good conductors or semiconductors. Conductivity data of many perovskites have been related to their magnetic properties which in turn depend upon the crystal structure[25]. Phase transformations or magnetic properties of these materials often influence their conducting properties. Goodenough[66] showed that in $LaNiO_3$, there is metallic conductivity from -200 to 300°C, and the conductivity is through d-electrons of transition metal oxides. The data obtained strongly supports the existence of a partially filled σ^* band. $LaCoO_3$ below ~ 127°C was found to be a semiconductor. Its conductivity increases much more rapidly with temperature in the temperature range of 127 to 927°C.

Vassiliou et. al.[54] studied the resistivity of $NdNiO_3$, which was found to be 1.5×10^{-2} Ωcm. They also studied the temperature dependent resistance of this

compound and found that in the temperature range -143 to 27°C it behaves like a metal. At lower temperature the metallic behaviour changes smoothly to semi-conducting, as visualized by the rapid increase in resistivity with decreasing temperature. Between -143 and -223°C, the conductivity is thermally activated. This is a typical semi-conducting behaviour indicating that $NdNiO_3$ undergoes a metal to semiconductor transition at about -143°C.

Lacore et. al.[55] in their study of conductivity measurements of $RENiO_3$ (RE = La, Pr, Nd, Sm) perovskites found that these compound have a M-I transition and that increasing the rare earth radius leads to higher conductivity via decreasing the temperature of this transition. To correlate the structural and conductivity effects, they conclude that increasing the rare earth radius decreases the distortion between the neighbouring NiO_6 octahedra, which improves the electronic overlap between Ni ions and decreases the temperature of M - I transition. The tilting of NiO_6 octahedra is the main component of the distortion from ideal cubic perovskite structure[56]. These factors are main parameters in the electronic and magnetic behaviour of the $RENiO_3$ systems because they govern the transfer integral between Ni e_g and oxygen 2p orbitals and therefore there is electron transfer and exchange energy among them. The changes at the transition are essentially because of (i) an increase in Ni-O distances and (ii) a sudden increase in the tilt of octahedra. Sreedhar et. al.[76] studied the temperature dependence of the resistivity of $LaNiO_3$ and found a positive coefficient of resistivity, typical of a metal, down to -269°C with the resistivity varying from ~ 1.8 milli ohm.cm at 17°C to ~ 0.5 milli ohm.cm at -269°C. These

resistivity values are nearly two to three orders of magnitude larger than those characterizing ordinary metals.

Blasco et. al.[77] observed M - I transition in $NdNiO_3$ and similar behaviour in the electrical properties without regard to grain size of the compositions guaranteeing the intrinsic behaviour of material and mentioned that the conductivity mechanism cannot be explained either as in a classical semi-conductor or by the motion of electrons in a conduction band in the metallic phase Ni-O-Ni angle.

Sharma et. al.[78] arrived at a conclusion that the insulating property of $NdNiO_3$ against the metallic $LaNiO_3$ is due to the increased hopping interaction strength of $LaNiO_3$ between the oxygen and Ni d-states. $NdNiO_3$ derives its ground state insulating property from the simultaneous presence of electron correlation and strong covalent effect. Goodenough[79] showed that $NdNiO_3$ above a first-transition temperature T_t, it is metallic, whereas below T_t, it is antiferromagnetic insulator. Thornton[80] observed a broad higher order semi-conductor to metallic transition between approximately 247 and 477°C for $LaCoO_3$.

Barman[81] recently reported the resistivity and magnetoresistance measurements of perovskite oxides $LaMnO_{3+\delta}$, $LaCoO_{3+\delta}$ and $LaNiO_{3+\delta}$. The sample $LaMnO_{3+\delta}$ showed a small increase in resistivity in the low temperature range below -243°C and a large resistivity peak and a large negative magnetoresistance in the temperature range of about -23°C. This can be ascribed to the double exchange mechanism, due to the presence of mixed valency of Mn (Mn^{3+}/Mn^{4+}). The $LaCoO_{3+\delta}$ shows a sharp fall in resistivity near -223°C and after that semi-conducting

behaviour, which is due to combined effect of spin state transition of Co ions and the typical thermal activation of the semi-conductors. The $LaNiO_{3+\delta}$ sample shows a metal-semiconducting type of transition near -138°C, which shifts towards higher temperature with the application of magnetic field. Mahesh[27] observed that rare earth manganites of the formula $La_{1-x}A_xMnO_3$ (A = divalent alkaline earth cation) become ferromagnetic and undergoes an insulator-metal transition at around Curie temperature Tc, when the Mn^{4+} content is around 30%. These materials also show giant magnetoresistance, especially at around Tc.

2.4.2 Magnetic properties

Perovskites show interesting variations in their magnetic properties, due to orientation and ordering of spins in the lattices. This kind of ordering in spin results in ferromagnetic, antiferromagnetic and ferrimagnetic materials.

Ferromagnetism arises out of the parallel alignment of magnetic moments of the ions and leads to the higher magnetic moments than ferri and antiferromagnetic materials. Antiferromagnetism is due to the opposite alignment of the magnetic moments and has zero resultant magnetic moment.

For perovskite like compounds, a number of interesting magnetic properties have been reported[2,56,57,74,75,80,82,83], ranging from paramagnetic to antiferromagnetic with the change in temperature. In some of these compounds, the outer d-electrons are localized and are spontaneously magnetic. In some the electrons are itinerant making them spontaneously magnetic and in others Pauli paramagnetism has been

observed. These properties are stabilized depending upon the number of d-electrons per transition metal B-cation and strength of B-O-B interactions. In transition metal of perovskite, d-electrons generally can occupy either localized or itinerant states depending upon the transition metal ions. In the magnetically ordered semiconductor LaFeO$_3$, the Fe $^{(III)}$ ions are in the high spin configuration $t_{2g}3$ e_g2, while the low spin $t_{2g}6$ e_g1 of Ni $^{(III)}$ ions in LaNiO$_3$ give rise to metallic behaviour. LaCoO$_3$ is intermediate between these two extremes as the d-electrons show localized and itinerant behaviour at different temperatures[48, 84, 85].

The interaction energy between two metal ions depend on (i) the distance between these ions and oxide ion through which the interaction occurs and (ii) the angle M^I-O- M^{II} (M = metal ion). The exchange energy decreases rapidly with the increase in the distance and will be greatest for the angle of 180°. In magnetic oxide perovskites, the common exchange mechanism is that of super exchange type i.e. the mutual interactions of the metal ions through the oxygen atom situated between them.

The unsubstituted LnBO$_3$ oxides are interesting because of the different magnetic structures shown for different transition metal ions. Thus in the first row transition metal series, chromites are antiferromagnetic, manganites are either antiferro - or ferromagnetic, orthoferrites are weakly ferromagnetic, cobaltites are paramagnetic and nickelates are Pauli paramagnetic. Neutron diffraction study carried out by Wollen and Koehler[63] can shed light on magnetic structures of these oxides. LaMnO$_3$ has an A type magnetic structure with ferromagnetic coupling

between Mn^{3+} ions in a plane and an antiferromagnetic coupling between Mn^{3+} ions in the adjacent planes. Goodenough[65] has developed a new theory of covalency using hybridized orbitals to explain the magnetic structures of $LaMnO_3$ and $CaMnO_3$, which is also applicable to $LaCrO_3$. Cobaltites do not have any such spontaneous ordering but are queer enough due to the profound effect of the temperature on the spin and oxidation states[48]. The magnetic susceptibility of $LnCoO_3$ (Ln = La, Pr, Nd and Ho) shows three important regions: (i) a low temperature region where $1/\chi_g$ is essentially linear with temperature, (ii) an intermediate temperature region where $1/\chi_g$ is independent of temperature and (iii) a high temperature region where $1/\chi_g$ is again linear but leading to a higher effective moment.

DTA and Mossbauer studies have revealed several processes taking place in these regions. Co-ions are essentially low-spin at low temperature. With the rise in temperature they are thermally excited to a high spin-state, which is only 0.08 eV higher in energy. At around -73°C high-spin to low-spin ratio being more, electron transfer occurs from high-spin Co^{3+} to low spin $Co^{(III)}$ ions, resulting in low spin $Co^{(II)}$ and intermediate spin $Co^{(IV)}$ $t_{2g}4$ e_g1 ions. This is followed by the onset of a short range ordering at around 127°C, accompanied with simultaneous increase in Co^{3+} concentration and cation-anion movements. At about 377°C, complete ordering of Co^{3+} and $Co^{(III)}$ in alternate (111) planes effects a change of crystal symmetry.

The nature of coupling between the Mn-ions in $LaMnO_3$ was revealed from magnetic structure analysis[63]. A ferromagnetic coupling between the planes suggest that Mn^{3+}- Mn^{3+} interaction is distance dependent as was proposed by Watanabe[86].

For the system $LaCo_xNi_{1-x}O_3$, Rao et. al.[87] pointed out that Ni substitution forces the Co-ions to low spin state, so for x = 0.7, the compositions are Pauli paramagnetic.

Goodenough et. al.[88] studied the crystal symmetry and magnetic property correlation in the system $LaMn_{1-x}M_xO_{3+\delta}$ (M = Ga and Co). Mn^{3+}-O- Mn^{3+} super exchange was found to be crystal structure dependent. They found maximum magnetic moment in the range 0.25 < x < 0.4 for cobalt containing system. Substitution with non Jahn-Teller ions (Co^{3+}) or high temperature decreases the orthorhombic distortion and increases the isotropic ferromagnetic coupling. In the system, Co-ions thought to be in diamagnetic low-spin state with Mn-ions only contributing to the magnetic moment value for x < 0.5, composition with x = 0.5 shows a double curie point. Both high and low spin states were assumed to co-exist for higher value of x. Instead, Jonker[89] who also studied the system $LaCo_{1-x}Mn_xO_3$, suggested the formation of Co^{2+} and Mn^{4+} ionic states and a strong positive interaction between them. Recently, Yang[82] arrived at a conclusion that Co ions in the above doped system have nonzero magnetic moments. The values do not lie in the low-spin states as in $LaCoO_3$. The total moments of the doped compositions are decreasing with the concentration of Co dopant varying from 0.25 to 1.0, which is due to the decrease of Mn/Co ratio and the local moments of both Mn and Co ions in the doped compositions. They concluded that $LaMnO_3$ is antiferromagnetic, $LaCoO_3$ is paramagnetic where as intermediate compounds are ferromagnetic in nature.

The electron orbitals of the rhombohedral $LaMnO_{3+\delta}$ are degenerate and any static, co-operative Jahn-Teller deformation is suppressed. As δ increases, the MnO_3

array is oxidized to give a mixed-valent Mn^{3+}/Mn^{4+} system. Trapping of Mn^{4+} ions at the cation vacancies introduces super magnetic clusters, within which fast electron transfer from Mn^{3+} to Mn^{4+} ions introduces a ferromagnetic double exchange that is stronger than the antiferromagnetic Mn^{3+}-$O_{2p\pi}$- Mn^{3+} super exchange interaction.

Very little was known about the magnetic behaviour of $RENiO_3$, before the nineties. Goodenough[66] studied the susceptibility measurements as well as neutron diffraction on $LaNiO_3$ for the first time and did not find evidence for magnetic ordering at above -263°C. The value and the temperature dependence of the magnetic susceptibility were consistent with a Pauli paramagnetic behaviour. These results were agreeable to Demazeau[50] and concluded that only those compounds with diamagnetic RE^{3+} ions show magnetic susceptibility measurements. Since 1989, several authors[54,90,91] reported magnetic susceptibility measurements on $PrNiO_3$ and $NdNiO_3$, but could not derive any information about the behaviour of the Ni magnetic moments, since the contribution of Pr^{3+} and Nd^{3+} ions are enormous. The Curie-Weiss behaviour[66] was observed for $YNiO_3$ and $LuNiO_3$. A sudden increase in magnetic susceptibility at -128°C for Y and -143°C for Lu was interpreted as the onset of co-operative ordering of the Ni magnetic moments. From the refined values of the Curie constant they concluded that Ni ions were trivalent with the low-spin $t_{2g}6 \; e_g1$ configuration. Garcia et. al.[92] studied the magnetic structure of $PrNiO_3$ and $NdNiO_3$. The existence of an equal number of ferromagnetic (F) and antiferromagnetic (AF) coupling between nearest neighbours is the most interesting feature of such a magnetic arrangement. Thus, each Ni magnetic moment is coupled

with three of its six nearest neighbours via AF interactions, whereas the coupling with the three others is F.

In the orthorhombic structure, the e_g orbitals are split up into two non-degenerate a_{g1} and a_{g2} orbitals. If only one of the a_g orbitals were occupied, then Goodenough-Kanamori rule[83] would have predicted the existence of AF coupling between the Ni magnetic moments. The experimentally observed arrangement contradicts to the uniform occupation of a_g orbitals. Actually observed magnetic structure results from the occurrence of an orbital super - lattice. As the difference in energy of the a_{g1} and a_{g2} orbitals may be very small, the competition between inter-atomic exchange correlation and the energy gain by the electrons occupying the lower energy orbital can lead to a ground state in which the lattice breaks up into two sub-lattices, each with predominantly one of the a_{g1} or a_{g2} orbitals half occupied. The nearest neighbouring Ni atoms with the electrons in the same orbital will be the AF coupled and those with a different orbital occupancies will prefer to align their $S = 1/2$ spins parallel.

The co-operative Jahn-Teller effect[93] is another mechanism, which may induce orbital ordering. In $LaMnO_3$ compound, the electronic configuration of Mn^{3+} is $t_{2g}3\ e_g1$. To break the degeneracy of the e_{g1} orbitals a strong elongation of the MnO_6 octahedra takes place, resulting in the orbital ordering. The orientation of the e_g orbitals can be directly deduced from the alternating arrangement of the elongated MnO_6 octahedra. In $RENiO_3$ perovskites, no appreciable Jahn-Teller distortion has been observed, the existence of an orbital super-lattice being invoked uniquely to

explain the existence of such an unusual magnetic structure. Rosenkranz[94] studied the co-operative magnetic ordering in the Nd sub-lattice. The sharp rise of some magnetic reflections observed below -243°C indicates the existence of induced magnetic ordering of the Nd^{3+} moments in $NdNiO_3$.

Thus, in the case of transition metal rare earth perovskites, the B-B interaction and A-B interaction predominate depending upon the size and electronic configuration of the A-site and B-site ions. The compounds will show antiferromagnetic, ferrimagnetic or paramagnetic behaviour depending on the relative strength of these interactions.

2.4.3 Vibrational Spectroscopy

Infrared spectroscopy is a powerful and widely used tool for the characterization of perovskite materials. There exists a close relation between spectra and structure. Therefore, the analysis of vibrational spectra is a rapid and sensitive method for obtaining structural information. In the recent years a large number of spectroscopic studies on perovskite related materials have been reported[95-101]. For the ideal cubic perovskite, the optically active internal vibrations can be classified as T_{vib} = $3F_{1u}+F_{2u}$. F_{1u} modes are IR-active whereas F_{2u} is inactive. These four vibrations, in a crude approximation can be described as follows: γ_1 (F_{1u}) is the B-O stretching vibration of the BO_6 - octahedra, γ_2 (F_{1u}) is essentially an O-B-O angle deformation coupled to some extent with A-O motions, γ_3 (F_{1u}) represents the motion of the full A-lattice against the BO_6 - octahedra and the inactive mode γ_4 (F_{2u}) is also an O-B-O

angle deformation. The expected band order is usually $\gamma_1 > \gamma_3 > \gamma_4 > \gamma_2$. As γ_2 is usually expected to lie at very low frequencies and γ_4 is inactive, cubic perovskites show rather a simple, two band infrared spectrum[101-105].

In the case of lower symmetry or distorted materials, one may expect some splitting of the F_{1u} modes and the eventual activation of γ_4[96,106]. Perovskite oxides were investigated in a classical paper by Last[105] and later by many other workers[100,107] and the literature cited there in. The previous analysis of the vibrational modes of a cubic perovskites suggests some mixing between BO_6 and AO_{12} motions. This is especially true for $A^{III}B^{III}O_3$ materials. In case of $A^{I}B^{V}O_3$ phases and also in more complex stoichiometries, this mixing is probably lowered. In these compositions a highly charged cation is located at the B- sites.

Another point of interest is that IR-studies can be used to differentiate perovskite forms from other polymorphic forms[108]. Recently, a number of oxidic materials structurally related to K_2NiF_4 have also been investigated by means of IR-spectra techniques[109-111].

2.5 HETEROGENEOUS CATALYTIC PROCESS

The steps involved in every heterogeneous catalytic process are:

1. Diffusion of the reactants from the bulk to the surface of the catalyst.

2. Adsorption of the reactants on the catalyst surface.

3. Chemical reaction of the adsorbed species on the catalyst surface.

4. Desorption of the products from the surface and

5. Diffusion of the products into the bulk.

Depending upon the slowest step, the catalytic process can be classified as either diffusion controlled or kinetically controlled. An understanding of the kinetically controlled catalytic process requires the study of nature of adsorption as well as the reaction mechanism.

2.5.1 Studies of carbon monoxide oxidation by oxygen

Catalytic CO oxidation occurring on the surface of metal oxides has been classified by Voorhoeve et. al.[13] as intrafacial and suprafacial processes. In suprafacial process catalyst surface provides a set of electronic orbitals of proper energy and symmetry for the bonding of reactants and intermediates. In this process relatively less active catalyst surface is involved. The transition metal ions at the surface provide proper atomic orbitals for the adsorption of the reactant molecules. In the suprafacial process, the reaction rate appears to be correlated primarily with the electronic configuration of the surface transition metal ions or of surface defects. In intrafacial process, the catalyst participates as a reagent that is partly consumed and regenerated in a continuous cycle. The reaction rate of this process appears to be correlated primarily with the thermodynamic stability of oxygen vacancies adjacent to transition metal ions.

In general CO oxidation can proceed in two ways depending upon the nature of the surface oxygen that is involved in the reaction:

a) Reaction with oxygen in the adsorbed state

This can occur either through Langmuir-Hinshelwood or Eley-Rideal type of interaction depending upon whether CO reacts from an adsorbed state or from gas phase with adsorbed oxygen. The interaction between chemisorbed reactants is referred as Langmuir-Hinshelwood mechanism and other as Eley-Rideal mechanism. The reaction between adsorbed CO and gas phase O_2 is known to be Eley-Rideal is not very common.

b) Reaction involving lattice oxygen

In this mechanism, the adsorbed CO reacts readily with lattice oxygen to form CO_2 and lattice oxygen is then replenished by gas phase oxygen.

2.5.2 Metal and metal oxide surfaces

A review article by Savchenko[112] presents the current status of oxidation of CO on metals. Rajadurai and Carberry[113] have demonstrated the structure sensitivity of Pt-catalysts for CO oxidation. Jin et. al.[114] highlighted the role of lattice oxygen in the case of Pt/CeO$_2$ catalysts for the CO oxidation. Sung-Ho et. al.[115] have reported the effect of magnesium on preferential CO oxidation on platinum catalyst. Kim et. al.[116] studied the oxidation of CO on CdO / La$_2$O$_3$ system and reported that CO essentially chemisorbs on the lattice oxygen of Cd-doped La$_2$O$_3$, while O$_2$ on the lattice oxygen vacancies induced by Cd doping. Meng et. al.[117] investigated the catalytic CO oxidation activity over manganese oxide supported on CeO$_2$. Gagarin et. al.[118] made an attempt to project the role of electronic factor of the catalysts on

the catalytic oxidation of CO. Indoniva et. al.[119] studied the CO oxidation on CoO/MgO and found that the d-electron configuration of Co^{2+} is of primary importance and the nature of matrix and the extent of dispersion are less relevant.

Kobayashi et. al.[120] by using transient response method suggested a mechanism involving interaction of gaseous CO with surface anions or neutral oxygen for the formation of CO_2 on ZnO surface. Jen and Anderson[121] concluded that CO reacts readily with oxygen at the surface to form CO_2, which can immediately bind to O^{2-} to form surface carbonate. Reaction with isolated O^- has a higher barrier on account of O-CO bond formation with promotion of electron to surface conduction band. In this case CO_2 gets dissociated from the surface thus stabilizing the promoted electron.

A large variation in the surface properties of a commercial copper oxide/γ-alumina catalyst induced by calcinations in temperature range 450-1050°C both in oxidizing and reducing atmosphere, was reported by Huang and Yu[122]. Decrease in CO oxidation beyond 900°C was attributed to calcination temperatures in the region of 1000°C which may be detrimental to the catalyst. Kapteijn[123] succeeded in finding out substitute for noble metal catalysts for purification of auto-exhaust. Supported Cu / Cr oxide catalysts were found to be most active for CO oxidation and NO reduction by CO.

In the study of CO oxidation at lower temperature over composite noble metal/reducible oxide catalyst, Hertz et. al.[124] summarized that the high activity for CO oxidation can be obtained over a composite material of highly interspersed

mixture of one type of site, α, that adsorbs CO and O_2 and another type of site, β, that adsorbs oxygen without significant CO inhibition. Szanyi and Goodman[125] summarized that the presence of certain level of surface oxygen is advantageous during CO oxidation on a Cu (100) catalyst, however, under stoichiometric conditions an oxide layer formed significantly reduces the catalytic activity compared to metallic copper.

Jernigan and Somorjai[126] concluded that the mechanism for CO oxidation over the three copper catalysts (copper-O, copper-I oxide and copper-II oxide) was affected by sub-surface oxygen and oxide formation. The stability of a given oxidation state of copper under reaction conditions was found to be a function of oxidizing power of the CO/O_2 partial pressure ratio. The rate of reaction at 300°C decreased with increasing copper oxidation state ($Cu > Cu_2O > CuO$) and the activation energy increased with increasing copper oxidation state (Cu -9 $< Cu_2O$ -14 $< CuO$ -17 Kcal/mol). According to Boccuzi et. al.[127], Au/ZnO catalyst prepared by Co-precipitation method, exposes gold sites, which are able to adsorb both oxygen and CO atoms at the same time and easily oxidize CO to CO_2.

Mergler[128] synthesized successfully the catalyst $Pt/CoO_x/SiO_2$ that could bring about CO conversion at room temperature. He suggested that during CO oxidation by oxygen, O^- vacancies on Co_x play an important role as dissociation centers for oxygen. According to the mechanism proposed by Holfund[129] for low temperature CO oxidation on Pt/SnO_x surface, during the reaction, CO gets adsorbed on Pt and associates with a neighbouring hydroxyl group (on a Pt or Sn atom) and

with a neighbouring O⁻ ion on Sn to form a surface carbonate. Further, CO can also

be adsorbed on Pt by neighbouring OH⁻ and form a formate species. Gurav and

Salker[130-131] studied CO oxidation on different spinel systems and proposed that the

CO oxidation by O_2 reaction proceeds by Langmuir-Hinshelwood mechanism.

2.5.3 Molecular orbital approach for carbonyl formation

In simple or mixed transition metal oxides, the nature of CO-catalyst bond is

considered to be essentially important in understanding the metal carbonyl formation

in the mechanistic studies of CO oxidation.

Studies have shown that CO molecule is bonded in carbonyl either linearly

with one transition metal atom or forming a bridge between two or less frequently

between three metal atoms as shown by the following scheme:

```
      O               O                    O

    | | |           | |                    |

      C               C                    C
      |              / \                  /|\

      M             M   M                M M M
```
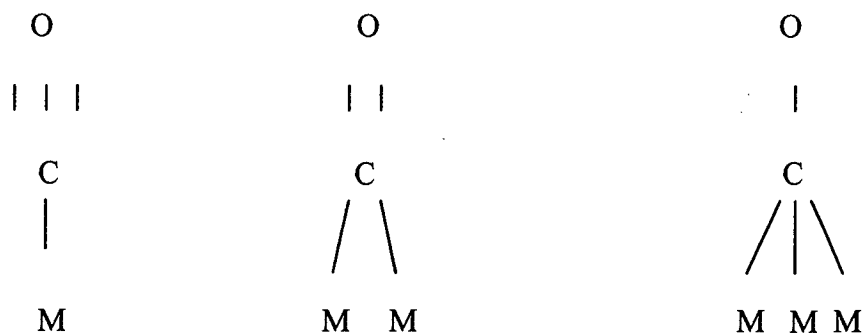
Blyholder[132] demonstrated that the frequency based criterion is incapable of

furnishing a sound basis for calling the structure either linear or bridge. He gave a

qualitative description of the chemical bonding in the adsorbed CO from the stand

point of the theory of molecular orbitals. His calculations together with later findings

37

of the other author[133] explain some particular features of the IR spectra of adsorbed CO. The diagrammatic representation of molecular orbitals of CO and of adsorptive complex of CO with a transition metal is being reproduced[134] in fig. 2.3 along with the scheme of the overlapping molecular orbitals.

When the CO molecule forms a complex with a metallic ion, the antibonding 5σ orbital produced by the $2p_z$ orbitals of carbon overlaps with the unoccupied d_z^2 orbital of metal, producing a donor-acceptor bond between CO and metal and giving rise to a $5\Sigma^+$ orbital. The back donation of the electron from the occupied d-orbital of the metal (d_{yz}, d_{xz}) to the unoccupied 2π orbital of CO produces a dative bond.

In this scheme of molecular orbitals, the formation of donor acceptor bond $M \leftarrow C$ results in an increase in the frequency of the CO- vibration forming a strong bond with the surface. On the other hand, the creation of the dative bond $M \rightarrow C$ lowers the frequency of CO-vibration and forms a weak bond with the surface. Thus according to Little[135] the shift of electron density to the 2π antibonding orbitals weakens the C-O bond in CO molecule decreasing its stretching frequency from 2143 cm^{-1} in free CO molecule to 2100 - 2000 cm^{-1} for neutral unsubstituted linearly bonded one.
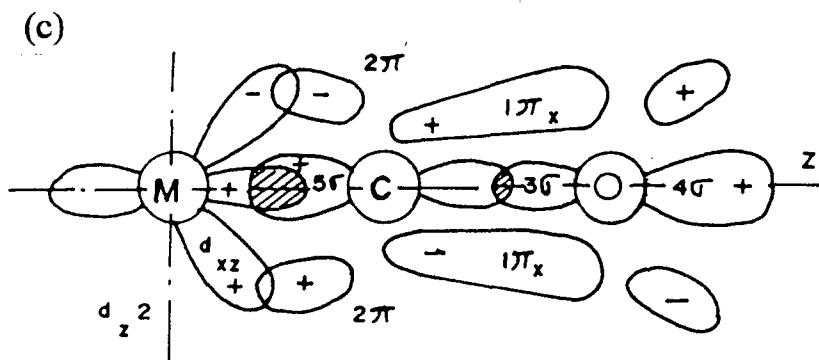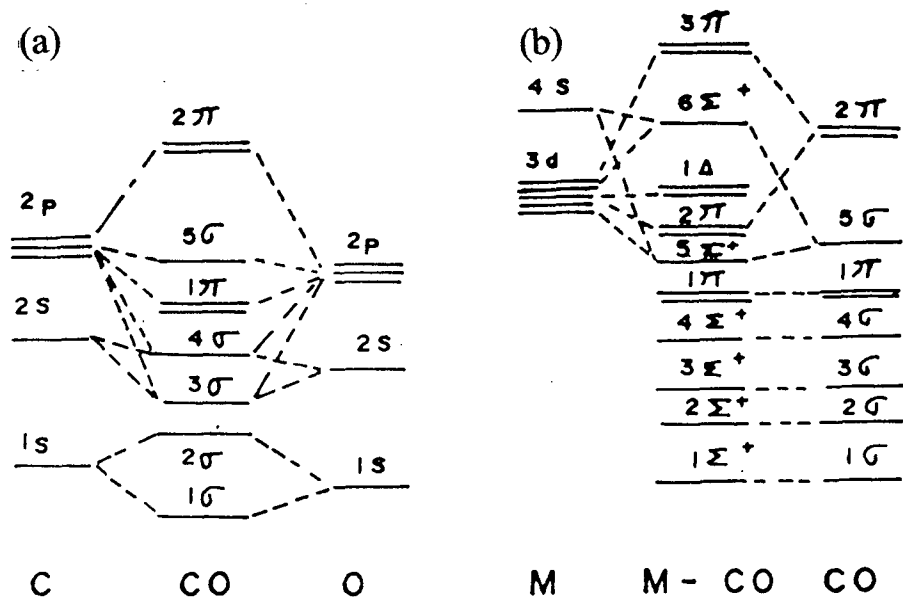
Fig.2.3 (a) Molecular orbital of carbon monoxide (b) Molecular orbital of carbonyl complex (c) Scheme of overlapping of molecular orbital of carbonyl complex

The decrease in bond strength and bond order of CO also results in the decreased stretching frequency of CO molecule, which is in the range 1750-1850 cm^{-1} for doubly co-ordinated CO molecules.

The strength of the donor acceptor bonding M-CO in the first transition series increases steadily from Ca to Ni and decreases with copper. The strength of back donation bond increases from Ca to Ti, further goes down to Ni, and up a little with Cu. The low frequency bands may be explained by multi site adsorption of CO. In general the scheme discussed above is confirmed by numerous experiments with the adsorption of CO on the transition metal oxides[136-139]. A kinetic study by Kobayashi et. al.[120] of CO oxidation to CO_2 over a partially reduced ZnO showed that there are two reaction paths (I and II). For path - I, the proposed model is the surface reaction of gaseous CO with O⁻, followed by rapid adsorption of CO_2 formed. Path - II, is controlled by both the surface reaction of gaseous CO with neutral atomic oxygen species and the desorption of CO_2 formed which is summarized as follows:

Path-I

$$CO + O^-_{(ads)} \xrightarrow{\quad} CO_{2\,(ads)} + e^- \xrightarrow{\quad fast \quad} CO_{2\,(g)} + e^-.$$

Path-II

$$CO + O_{(ads)} \xrightarrow{\quad slow \quad} CO_{2\,(ads)} \xrightarrow{\quad} CO_{2\,(g)}.$$
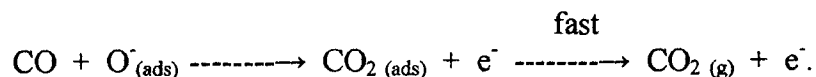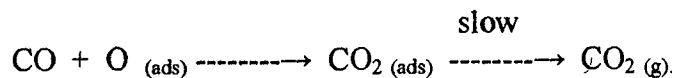
2.5.4 Mechanism of the oxidation of carbon monoxide

The ease of oxidation of CO in presence of catalyst of different type materials like noble metals, oxides etc. leads to an extensive study of the mechanism of CO oxidation. The rate of reaction has been found to vary with catalyst material, temperature, partial pressure of the reactants etc. The reaction is observed to be suprafacial on noble metals and some oxides, whereas on some other oxides it was found to be intrafacial.

Intrafacial process

Roginskii[140], one of the earlier workers to study CO oxidation proposed a mechanism in which he suggested the oxide catalyst as providing oxygen for the reaction followed by a subsequent regeneration of the surface using gas phase oxygen. Around the same period, Garner[141] suggested from experimental thermo chemical data the formation of surface carbonate ions through the lattice oxygen participation. He observed that there was little oxygen adsorption on a bare Mn_2O_3 or Mn_2O_3-Cr_2O_3 surface, but was considerable (half of the adsorbed CO) on a CO preadsorbed surface. Further it was noticed that, the heat of adsorption of CO_2 on Mn_2O_3 is almost equal to the heat of decomposition of manganese carbonate and this suggests that the common adsorbed species must be a carbonate ion. The process was outlined as below:

$$M^{2+} \quad O^{2-} \quad M^{2+} \qquad M^{2+} \quad CO_3^{2-} \quad M^{2+} \qquad M^{2+} \quad CO_3^{2-} \quad M^{2+}$$

$$\xrightarrow{\quad CO \quad} \qquad\qquad \xrightarrow{\quad \frac{1}{2}\,O_2 \quad}$$

$$O^{2-} \quad M^{2+} \quad O^{2-} \qquad O^{2-} \quad M^{2+} \quad 2e^- \qquad O^{2-} \quad M^{2+} \quad O^{2-}$$
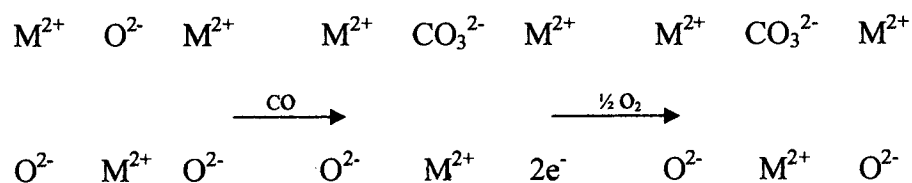
CO interacts with the surface oxide ions forming a carbonate and an anion vacancy, which is subsequently filled up by the gas phase oxygen. This explains the increased adsorption of oxygen on a CO pre-adsorbed surface. Simple experimental evidence was given by the X-ray diffraction analysis of CuO on alumina catalyst. Pierron et. al.[142] observed the reduced Cu_2O and Cu phases when catalyst was activated with CO and hence suggested an alternate redox process on the CuO above160°C.

Winter[143] has provided the conclusive evidence of carbonate formation from the isotopic exchange studies using ^{18}O on Cu_2O and V_2O_5. He observed that both CO and CO_2 readily exchange oxygen with the whole of the out-gassed oxide surface. Hirota et. al.[144] found that the concentration of ^{18}O in CO_2 depends on the amount of ^{18}O on the V_2O_5 surface in the temperature range 347 to 412°C. From these considerations, Hughes and Hill[145] gave the mechanism of CO oxidation with lattice oxygen as below:

$$M = O \;+\; CO \;\dashrightarrow\; (M = O)\; CO$$

$$(M = O)\, CO \;\dashrightarrow\; M: \;+\; CO_2$$

$$M: \;+\; \tfrac{1}{2}\,O_2 \;\dashrightarrow\; M = O$$
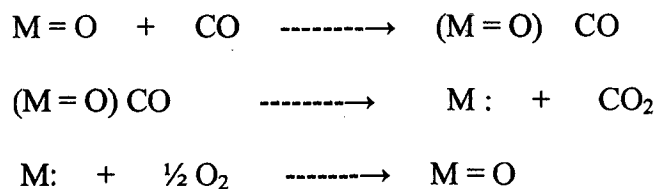
From energy considerations, this type of reaction will necessarily be a high temperature process (300 - 600°C). Marshneva et. al.[146] studied the CO oxidation on V_2O_5 in the temperature region 300 - 500°C and pressure range 1-400 torr. He found that the lattice oxygen participation gains importance at above 450°C so that at above 590°C the reaction proceeds through only lattice oxygen participation. Below 450°C the reaction between the adsorbed species gains importance thus gradually reducing the lattice oxygen participation. Similar observations have been made for TiO_2 and NiO catalysts.

Suprafacial process

The intrafacial process expects the oxidation to occur at high temperature. But the reaction has also been observed at low temperature of -20°C on hopcalite catalyst containing a mixture of oxides of Mn and Cu. This made Stone[147] to suggest that a mechanism other than the surface carbonate species must be involved. The lattice oxygen participation is not an essential requirement, is further proved[123] by the negative ^{18}O isotopic exchange studies on NiO.

The CO_2 adsorption takes place only on an oxygen-preadsorbed surface and the amount of adsorption was the largest for a mixture of $O_2:2CO_2$. Stone and his coworkers[147] measured the heat of adsorption of CO, O_2 and CO_2 on the bare as well as on preadsorbed surfaces of Cu_2O, NiO and CoO. They found that the heat of adsorption of CO and O_2 on the oxygen and the CO preadsorbed surfaces respectively matches well with that of a theoretical surface CO_3 complex species.

Further, computations from heat measurement data by different methods resulted in almost similar heat of formation of surface CO_3 complex, from the gaseous CO and oxygen.

$$CO_{(g)} \quad + \quad O_{2(g)} \ \text{--------}\rightarrow \quad CO_{3\,(ads)}$$
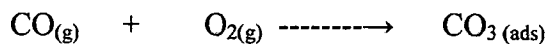
Unlike the CO adsorption the surface shows saturation after CO_2 adsorption and hence it can be inferred that CO interacts with the surface adsorbed oxygen to form CO_3 complex as shown below:

$$O \quad O \quad O \quad\ CO_3 \qquad\qquad O \qquad CO_3 \quad O \quad O$$

$$\xrightarrow{\ \ CO\ \ } \qquad\qquad \xrightarrow{\ \ \frac{1}{2}O_2\ \ }$$

$$M \quad M \quad M \quad\ M \quad M \qquad M \qquad M \qquad M \quad M$$
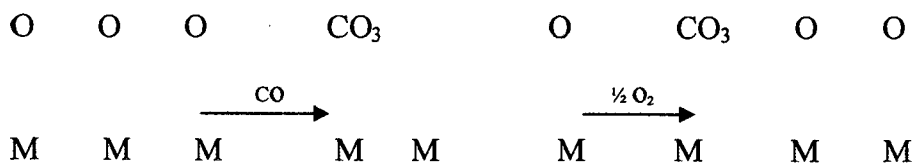
The observations of the Comprehensive study of Cu_2O undertaken by Garner et. al.[148,149] led to the conclusion that a CO_3 complex has been forming at the oxygenated surface according to the below scheme:

$$O \quad O \quad O \quad O \qquad co \qquad O \quad CO_3 \qquad\ O$$
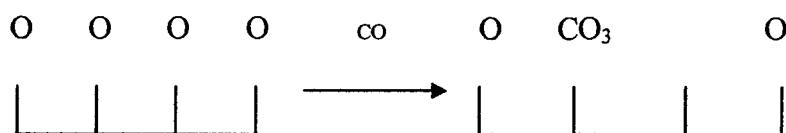
Similar observations were also made on Nickle[150] and cobalt oxide[151]. The study of IR-spectra of the adsorbed CO on Ni carried out by Blyholder[152] provided supplementary evidence for the complex formation.

2.5.5 Formation of carbon dioxide

The final formation of CO_2 from CO_3 complex was revealed from the heat measurements during the incremental CO adsorption on CoO by Rudham and stone[151]. On admission of CO on oxygen pre-adsorbed CoO, the heat of adsorption showed a gradual fall initially without any CO_2 formation. After the introduction of few more pulses, the heat of adsorption dropped by 20 Kcal/mole with a concomitant formation of CO_2, whose concentration was more than that of added CO. This shows the interaction of admitted CO with the CO_3 complex.

Thus on admitting CO, it first gets adsorbed $CO_{(ads)}$, which then at small concentration reacts with the adsorbed oxygen to form CO_3 complex. The further admission of CO reacts with the adsorbed complex to yield CO_2. Overall process can be written as:

(a)　O_2 　　　　　$\rightarrow$ 　$2O_{(ads)}$ 　　　　+ 55 Kcal

(b)　$CO_{(g)}$ 　　　　$\rightarrow$ 　$CO_{(ads)}$ 　　　+ 20 Kcal

(c)　$CO_{(ads)} + 2O_{(ads)}$ 　$\rightarrow$ 　$CO_{3\,(ads)}$ 　　　+ 40 Kcal

(d)　$CO_{(ads)} + CO_{3\,(ads)}$ 　$\rightarrow$ 　$2CO_{2(g)}$ 　　　+ 19 Kcal
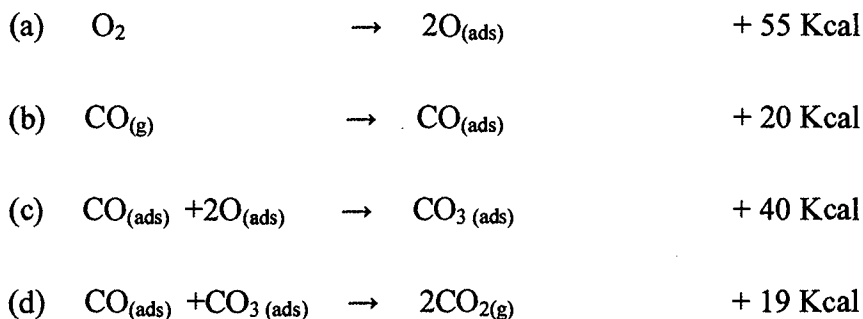
The similarity between the fall of heat of adsorption of CO (20 Kcal/mole) and the difference in the heat of adsorption (21 Kcal/mole) when reaction (d) takes over from (c), justifies the mechanism. This kind of reaction between the adsorbed

species commonly referred to as Langmuir-Hinshelwood mechanism has been observed on Cu_2O and CoO.

An alternative Eley-Rideal mechanism also seems to be possible. The heat of formation of the CO_3 complex from the gaseous oxygen and adsorbed CO is larger (131 Kcal/mole) for NiO, as compared to CoO and Cu2O (111 and 104 Kcal/mole respectively). This necessitates the reaction (d) to be an endothermic on NiO unlike the exothermic one on Cu_2O and CoO and hence less favourable. So the observed small activity was presumed to be due to the reaction between the CO_3 complex and gaseous CO. Hertal and Ferrauto[153] studied the mechanism of CO oxidation on copper chromite and identified two distinct active sites. A carbonyl has been found to be active at temperature in the vicinity of 60 - 80°C, while a less active carbonate species react with O_2 to produce CO_2 at approximately 180 - 200°C. According to Morgan and Ferrauto[154], active site concentration is determined from the actual catalytic reaction allowing one to differentiate active site from the adsorption sites.

2.6 PEROVSKITES IN OXIDATION REACTIONS

The first investigators to suggest the potential application of perovskites as oxidation catalysts were Libby[155] and Pedersen and Libby[156]. The particular behaviour of these materials was explained in terms of the relative ease with which oxygen species can be released from the catalyst surface. The oxidation of low weight hydrocarbons such as methane[157, 158], propane[159-161], propene[15, 162] and n-butane[158] has been frequently taken as a test reaction for perovskite oxides.

2.7 CARBON MONOXIDE OXIDATION ON PEROVSKITES

Carbon monoxide oxidation over perovskite type oxides has been widely studied. Voorhoeve et. al.[163] put forward new ideas in explaining the role of defect chemistry of perovskites such as manganites, cobaltites, chromites and ruthenates. They suggested that two different oxidation processes should be distinguished (a) the catalyst participating in the reaction as a reagent being partially consumed and regenerated in a continuous cycle and (b) the catalyst acting as the template to provide the atomic orbitals of the proper symmetry and energy to activate the reactant molecules. These two alternatives were termed as intrafacial and suprafacial catalysis respectively. The oxidation of CO in the middle temperature range (100-400°C) has been suggested[15] as suprafacial catalytic process wherein it is expected to observe important effects of the ferroelectric and magnetic order of surface spins and of semi-conductivity on the catalytic reaction. $LnMO_3$ perovskites in which the lanthanide (Ln) ions are essentially inactive in catalysis and the active transition metal (M) ions are placed relatively at large distances from each other are excellent catalytic models for the study of the interaction of CO and O_2 on single surface sites. However, it must be stressed that idealized correlations between catalytic activity that is confined to the surface and a single collective parameter (conductivity, ferromagnetism etc.) should not be taken as conclusive.

Oxidation of CO on strontium substituted manganites was first reported by Parravano[164]. The work with these catalysts really took off after Meadowcraft[165]

reported that $La_{0.8}Sr_{0.2}CoO_3$ could match Pt as oxygen electrode. This made Libby[155] to try these oxides as potential auto-exhaust catalysts. Since then elaborate tests were carried out by Voorhoeve[166] with transition metal oxides on automobile emission.

Tascon et. al.[15] have summarized the CO oxidation on $LaMO_3$ surface. Rao and Chakrabarty[167] studied the CO oxidation on $La_{1-x}M_xCoO_3$ catalysts and found that the catalytic activity increases with oxygen deficiency in cobaltites. The catalytic CO oxidation on $LnCoO_3$ was reported by Vishwanathan and George[168] and they correlated the activity with the magnetic moment and the oxygen non-stoichiometry. Gallagher et. al.[169] reported the high activity of copper substituted lanthanum manganites and strong SO_2 poisoning for CO oxidation. The investigation of CO oxidation on $LnCoO_3$ surface and relating the activity of the catalysts to the spin and valence bond of cobalt was attempted by Om Prakash et. al.[170]. Gunasekaran et. al.[171] studied several cuprates and nickelates and reported that the oxidation takes place through the interaction between the adsorbed species. Chakrabarty and Rao[172] studied the CO oxidation over cobaltites of lanthanides and investigated the effect of A-site substitution in $Nd_{1-x}Ba_xCoO_3$ and $LnCoO_3$ (Ln = La, Sm, Nd and Dy). They found that the compounds with cubic structure show maximum activity which decreases with distortion in cubic structure. Shetkar and Salker[173] studied the effect of A-site substitution in $AMnO_3$ (A = Sr, Sm and Nd) manganites and observed that the activity decreases with the distortion in orthorhombic structure. The kinetics of redox reactions between NO and CO over $LaMnO_3$ and $LaCoO_3$ catalysts was studied by Salker et. al.[174]. They were of the

opinion that the rate-controlling step in the catalytic reduction of NO by CO is presumably the active site reduction process. Salker and Vaz[175] studied CO oxidation on $LaMn_{1-x}Co_xO_3$ catalysts and observed that the activity increases with the substitution of Co^{3+} at B-site. Chan et. al.[176] studied the influence of either A or B-site substitution in mixed oxides on catalytic CO oxidation. From the different systems that were investigated, cobaltites were found to be more active than the manganites. They concluded that partial substitution of lanthanum manganites or cobaltites with strontium or copper leads to an increased activity for CO oxidation, which was attributed to an increase in oxygen mobility within the lattice of perovskites. This explains the lattice oxygen participation in the reaction even under stoichiometric conditions. Jaenicke et. al.[177] examined the catalytic activity for CO oxidation over $LaMnO_3$ and $La_{0.5}Sr_{0.5}MnO_3$ catalysts. They confirmed the ability of the catalysts to provide lattice oxygen and to sustain the oxidation reaction, even in the absence of molecular oxygen.

CHAPTER 3

EXPERIMENTAL TECHNIQUES

EXPERIMENTAL TECHNIQUES

Perovskites have been reported to possess interesting structural, solid state and catalytic properties. Ceramic method is commonly used for the preparation of mixed metal oxides whose textural characteristics are not important for their use. The technique involves the heating of an intimate mixture of the respective binary oxides or their precursors (hydroxides, nitrates, carbonates etc.) in solid state at high temperature[81,178-180]. Sol-gel method for the preparation of perovskites is based upon the formation of a sol of the precursors which is destabilized to the formation of a gel[26,28,102,181-183]. In combustion method, the high temperature required for the formation of the oxides is achieved by the exothermicity of the redox reactions between the decomposition products of metal nitrate (oxidizer) and the fuel during combustion[184]. Perovskites can also be prepared by other methods like dry evaporation, explosion, spray-drying, freeze-drying, crystallization, complexation and co-precipitation[15].

In wet co-precipitation method, the constituent metal ions are jointly precipitated as a single or two separate precursors like citrates, oxalates, carbonates, cyanides and hydroxides[28,174,185-187]. The derived precursors are normally stable in air

and ensure better homogeneity. The subsequent decomposition and heating yield fine and higher surface area particles[188-189]. This old non-conventional technique is extensively used as a powerful method. Bell et. al.[28] have reported compounds prepared by this method which are found to be most efficient to facilitate oxidation type of reactions.

In the present context, co-precipitation technique has been fully exploited for the preparation of some perovskites and mixed metal oxides for their solid state and catalytic studies. Some other perovskites for similar studies have been prepared by combustion technique.

3.1 MATERIAL PREPARATION

Perovskites of the compositions:

- (I)$Zn_{1-x}Ni_xMnO_3$ (where, x = 0.0, 0.2, 0.4, 0.6, 0.8 and 1.0)

  Supported metal oxides of the compositions:

- (III) Fe_2O_3/ZnO (where, Fe_2O_3 = 0%, 5%, 10%, 20% and 100%)

- (IV) NiO/ZnO (where, NiO = 0%, 5%, 10%, 20% and 100%)

  were prepared by wet co-precipitation technique[51,131,175,189].

Perovskites of the compositions:

- (II) $AMnO_3$ (where, A = Sr, Sm and Nd), $BaCeO_3$ and $ZnSnO_3$

  were prepared by combustion technique[184].

The step wise process involved in co-precipitation technique is shown in flow diagram (fig.3.1). Stoichiometric quantities of the respective metal nitrates and

361

51

acetates of A.R. grade quality as required in the desired final compositions were weighed and dissolved in about 200 ml of distilled water. The solution was heated at 60-80°C with stirring to get a clear homogeneous solution. 5% sodium hydroxide solution was prepared by dissolving NaOH (A.R. grade) in distilled water to obtain an approximately equimolar concentration solution. This was filled in a burette and was added slowly to the metal ions solution in a beaker on a magnetic stirrer with constant stirring, till the precipitation was complete. The pH of the solution was maintained between 9-10. The precipitate was digested on a hot water bath for about 3 h and then cooled. This was oxidized by drop wise addition of 30% hydrogen peroxide in a burette with continuous stirring of the precipitated mixture on a magnetic stirrer. The precipitate was then washed and filtered using warm distilled water till it was free from nitrate and sodium ions. This was followed by the drying of the precipitate in an oven at 80°C for 10-15 h. The dried precipitate was ground well in a mortar and then heated in a muffle furnace at 700-800°C for 10-12 h to form the required oxides. If X-ray diffraction of the desired perovskites showed any biphasic character, further heating was done for few more hour to obtain monophasic compound. The characterized compositions were finally designated as perovskite and supported metal oxide catalysts.

The step wise process involved in combustion technique is shown in flow diagram (fig.3.2). Stoichiometric quantities of pure (A.R. grade) Sr/Sm/Nd/Ce/Sn nitrate and Mn/Ba/Zn acetate were separately dissolved in distilled water.

Metal nitrates / Acetates
Aqueous solution (A.R.grade)

NaOH solution
(A.R.grade)

Stoichiometric
equimolar
concentration

Co-precipitation

Oxidation by
H_2O_2 (30 %)

Ageing
(Digestion)

Filter & washing

Drying

Grinding

Thermal analysis

Mixture of hydroxides

Calcination

$Zn_{1-x}Ni_xMnO_3$,
Fe_2O_3/ZnO, NiO/ZnO

Characterization and physical
Studies. XRD, IR, AAS, BET,
SEM, Elect. Cond., Mag.
Suscp., ESR, DRS, GC etc.

Fig. 3.1 Flow diagram of co-precipitation preparative method
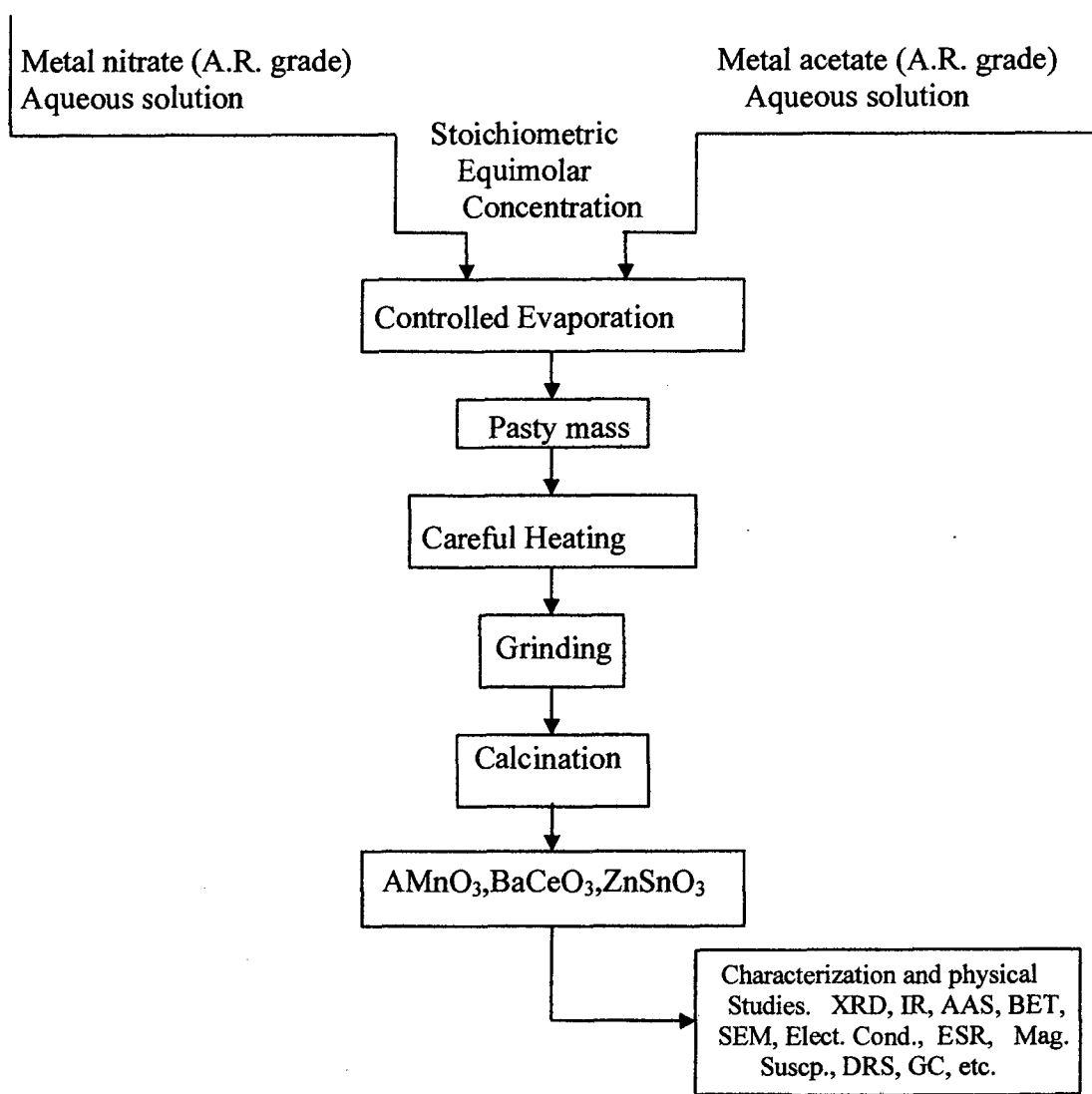
Fig. 3.2 Flow diagram of combustion preparative method

Metal nitrate (A.R. grade)
Aqueous solution

Metal acetate (A.R. grade)
Aqueous solution

Stoichiometric
Equimolar
Concentration

Controlled Evaporation

Pasty mass

Careful Heating

Grinding

Calcination

$AMnO_3, BaCeO_3, ZnSnO_3$

Characterization and physical
Studies. XRD, IR, AAS, BET,
SEM, Elect. Cond., ESR, Mag.
Suscp., DRS, GC, etc.

54

The two aqueous solutions were mixed in an evaporating dish and heated slowly with constant stirring on a sand bath to a pasty mass. Further careful heating involved the exothermic combustion of the substrate leading to the formation of residue. The residue was mixed and ground in a mortar and finally calcined in a muffle furnace at 700-800°C for 10-12 h. The characterization of the compounds were done by employing powder X-ray diffraction technique.

3.2 CHARACTERIZATION

Materials prepared by the above methods were characterized by powder X-ray diffraction (XRD) technique, Infra Red Spectroscopy (FTIR), Atomic Absorption Spectroscopy (AAS), B.E.T. surface area measurement and Thermal studies (TGA/DSC).

3.2.1 Powder X-ray diffraction technique

XRD patterns for the powdered samples were recorded on X-ray diffractometer (Philips PW 3710 / Rigaku), using Cu $K\alpha$ / Cr $K\alpha$ radiations, at a scanning rate of 2°/min. These compounds were identified by comparing their d_{hkl} values and the relative peak intensities obtained from diffractogrammes with those reported in JCPDS data files. The intermediate compositions, not reported, were confirmed by comparing with the end compositions.

3.2.2 Infra Red Spectroscopy

FTIR absorption spectra for all the samples were recorded on a Shimadzu IR Prestige-2 model spectrometer. The solid sample was finely ground along with pure and dry KBr, in the ratio 1:10. The mixture was pressed in a special die which was mounted on the sample holder in the sample chamber of the spectrometer. The absorption spectra was recorded in the range 300 cm^{-1} to 1500 cm^{-1}. The spectra were compared with literature and were interpreted accordingly.

3.2.3 Atomic absorption spectroscopy

Sodium contamination in the samples prepared by co-precipitation technique was determined by using an atomic absorption spectrometer. About 250 mg of powdered sample was dissolved in 25 ml of pure HCl which was further diluted to the required concentration using deionised water. The total amount of sodium was determined by comparison with the standard. Sodium contamination in these samples was found in the range 0.2 to 0.4% by weight.

3.2.4 B.E.T. Method (Surface area measurement)

Surface areas of the samples under study were determined using B.E.T. nitrogen adsorption method, employing SMARTSORB-92/93 model Surface Area Analyzer. Specific surface areas of the catalysts were calculated with the help of well known Brunauer, Emmet and Teller (BET) expression:

$$\frac{P}{V(P_o-P)} = \frac{1}{V_m C} + \frac{(C-1)}{V_m C} \times \frac{P}{P_o} \qquad \text{------------------(1)}$$

Here 'P' is the equilibrium pressure, 'P_0' is the saturated vapor pressure of the gas at the temperature of adsorption, 'V' is the volume of the adsorbed gas at S.T.P., 'V_m' is the volume of the gas at S.T.P. required to form a monolayer and 'C' is the constant related to the heat of adsorption. The quantities P, P_0 and V can be determined experimentally. The plot of P/V (P_0-P) versus P/P_0 is a straight line with slope $S = C-1/V_m$ C and intercept $I = 1/V_m$ C, which proves the validity of equation (1). V_m and C can be obtained from the above plot.

From equation (1) it can be shown that $V_m = 1/S+I$ and $C = S/I+1$. Since V_m is the volume of the gas at 273 K and 1 atm pressure necessary to cover the surface with single layer it can be converted into the number of molecules involved. Assuming 16.2 A° as the value of the cross sectional area of single nitrogen molecule at liquid nitrogen temperature, Brunauer, Emmet and Teller have shown that,

$$\text{Surface Area} = 4.38 V_m \text{ (c.c., S.T.P.) } m^2/g \quad \text{---------------- (2)}.$$

3.2.5 Thermal studies (TGA/DSC)

Thermal study of the co-precipitated hydroxide precursors of the perovskites was carried out employing NETZSCH Geratebau GmbH Thermal Analyzer (STA 409PC). Around 10 to15 mg of the powdered hydroxide precursor sample weighed in an alumina crucible covered with lid was mounted on a sample holder of the analyzer which is then operated in the temperature range 30 to 800°C. Thermal gravimetric analysis (TGA) and Differential scanning calorimetry (DSC) patterns during heating were recorded. TGA pattern was used to interpret the heat effects

associated with the physical and chemical changes and the behaviour of weight loss of the precursor sample. The thermal effect, exothermic or endothermic preceding physical and chemical changes were studied using DSC patterns.

3.3 PHYSICAL AND SPECTROSCOPIC STUDIES

Different physical and spectroscopic studies like electrical resistivity, magnetic susceptibility, saturation magnetization, electron spin resonance, diffuse reflectance spectroscopy and scanning electron microscopy were performed on the prepared samples using suitable techniques.

3.3.1 Electrical resistivity measurements

Electrical resistivity measurements of all the samples were carried out to study the conductivity behaviour of the samples and to establish the possible relationship with the catalytic activity.

The dc electrical resistivities of the samples were measured in air using a two probe method during cooling cycles in the temperature range 400-30°C. Pellets of the powdered samples with 10 mm diameter and 2 to 3 mm thickness under a pressure of 5000 kg/cm² were made. The pellets were heated at 800°C for 18-20 h. These were silver pasted on either side. The pellets were fitted between the polished electrodes of a two-probe conductivity cell suspended within a furnace. The constant voltage of 3 V was supplied to the cell and the varying current at different temperatures was noted on KEITHLEY make multimeter. Electrical resistivities at different temperatures were calculated during the cooling cycle.

3.3.2 Magnetic susceptibility measurements

The magnetic susceptibility 'χ_g' measurements of the samples in air at room temperature were done using Gouy method. During the measurements, magnetic field of the order of 8000 gauss was used. Mercury tetrathiocyanatocobaltate {Hg [Co (SCN)$_4$]} as a standard material with the known magnetic susceptibility 'χ_g' (16.44 x 10^{-6}) and sensitive analytical balance of DONA make were employed. The sample tube was washed, dried and hanged between the electromagnets of the Gouy balance. The weight of the tube was recorded before and after applying the magnetic field. The sample tube was filled with the standard material up to a certain mark and was weighed on Gouy balance before and after applying the field. The procedure was repeated with the sample whose 'χ_g' was to be determined. The magnetic susceptibility of the sample was found out by using the following calculations:

In the first part, tube constant or β - constant was calculated with the known 'χ_g' value of the standard material, using the relation,

$$\beta \text{ - Constant} = \chi_g \cdot \frac{W}{\Delta W} \quad (\chi_g = 16.44 \times 10^{-6}).$$

$W = (W_3 - W_1) =$ Weight of the standard material taken and $\Delta W = \Delta W' \pm \Delta W''$

$\Delta W' = (W_4 - W_3)$ and $\Delta W'' = (W_1 - W_2)$

$W_1 =$ weight of empty tube,

$W_2 =$ weight of the empty tube with field,

$W_3 =$ weight of the tube with standard substance and

$W_4 =$ weight of the tube and standard substance with field.

In the second part, substituting β - constant value in the above relation, 'χ_g' of the sample under study was calculated. Molar susceptibility(χ_M) of the samples were calculated using the relation:

$\chi_M = \chi_g$. Molecular weight of the sample

The magnetic moment (μ_{eff}) of the samples was found out using the formula:

$\mu_{eff} = 2.84 \sqrt{\chi_M . T}$ B.M., where T = absolute temperature. With these values, the number of unpaired electrons in the samples were calculated.

3.3.3 Saturation magnetization study

Saturation magnetization study was done on selected magnetic samples, using high field hysteresis loop tracer described by Likhite et. al.[190]. The three major components of the loop tracer are electromagnet, pick-up coil and balancing with integrating circuits.

The electromagnet works at 50 Hz mains frequency. The alternating magnetic field of about 3600 Oersted is produced in an air gap of about 1 cm, in the instrument. A special balancing coil is used to measure the saturation magnetization of the sample in the air gap. Pick-up coil produces a field proportional to the magnetic induction in the sample. The supporting coil produces a signal that is equivalent to the strength of the magnetic field. The signal is displayed as a hyteresis loop on the screen of an oscilloscope. A digital AC voltmeter connected to the output displays the peak or RMS value of the signal proportional to the saturation magnetization in millivolts. The calibration of the vertical scale corresponding to the

magnetization value is done using nickel as a standard substance having magnetization of 53.34 emu/g. The saturation magnetization values, σs in emu/g of the magnetic samples were found out.

3.3.4 Electron spin resonance (ESR) study

Electron spin resonance occurs when a spinning electron in an externally applied magnetic field absorbs sufficient electromagnetic radiation to cause the inversion of spin state of the electron. This phenomenon is exhibited by a paramagnetic species and is also referred as electron paramagnetic resonance and as electron magnetic resonance.

ESR study of the samples was carried out at room temperature at X-band using a Varian E-112 X-band spectrometer to get an insight of the catalytically active and paramagnetic species. During the measurements, the magnetic field of the strength 3000 gauss was employed. The energy level difference due to electron spin was 6.1×10^{-17} ergs (or about 1.5×10^{-24} calories) and frequency 'ν' was 9.2 GC (Giga cycles or 10^9 cycles per sec). This frequency lies in the microwave region of the electro magnetic radiation spectrum. The sample was mounted in a quartz tube and TCNE was used as a field calibrant, taking its g-value as 2.00277. Spectroscopic splitting factor (g) or gyromagnetic ratio was obtained from the following relation:

$$\mu = - g\beta s$$

where 'μ' is the magnetic moment, 'β' is the Bohr magneton (ergs/gauss) and 's' is the spin of electron +1/2 or -1/2.

3.3.5 Scanning Electron Microscopy

Scanning Electron Micrographs of powdered materials of some samples were taken on microscope (JEOL make, model JSM 5800 LV). Interpretation of the surface morphology and the calculation of the average particle size of the compounds were done with the help of the micrographs.

3.3.6 Diffuse Reflectance Spectroscopy (DRS)

Diffuse reflectance spectra of the samples were recorded in the wavelength range 300 to 700 nm, using UV-visible spectrometer (SHIMADZU model no. 2450). Powdered reference sample of BaSO4 and the sample under consideration were fitted into the sample holders which were mounted on a stand in sample chamber and the spectra were recorded. The spectra were used to calculate the band gap energy possessed by the samples. On the basis of the band gap energy, the conducting behaviour and the catalytic activity of the samples were visualized.

3.4 CATALYTIC STUDIES

Perovskites and the supported metal oxides were tested for a model CO oxidation reaction with oxygen using AMIL-NUCON series gas chromatograph (GC) on line for the analysis of the reactants and the products. Experimental set up for online analysis is shown in fig. 3.3. Hydrogen was used as a carrier gas with a constant flow rate of 30 ml/min. Porapak Q as a reference column and molecular sieve 13x as a column for CO oxidation analysis of the reactants and the products were used. Injector and detector were operated at a temperature of 60°C and oven at

50°C. Through out the reaction studies constant current flow of 150 mA was supplied to the thermal conductivity detector (TCD). GC used is equipped with eight port valve to inject the gaseous samples for the on line analysis. The analyzed data were recorded on Omniscribe recorder at an appropriate chart speed to obtain qualitative and quantitative information of the reaction under study.

CO gas used for the catalytic reaction was prepared in the laboratory by drop wise addition of formic acid (A.R. grade) to the warm sulphuric acid in a specially designed glass reactor. The evolved gas was bubbled through 20% NaOH solution, also through molecular sieve and finally dried over calcium chloride. Prepared CO gas was found to be highly pure as confirmed by GC. Pure oxygen, nitrogen and hydrogen gases were used from commercial cylinders.

Reaction studies were carried out in a continuous flow fixed bed glass reactor in which around 1 g of powdered catalyst was supported in between glass wool plugs and glass beads on either side. The catalyst activity was determined using gas feed composition of 5% CO, 5% O_2 and 90% N_2. The individual gas flow rates were controlled using flow meters and precision needle valves. CO oxidation was checked at various catalyst temperatures point by point measurement from room temperature to 400°C. The total flow rate used was 5000 ml/h. By using a three way valve the provision was made to pass the reactants to GC, without passing through the catalyst. At regular intervals the products were injected into the GC which were analyzed by molecular sieve 13x and detected by the TCD.
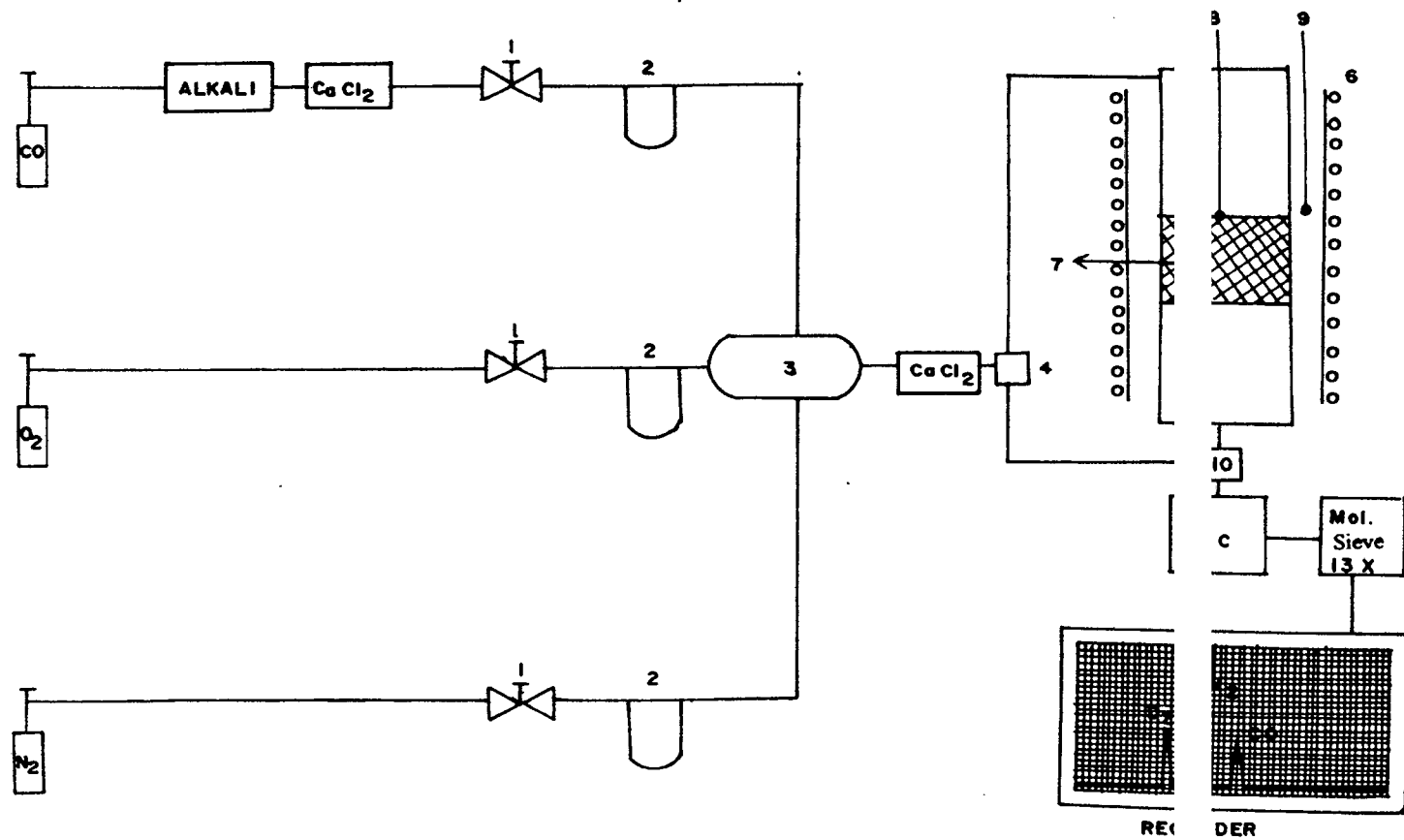
Fig. 3.3. Schematic diagram of the experimental reaction set up.
1. Fine control needle valve, 2. Flow meter, 3. Mixing bulb, 4. Two way valve,
5. Glass reactor, 6. Electric furnace, 7. Catalyst bed, 8. Thermocouple T_1,
9. Thermocouple T_2, 10. Eight port valve.

The analysis of the reaction products at different temperatures was used to evaluate the temperature dependent CO oxidation efficiency of the catalysts and kinetics of CO oxidation over the catalysts. The reactions were also used to study CO oxidation cycles over the catalysts and to study the life of these catalysts.

CHAPTER 4

SOLID STATE STUDIES

SOLID STATE STUDIES

The various solid state experimental studies such as structural characterization (Powder X-ray diffraction, FTIR spectroscopy, atomic absorption spectroscopy, B.E.T. surface area, thermal studies and scanning electron microscopy), electrical resistivity, magnetic susceptibility, saturation magnetization, electron spin resonance and diffuse reflectance spectroscopy were carried out. The comparison of different results were undertaken and discussed on the basis of the experimental data.

4.1 X-RAY DIFFRACTION ANALYSIS

The formations of monophasic perovskites were checked by recording the powder X-ray diffractogrammes of all the samples such as $Zn_{1-x}Ni_xMnO_3$ (x = 0, 0.2, 0.4, 0.6, 0.8 and 1.0), $AMnO_3$ (A = Sr, Sm, and Nd), $BaCeO_3$ and $ZnSnO_3$. The d- spacing and intensities corresponding to 2θ obtained from the diffractogrammes, on comparing with the values reported in the literature (JCPDS data file) were found to be in good agreement. The- d spacing of the intermediate compositions not reported in literature were compared with the end members namely $ZnMnO_3$ and $NiMnO_3$.
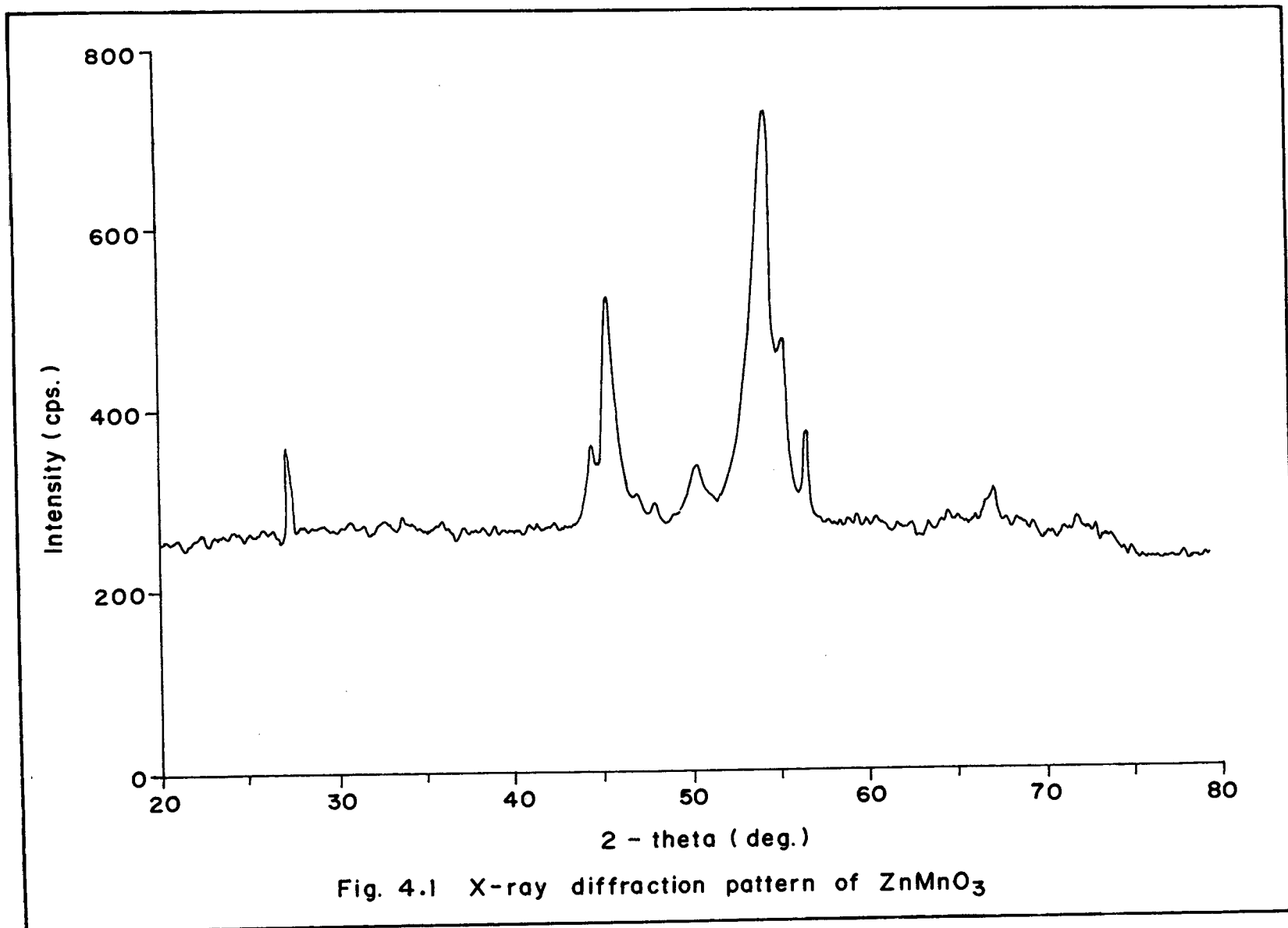
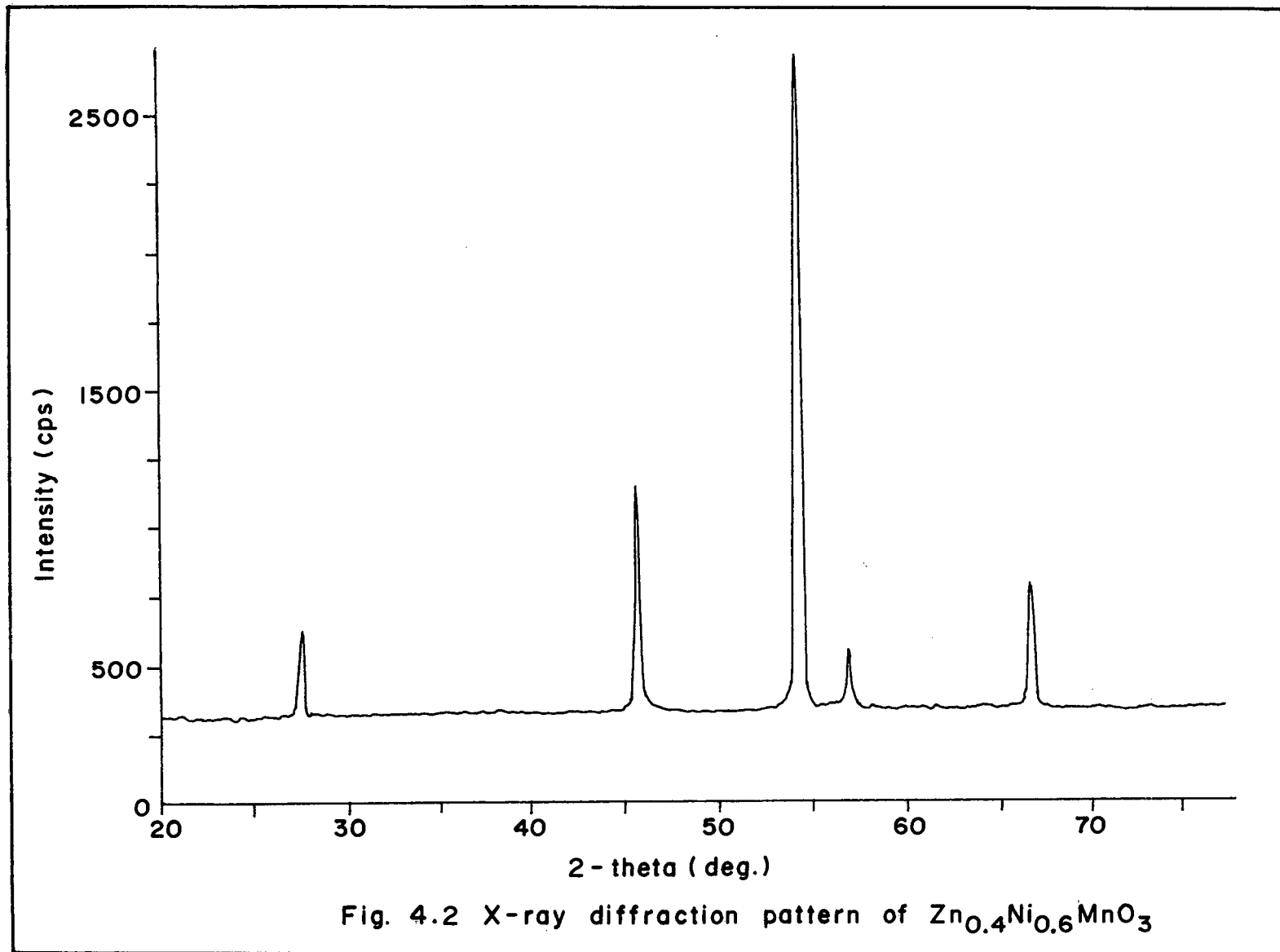Figures 4.1 - 4.5 show X-ray diffraction patterns of some of the representative samples.

Chamberland et. al.[191] have reported hexagonal $ZnMnO_3$, prepared at 65 kbar and 900°C. However, our results of X-ray analysis on comparison found to be in good agreement with the values reported in JCPDS data file and indicated that $ZnMnO_3$ is cubic. $NiMnO_3$, prepared by Whittingham et. al.[192] at 200°C is reported to have orthorhombic structure. $NiMnO_3$ prepared by us is found to be rhombohedral. This is in agreement with the rhombohedral structure of $NiMnO_3$ prepared by Feltz et. al.[193] at 700°C. The transition from orthorhombic to rhombohedral phase may be because of the higher temperature of preparation.
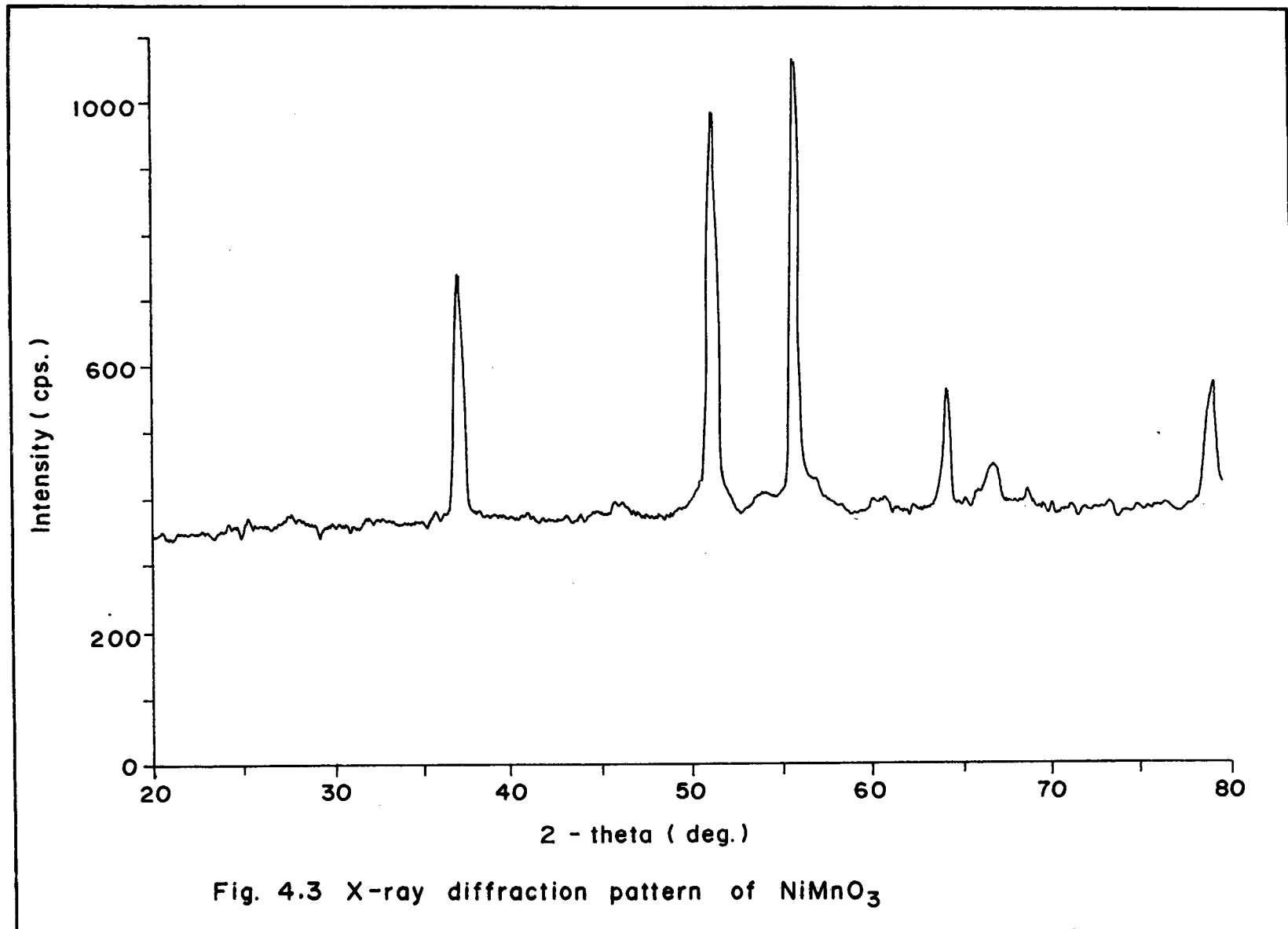
$SrMnO_3$ reported by T. Negas and R.S. Roth[194] has a hexagonal unit cell, the dimensions of which ($a_n = 5.449$ A°, $c_n = 9.080$ A°) indicate a mixed hexagonal/cubic close packing of the SrO_3 layers. Heating $SrMnO_3$ at 1360°C in air for 200 h, followed by rapid quenching transforms it to orthorhombic phase. Thus, heating at higher temperature transforms $SrMnO_3$ from hexagonal to orthorhombic phase. XRD pattern of $SrMnO_3$ prepared by us showed that it has hexagonal structure. $SmMnO_3$, $NdMnO_3$ and $BaCeO_3$ are observed to have orthorhombic structure. XRD patterns of supported oxides show the peaks of Fe_2O_3 and NiO besides the peaks of the support i.e. ZnO.
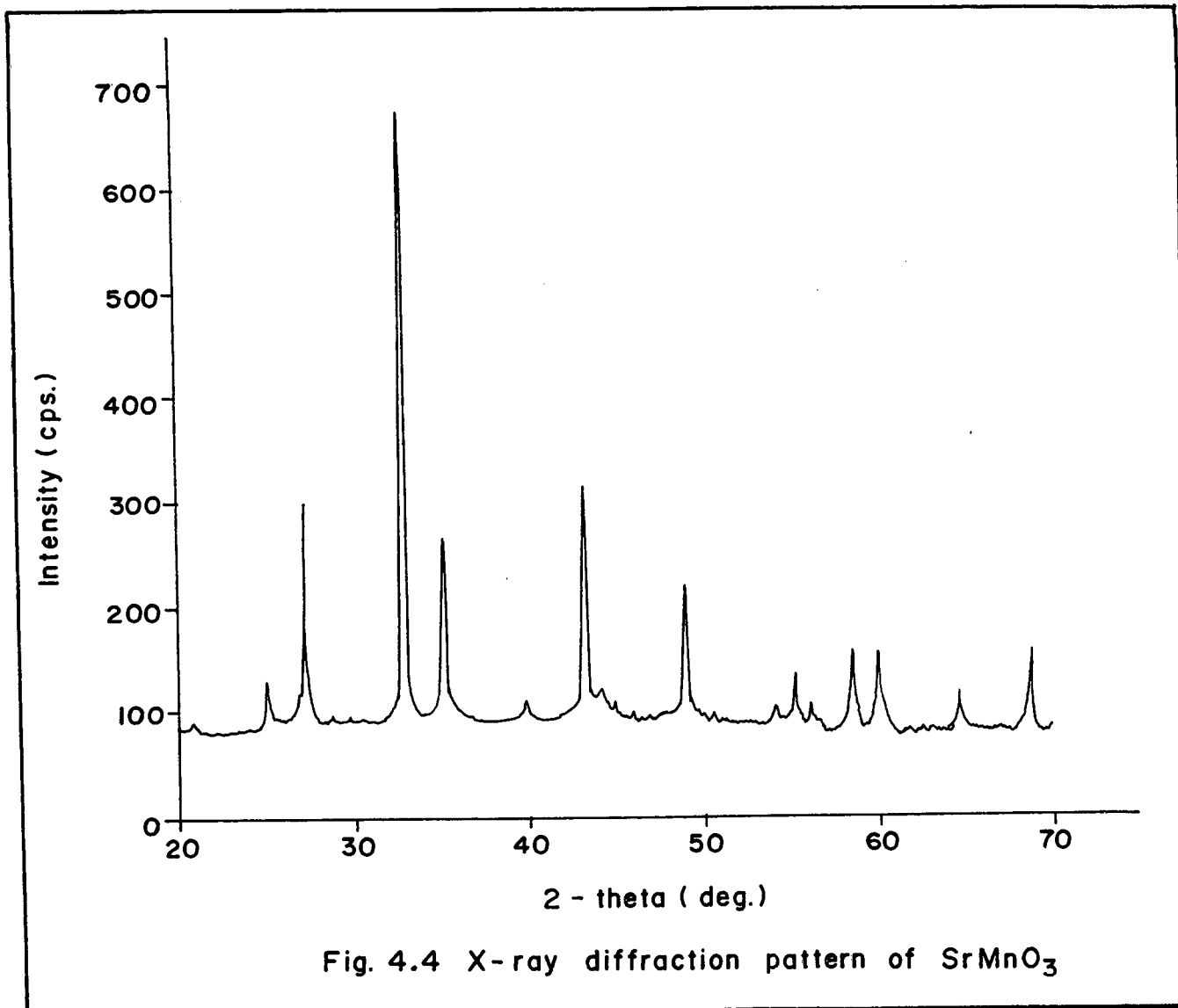
The average particle size for all the samples was calculated from the X-ray line widths through the classical Scherrer formula, $D_{hkl} = K\lambda/B \cos\theta$, where D_{hkl} is the diameter of the particle, K is a constant (shape factor~0.9), B is the width of the

67

Fig. 4.1 X-ray diffraction pattern of ZnMnO₃

Fig. 4.2 X-ray diffraction pattern of $Zn_{0.4}Ni_{0.6}MnO_3$

Fig. 4.3 X-ray diffraction pattern of $NiMnO_3$

Fig. 4.4 X-ray diffraction pattern of SrMnO₃
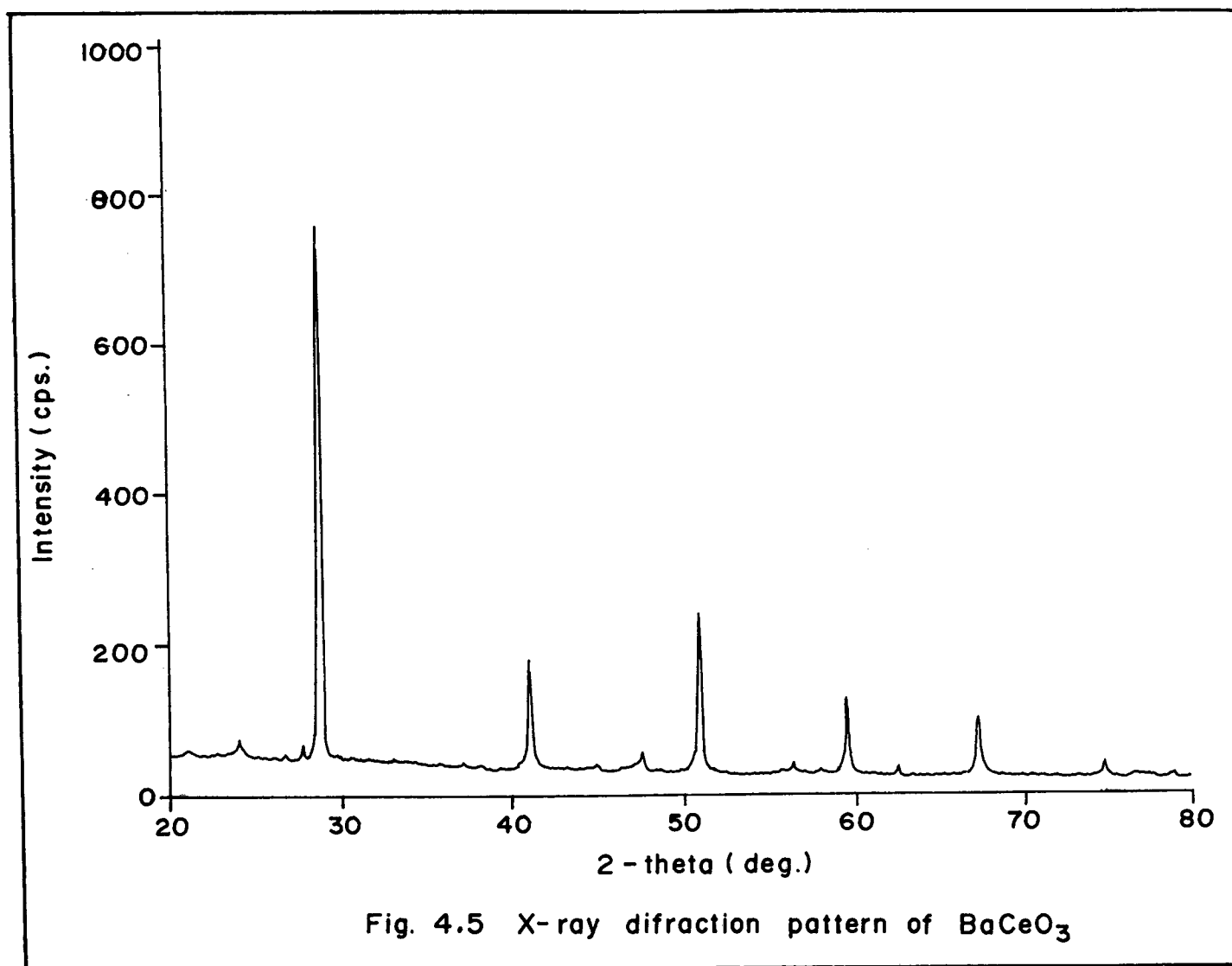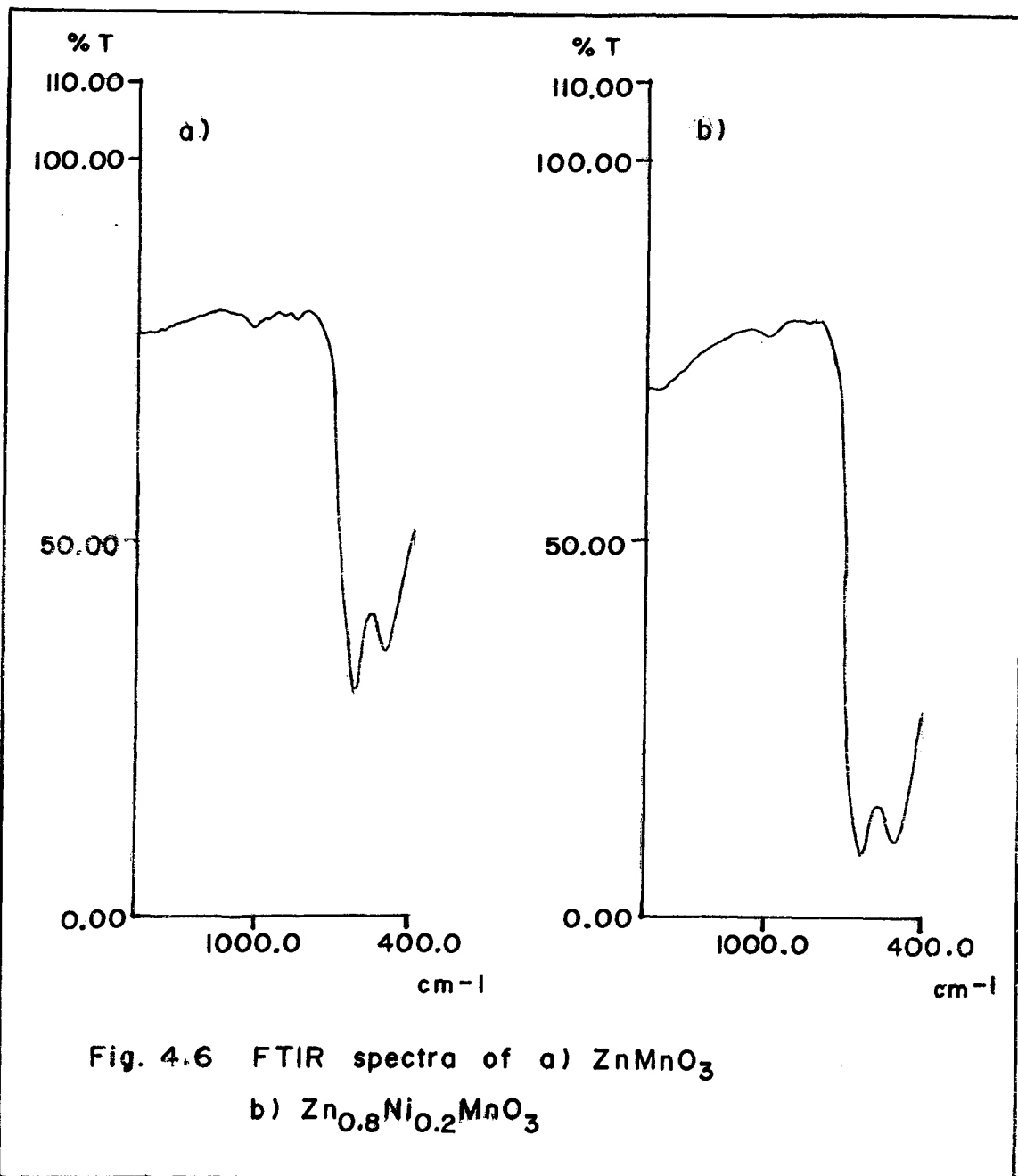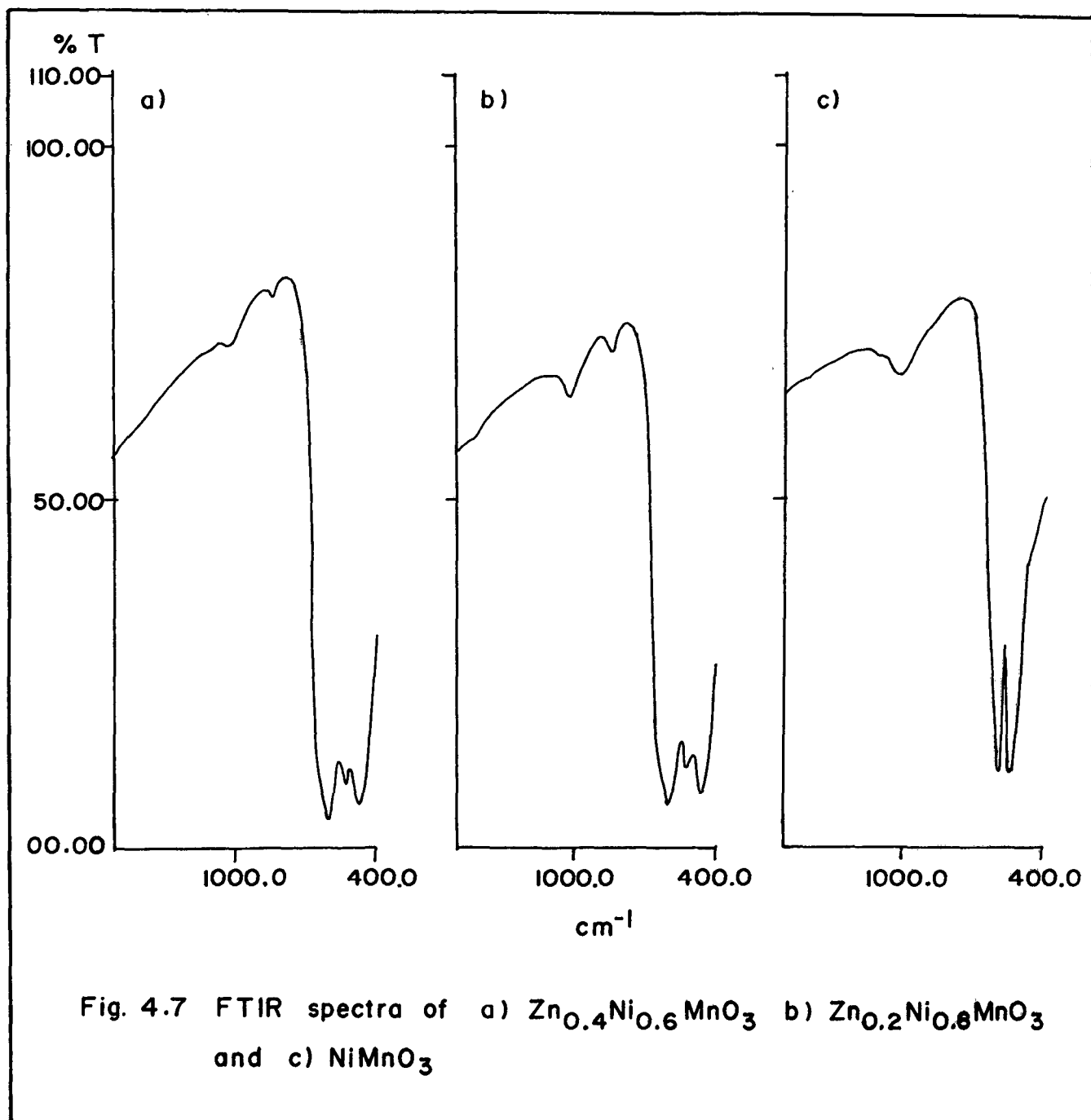
Fig. 4.5 X-ray difraction pattern of BaCeO$_3$

half-maximum of the peaks, λ is the wavelength of the X-rays and θ is the Bragg's angle. The average particle size of $Zn_{1-x}Ni_xMnO_3$ series compounds were found in the range 30-50 nm and the average particle size for $AMnO_3$ (A=Sr, Sm and Nd), $BaCeO_3$ and $ZnSnO_3$ lies in the range 80-100 nm.

4.2 FTIR SPECTROSCOPY

The perovskite structure is characterized by IR spectra[95-101] in the region 1000 to 300 cm^{-1}. In IR spectra of the perovskites two absorption bands were observed in the region 700 to 400 cm^{-1} corresponding to the stretching vibration of metal-oxygen bonds as shown in figures 4.6 and 4.7. The lower frequency band has been assigned to the deformation mode of BO_6 (B = B-site metal) octahedra i.e. the B-O-B bond angles of the perovskite structure. The frequency of these bands has been related to the strength of metal-oxygen covalency[102].

From these spectra, it is observed that as the substitution of Ni ion at A site increases, the higher frequency band observed at 619 cm^{-1} remains undisturbed for compositions from x = 0.0 to 0.8. This indicates no change in Zn-O covalency of the perovskites for these compositions. For x = 1 composition, the strong peak gets shifted to 585 cm^{-1} revealing that Zn-O covalency at A-site has been substituted by Ni-O covalency in $NiMnO_3$. For compositions from x = 0.0 to 1.0, the lower frequency band of MnO_6 octahedra is gradually shifted from 495 to 425 cm^{-1}, due to the increasing e_g electron density in the antibonding orbitals.

Fig. 4.6 FTIR spectra of a) $ZnMnO_3$
b) $Zn_{0.8}Ni_{0.2}MnO_3$

Fig. 4.7 FTIR spectra of a) $Zn_{0.4}Ni_{0.6}MnO_3$ b) $Zn_{0.2}Ni_{0.8}MnO_3$ and c) $NiMnO_3$

For compositions of x = 0.6 and 0.8, shoulder peak appears at 540 cm^{-1}, the length of which increases with the increasing value of x. Similar frequency bands were also observed in the spectra of the other perovskite compositions.
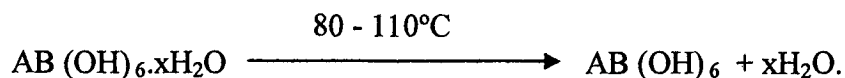
4.3 THERMAL STUDIES

To find out the decomposition temperature of hydroxides and the initiation of solid-state reaction, the co-precipitated hydroxide precursors were subjected to thermal studies. TGA/DSC thermogram patterns of representative samples are shown in figures 4.8 - 4.11.

Thermal studies show that there are three major steps in the decomposition process. They are a) Loss of moisture, b) decomposition of hydroxides to corresponding oxides and c) solid-state diffusion reaction leading to the formation of perovskite.

In these thermograms, DSC patterns show endothermic peaks at 80 - 110°C, due to the loss of moisture corresponding to the weight loss observed in TGA patterns. Decomposition of hydroxide precursors to the corresponding oxides is shown by the endothermic peaks of the DSC patterns at around 300°C. TGA patterns show the corresponding weight loss.

The probable reactions taking place during heating may be represented by the following scheme:

$$AB\,(OH)_6.xH_2O \xrightarrow{\;\;80-110°C\;\;} AB\,(OH)_6 + xH_2O.$$
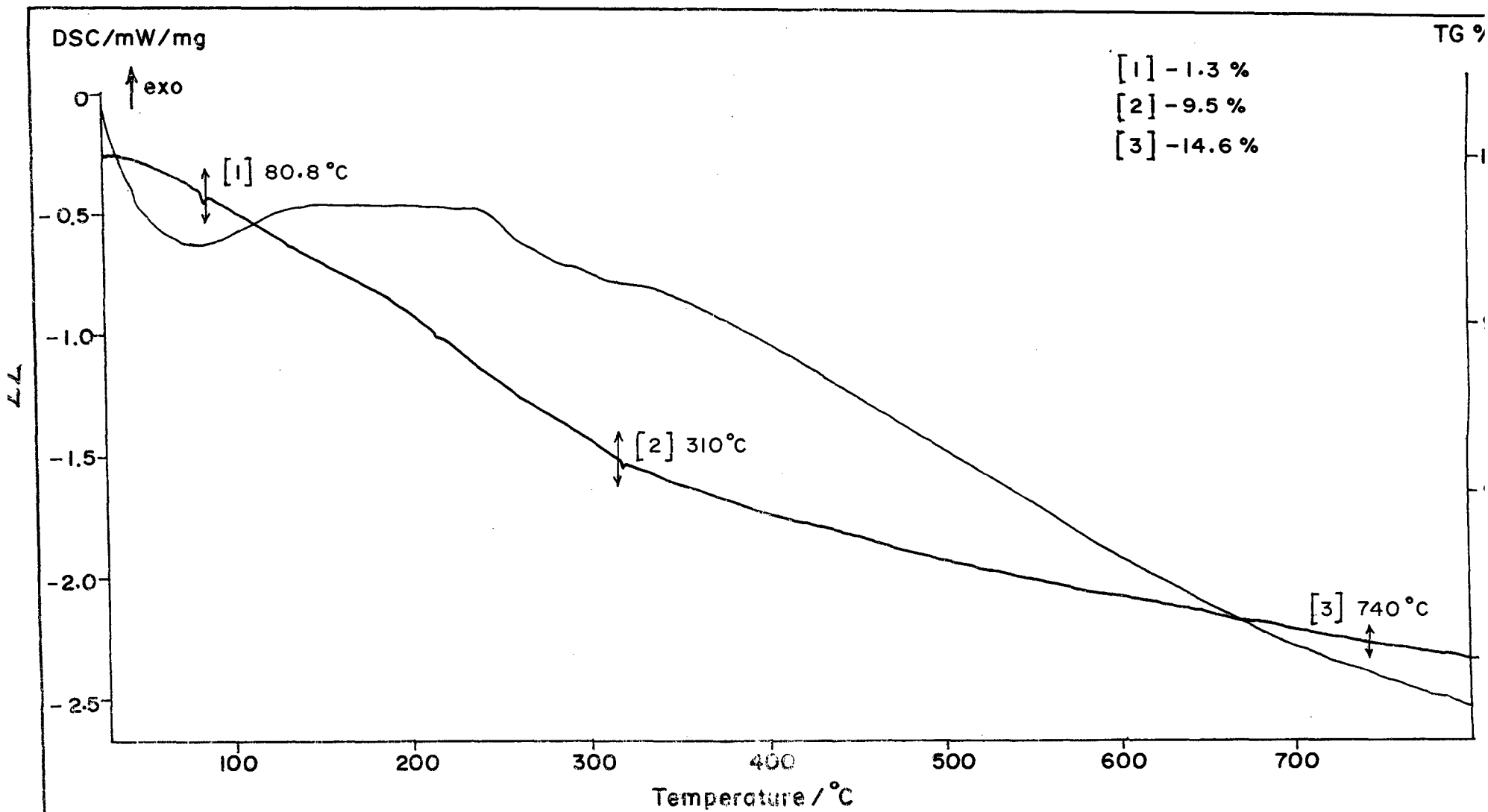
Fig. 4.8 TGA / DSC curves of $Zn_{0.8}Ni_{0.2}Mn(OH)_6 \cdot XH_2O$ precursor.

DSC/mW/mg

0

↑ exo

-0.5

[1] 79.5°C

-1.0

-2.0

[2] 310°C

-3.0

[3] 740°C

-4.0

TG %

[1] – 1·2 %
[2] – 10.5 %
[3] – 16.4 %

10

9

9(

8!

100   200   300   400   500   600   700

Temperature / °C
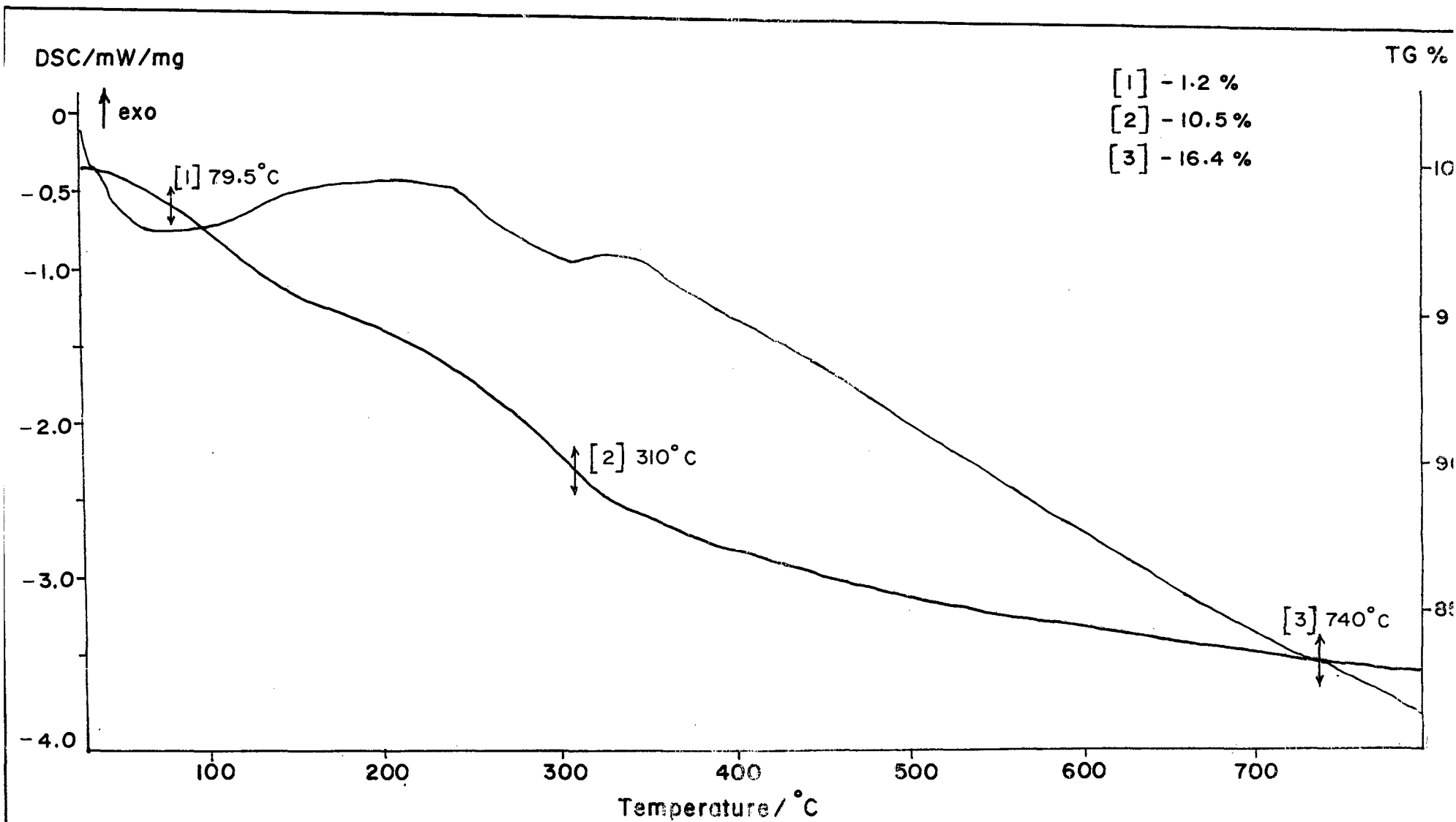
Fig. 4.9 TGA / DSC curves of $Zn_{0.6}Ni_{0.4}Mn(OH)_6 \cdot X H_2O$ precursor.
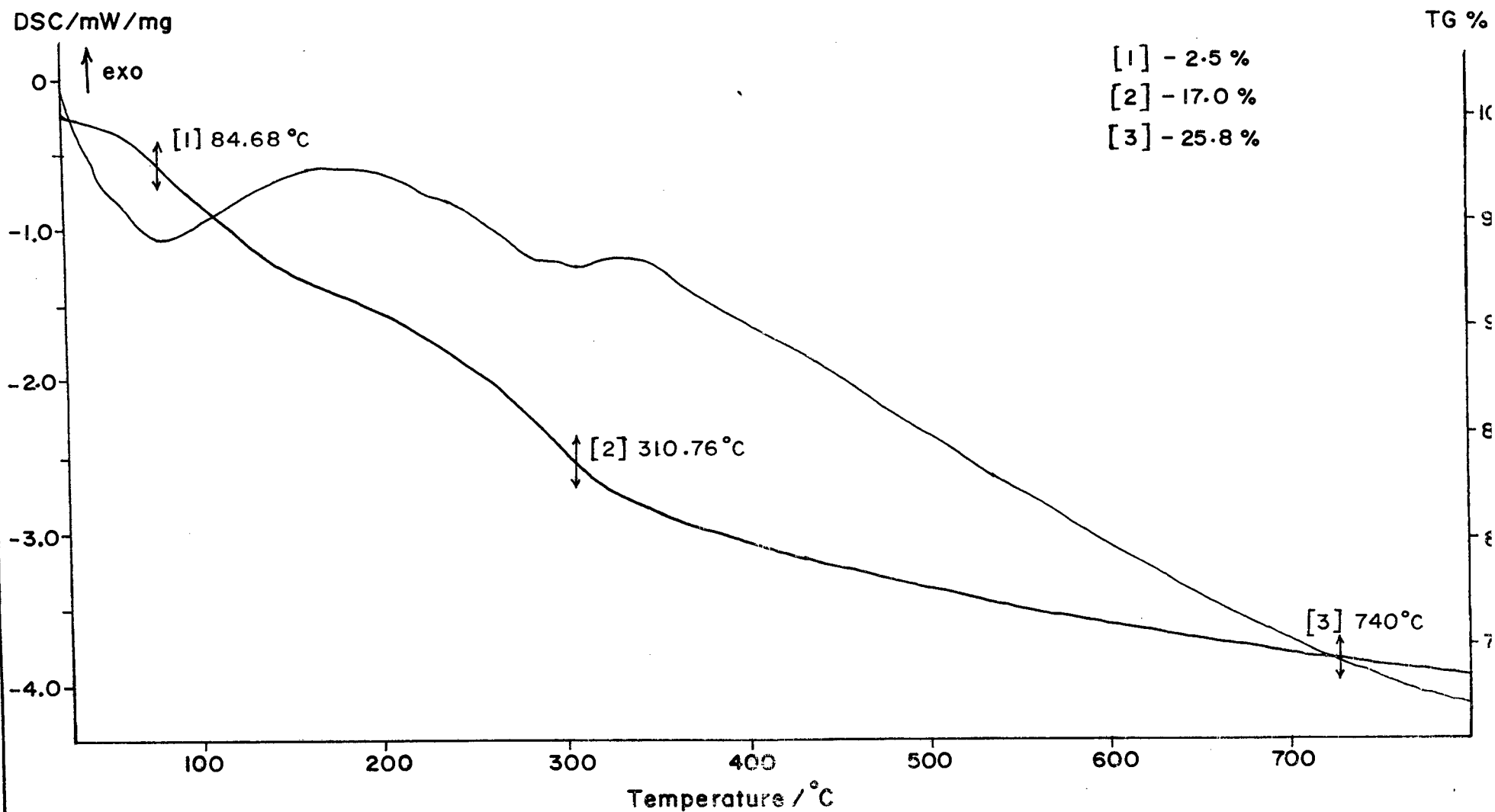
Fig. 4.10 TGA / DSC curves of $Zn_{0.4}Ni_{0.6}Mn(OH)_6 \cdot X H_2O$ precursor.

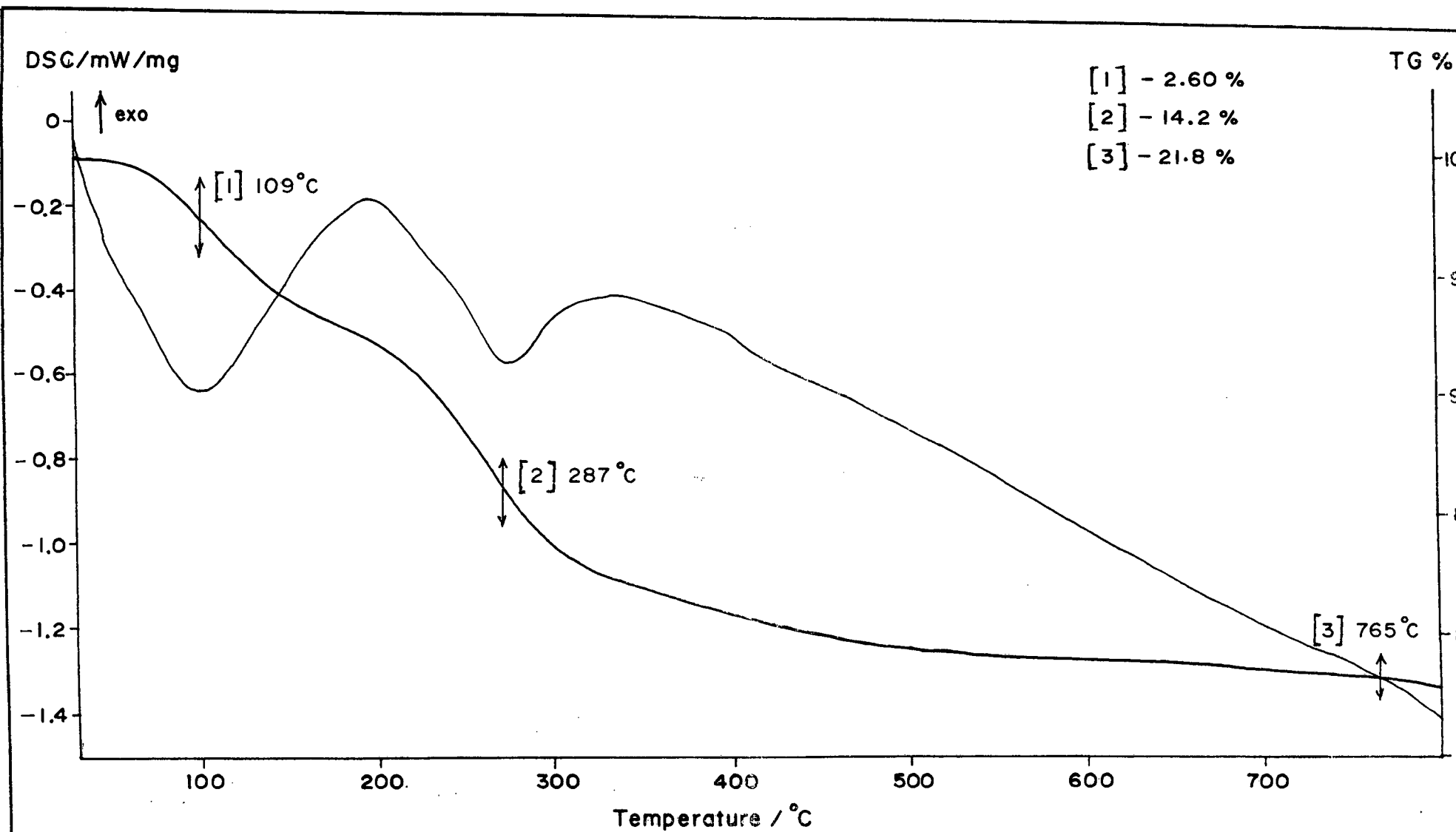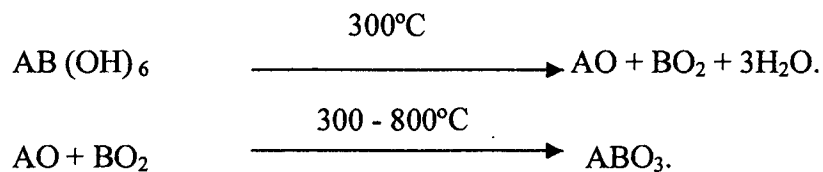Fig. 4.11 TGA / DSC curves of NiMn(OH)$_6$·XH$_2$O precursor

$$AB(OH)_6 \xrightarrow{\quad 300°C \quad} AO + BO_2 + 3H_2O.$$

$$AO + BO_2 \xrightarrow{\quad 300 - 800°C \quad} ABO_3.$$

where A and B are the transition metal ions.

4.4 ELECTRICAL RESISTIVITY MEASUREMENTS

Electrical resistivity of the different samples measured in air using two probe method during cooling cycles, from 400°C to room temperature were found to be in the range of semiconductors. Plots of resistivity ($\log\rho$) versus temperature (1000/T) are shown in figures 4.12 - 4.15. Resistivity is found to increase linearly with the decrease in temperature for all the compositions studied.

According to Verwey and co-workers[195], for high electrical conductivity in transition metal oxides, the material must contain cations of the same element with oxidation number differing by unity, situated at a similar site in crystal structure which are called as mixed valence semiconductors. From literature it is seen that B-site cations are responsible for electrical conductivity in perovskites by virtue of symmetry. The more significant B-B interactions determine the electrical conduction. From this it can be said that conductivity in manganite perovskites is due to manganese ions present on the Oh site of the lattice. Thus, the observed conductivity in manganite compositions could be explained on the basis of Mn^{3+}- Mn^{4+} ion pair association which is in agreement with many authors[196-200].
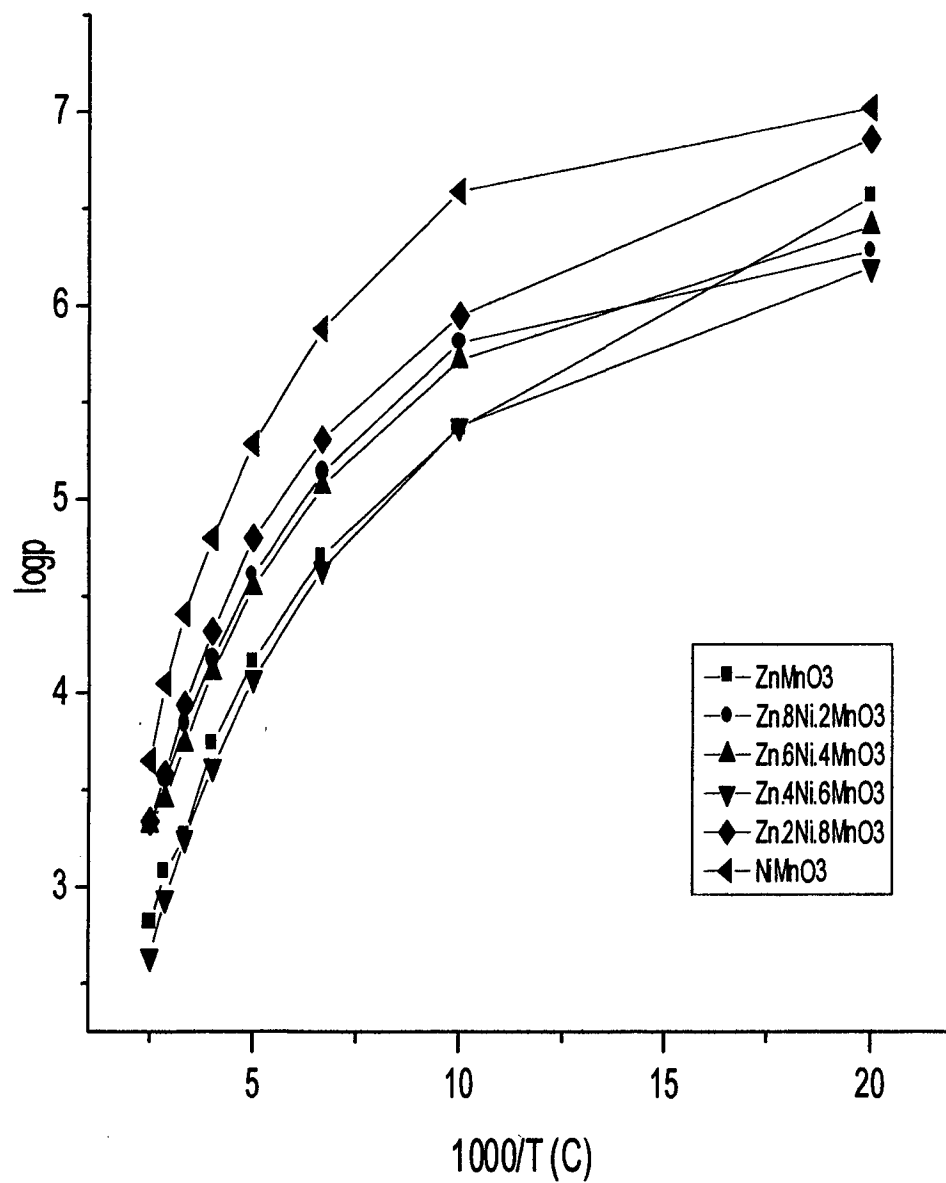
Figure 4.12 Variation of Electrical Resistivity of Series-I compositions with temperature.
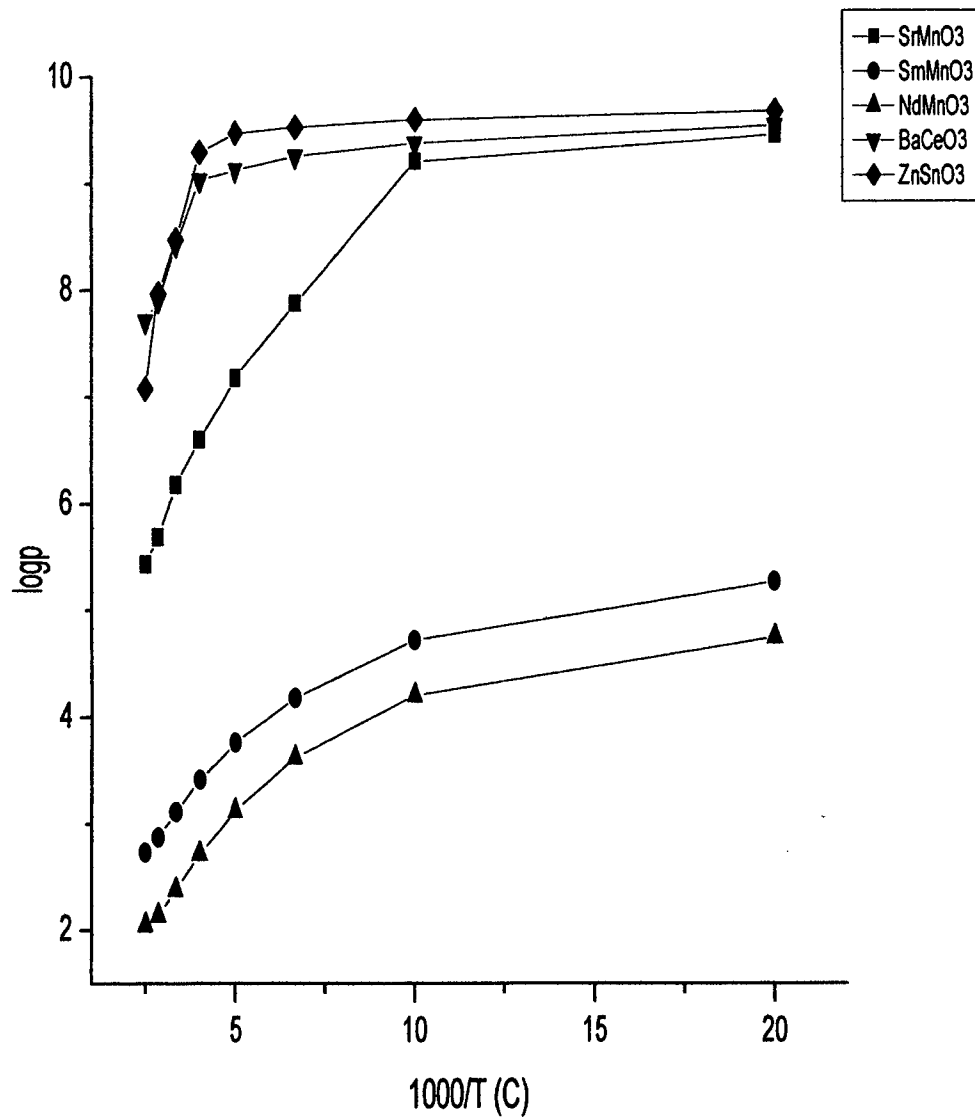
Figure 4.13 Variation of Electrical Resistivity of Series-II compositions with temperature.
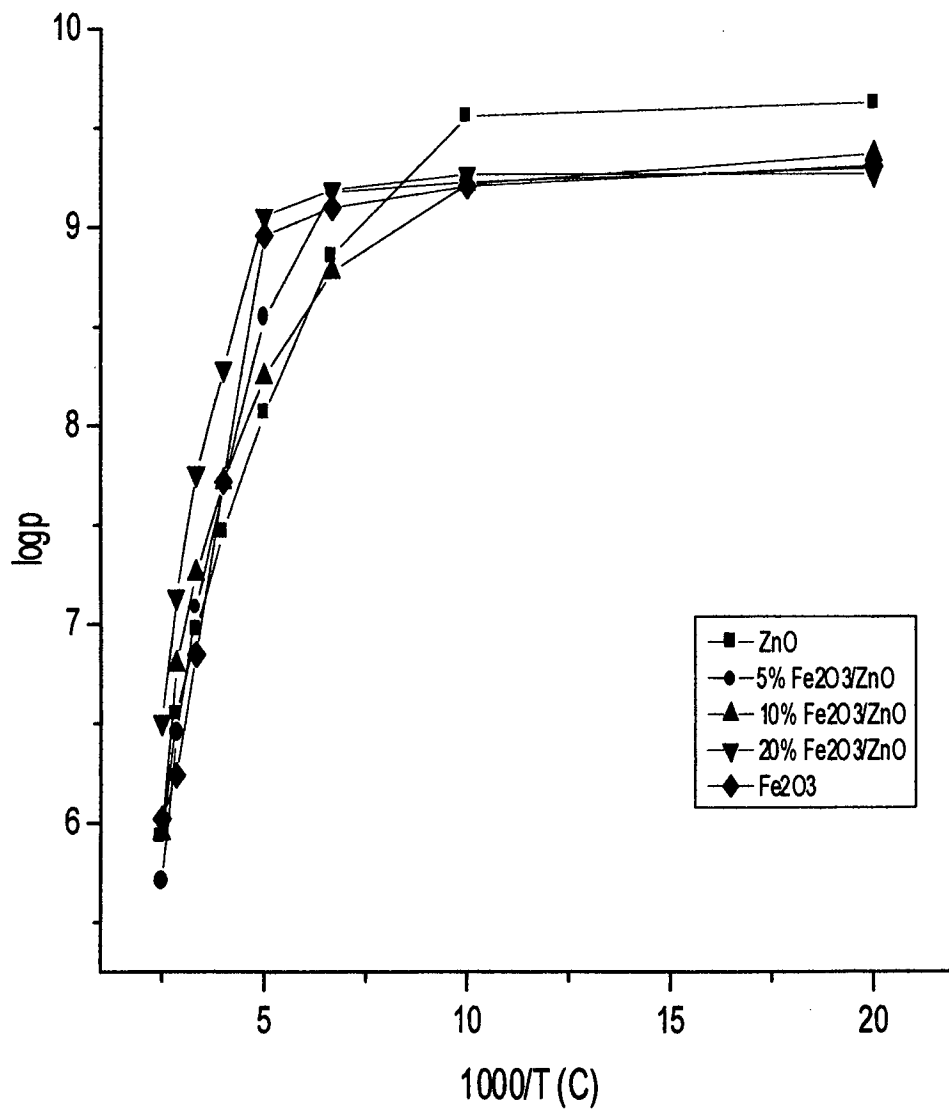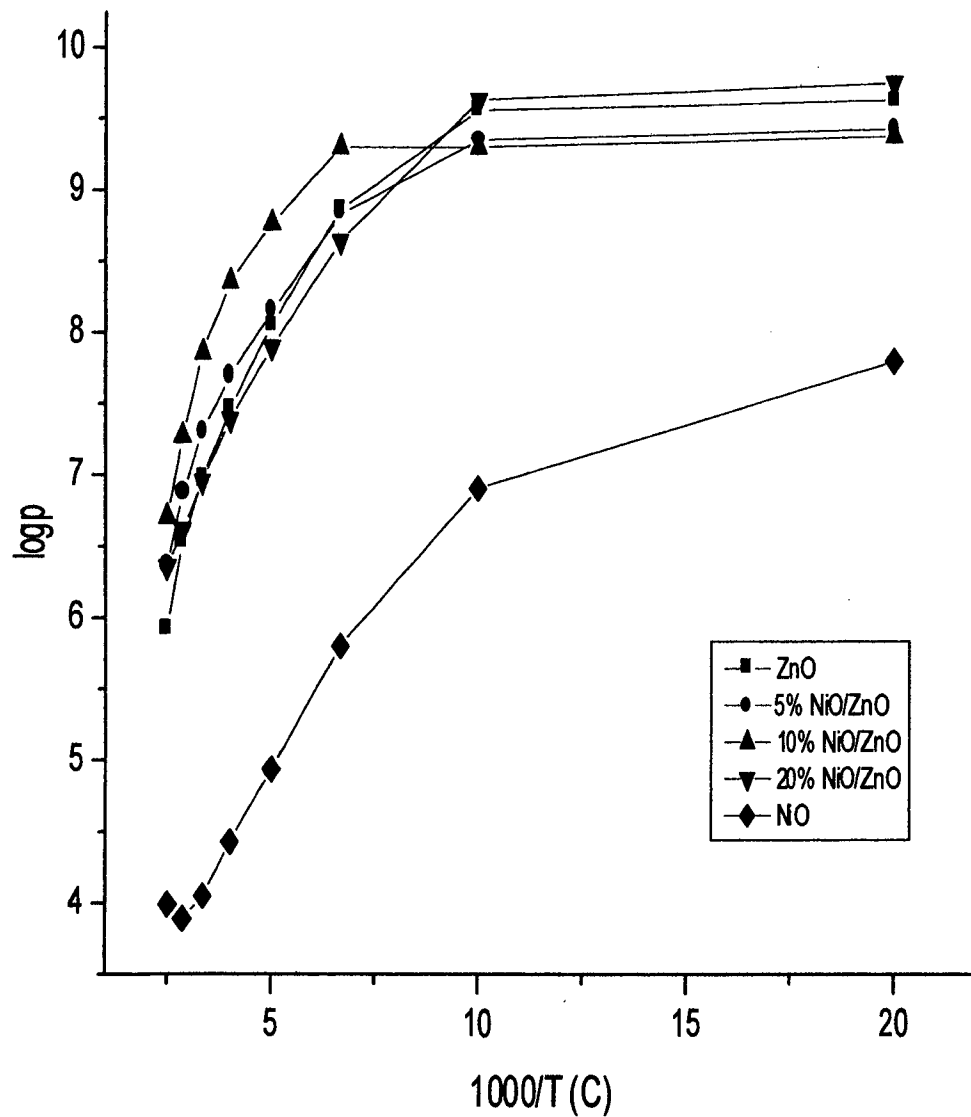
Figure 4.14 Variation of Electrical Resistivity of Series-III compositions with temperature.

Figure 4.15 Variation of Electrical Resistivity of Series-IV compositions with temperature.

Electrical conductivity in perovskites is also found to depend on site symmetry. Jorge et. al.[74] reported the possible explanation for the lower resistivity values of the perovskite compound, which is related to a less distorted structure.

In $Zn_{1-x}Ni_xMnO_3$ series, as seen in fig. 4.12, a typical semi conducting behaviour, approximately between 400 to 50°C has been observed for all the compositions. This may be because of the gradual decrease in the concentration of Mn^{3+}- Mn^{4+} ion pairs with the decrease in temperature. In this series, the difference in electrical resistivity of the compositions can be explained on the basis of symmetry distortions. Thus, cubic $ZnMnO_3$ which is less distorted than the rhombohedral $NiMnO_3$ shows lower electrical resistivity. From 50°C to room temperature, negligible change in resistivity of the compositions is observed.

Fig. 4.13 shows that the resistivity of $SmMnO_3$ and $NdMnO_3$ varies in the range 10^5 to 10^2 Ωcm from room temperature to 400°C. For $SrMnO_3$, resistivity variation range is 10^5 - 10^9 Ωcm. The difference in the resistivity variation range of these compounds can be correlated to the difference in their structures. Orthorhombic structure of $SmMnO_3$ is slightly distorted than the orthorhombic $NdMnO_3$, because of the smaller Sm^{3+} ion. Thus the observed resistivity for $SmMnO_3$ is slightly higher than that is for $NdMnO_3$. $SrMnO_3$ shows higher electrical resistivity variation range because of its hexagonal structure. $BaCeO_3$ and $ZnSnO_3$ both having orthorhombic symmetry show higher electrical resistivity. This cannot be explained on the basis of symmetry. These perovskites have extra stable Ce^{4+} and Sn^{4+} configurations respectively. Thus, the lower conductivity of $BaCeO_3$ and

$ZnSnO_3$ may be due to the lower concentrations of Ce^{3+}- Ce^{4+} and Sn^{2+}- Sn^{4+} ion pairs.

As shown by fig. 4.14, compositions of Fe_2O_3/ZnO series exhibit electrical resistivity variation from 10^6 to 10^9 Ωcm in the temperature range of 400 to100°C. This can be attributed to the hexagonal structures of Fe_2O_3 and ZnO. Fig. 4.15 shows the lower electrical resistivity variation range of 10^4 to10^8 Ωcm for NiO, which may be because of its cubic structure. However, NiO/ZnO compositions show higher resistivity variation range from 10^6 to 10^9 Ωcm.

4.5 MAGNETIC SUSCEPTIBILITY AND SATURATION
MAGNETIZATION MEASUREMENTS

Magnetic susceptibility of the different paramagnetic compounds was determined by Gouy method at room temperature, using the field strength of 8,000 gauss. Magnetic moments of the compounds were calculated using the expression, μ_{eff} (B.M.) = 2.84 $\sqrt{\chi_M \cdot T}$, where χ_M is the molar susceptibility at room temperature. Magnetic moments were used to calculate the number of unpaired electrons in these compositons. For magnetic compounds, saturation magnetization values were determined using high field hysteresis loop tracer.

The observed gram-susceptibility values at room temperature for the different compositions are presented in tables 4.1 and 4.2. Gram susceptibility values for $Zn_{1-x}Ni_xMnO_3$ system are in the range of 6.10 $x10^{-5}$ to 4.17 $x10^{-5}$ emu/g. It is observed that the susceptibility value gradually decreases with the increase in

x value, up to x = 0.4 and then for x = 0.6 to 0.8 it increases. For $AMnO_3$ (A=Sr, Sm and Nd) system, the susceptibility values are in the range of 0.73 $\times 10^{-5}$ to 5.48 $\times 10^{-5}$ emu/g and are found to be in increasing order from Sr- to Nd-manganites.

The observed higher values of suscesptibility in these manganites are because of Mn^{3+}- Mn^{4+} interaction favouring parallel spins[201]. This can also be explained on the basis of magnetic interaction proposed by Zener[202] called as double exchange interaction. In the interaction configuration:

$$Mn^{3+} — \quad O^{2-} \quad — Mn^{4+},$$
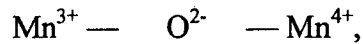
the easy simultaneous transfer of an electron from Mn^{3+} to O^{2-} and from O^{2-} to Mn^{4+} causes the tendency of the traveling electron to retain their spin orientation also a parallel orientation of the magnetic moments of the Mn^{3+} and Mn^{4+} ions. In $Zn_{1-x}Ni_xMnO_3$ system, the decrease in χ_g up to x = 0.4 may be because of the distortion in cubic structure. However, at x = 0.6 and 0.8, Ni ions concentration may result in the formation of ion pairs such as Mn^{3+}- Mn^{4+} along with Ni^{2+} and Ni^{3+}. The B-B interaction becomes stronger with increasing Mn^{3+}- Mn^{4+} ion pairs. This may be responsible for the increased susceptibility at x = 0.6 and 0.8.

In $AMnO_3$ system (A=Sr, Sm and Nd), there is a gradual decrease in structure distortion from Sr- to Nd-manganites. This may be gradually increasing the Mn^{3+}- Mn^{4+} ion pair interactions with the observed increasing order of magnetic susceptibility from Sr- to Nd- manganites.

Table 4.1 Magnetic susceptibility data of different perovskite manganites

Sr. No.	Compound	χ_g (emu/g)	μ_{eff} (B.M.)	No. of unpaired electrons
1	$ZnMnO_3$	6.10×10^{-5}	5.009	4
2	$Zn_{0.8}Ni_{0.2}MnO_3$	4.76×10^{-5}	4.407	4
3	$Zn_{0.6}Ni_{0.4}MnO_3$	4.17×10^{-5}	4.108	3
4	$Zn_{0.4}Ni_{0.6}MnO_3$	5.29×10^{-5}	4.608	4
5	$Zn_{0.2}Ni_{0.8}MnO_3$	5.60×10^{-5}	4.720	4
6	$SrMnO_3$	0.73×10^{-5}	1.855	1
7	$SmMnO_3$	1.86×10^{-5}	3.395	3
8	$NdMnO_3$	5.48×10^{-5}	5.757	5

89

Table 4.2 Magnetic susceptibility data of different supported metal oxides compositions

Sr. No.	Composition	χ_g (emu/g)	μeff (B.M.)
1	5 % Fe_2O_3/ZnO	0.71×10^{-5}	1.216
2	10 % Fe_2O_3/ZnO	1.0×10^{-5}	1.476
3	20 % Fe_2O_3/ZnO	1.2×10^{-5}	1.687
4	Fe_2O_3	1.81×10^{-5}	2.665
5	5 % NiO/ZnO	2.70×10^{-6}	0.731
6	10 % NiO/ZnO	2.90×10^{-6}	0.756
7	20 %NiO/ZnO	3.25×10^{-6}	0.797

Table 4.3 Saturation magnetization data of the magnetic compositions

Sr. No.	Compound	Saturation magnetization (emu/g)
1	NiMnO$_3$	5.593
2	NiO	3.743

NiMnO$_3$ and NiO are observed to be magnetic materials. The saturation magnetization values of these catalysts are presented in table 4.3. For NiMnO$_3$, the observed Tc = 152°C which is in agreement with the reports of Feltz et. al.[193] on ferrimagnetic NiMnO$_3$ and. NiO is antiferromagnetic. The compounds BaCeO$_3$, ZnSnO$_3$ and ZnO are found to be diamagnetic.

In Fe$_2$O$_3$/ZnO system, Fe$_2$O$_3$ is observed to be paramagnetic. This is in agreement with the reports of Creer et. al.[203]. With the gradual increase in concentration of Fe$_2$O$_3$ on the support i.e. ZnO, magnetic susceptibility is found to increase from 0.7 x 10^{-5} to 1.8 x 10^{-5} emu/g. In NiO/ZnO system, with the increase in the concentration of NiO on the support, χ_g value of the compositions increases from 2.7 x 10^{-6} to 3.25 x 10^{-6} emu/g.

4.6 ESR STUDIES

ESR studies carried out on various samples gave the insight of the catalytically active and paramagnetic species. The technique was used as a qualitative tool to analyze the changes occurring with the A site substitution in these perovskites. ESR data of different perovskites recorded at room temperature is presented in table 4.4. ESR spectra of some of the samples are shown in figures 4.16 - 4.18. The line-width of ESR spectra depends on the relaxation time of the spin state through either one or both the processes (a) spin-lattice relaxation and (b) spin –spin relaxation. The interaction of the paramagnetic ions with the thermal vibrations of the lattice leads to a short spin-lattice relaxation time.

Scan Range : 4000 G   Modulation Frequency : 100 KHz   Microwave Power   : 5.0 mW
Field Set   : 3000 G   Modulation Amplitude : 1.0 G   Microwave Frequency: 9.1 GHz
Temperature: R.T.   Marker   : TCNE

a)

b)

c)

−5   −4   −3   −2   −1   0   +1   +2   +3   +4   +5
1000   2200   3000   3800   5000
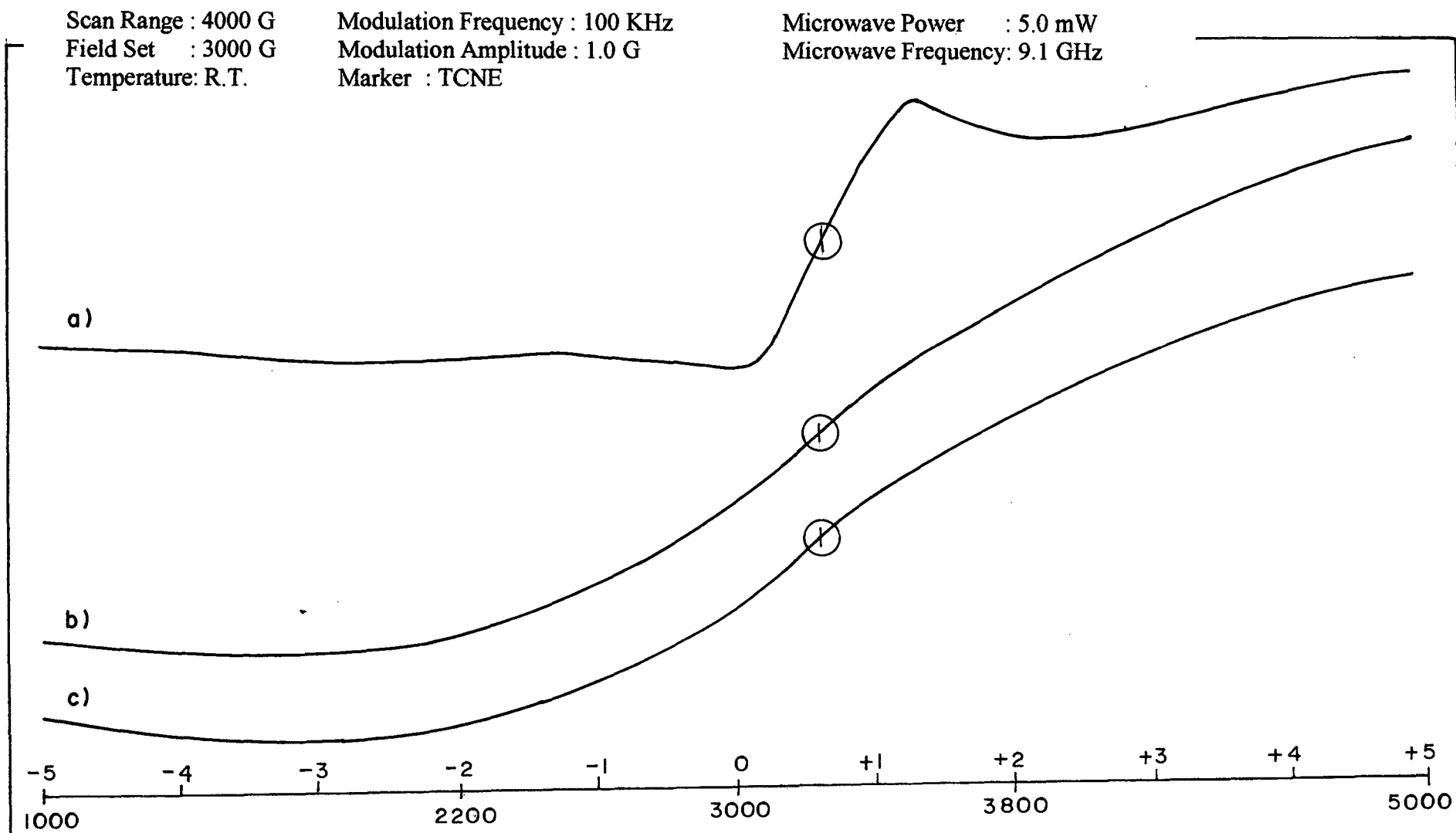
Fig. 4.16 ESR spectra of a) $ZnMnO_3$ b) $Zn_{0.8}Ni_{0.2}MnO_3$ and c) $Zn_{0.6}Ni_{0.4}MnO_3$

93

Scan Range : 4000 G   Modulation Frequency : 100 KHz   Microwave Power   : 5.0 mW
Field Set   : 3000 G   Modulation Amplitude : 1.0 G   Microwave Frequency: 9.1 GHz
Temperature: R.T.   Marker : TCNE

a)

b)

-5   -4   -3   -2   -1   0   +1   +2   +3   +4   +5
1000   2200   3000   3800   5000
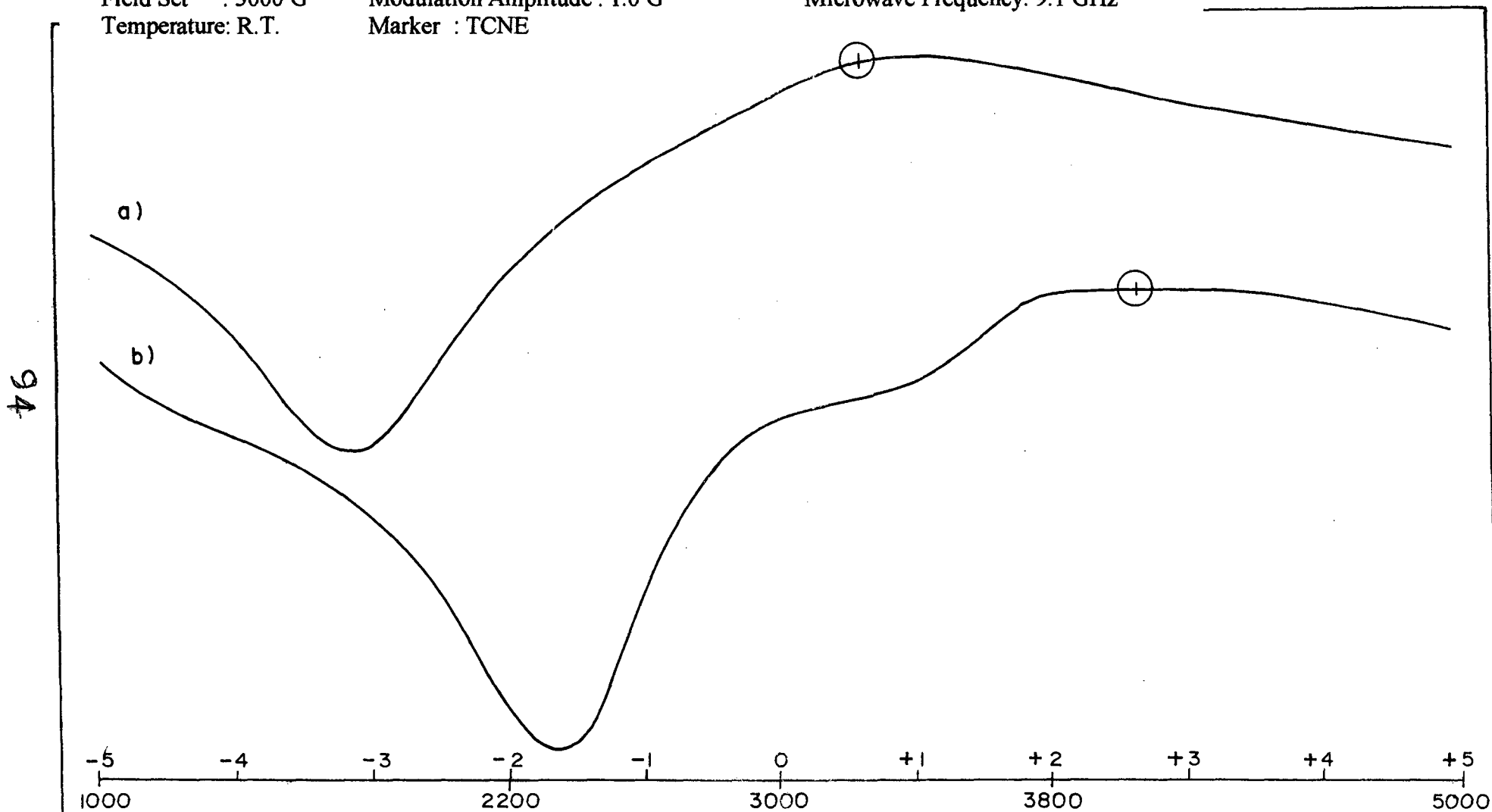
Fig. 4.17   ESR   spectra   of   a) $Zn_{0.4}Ni_{0.6}MnO_3$ and   b) $Zn_{0.2}Ni_{0.8}MnO_3$

94

Fig. 4.18   ESR   spectra   of   a) $SrMnO_3$ b) $SmMnO_3$ and   c) $NdMnO_3$

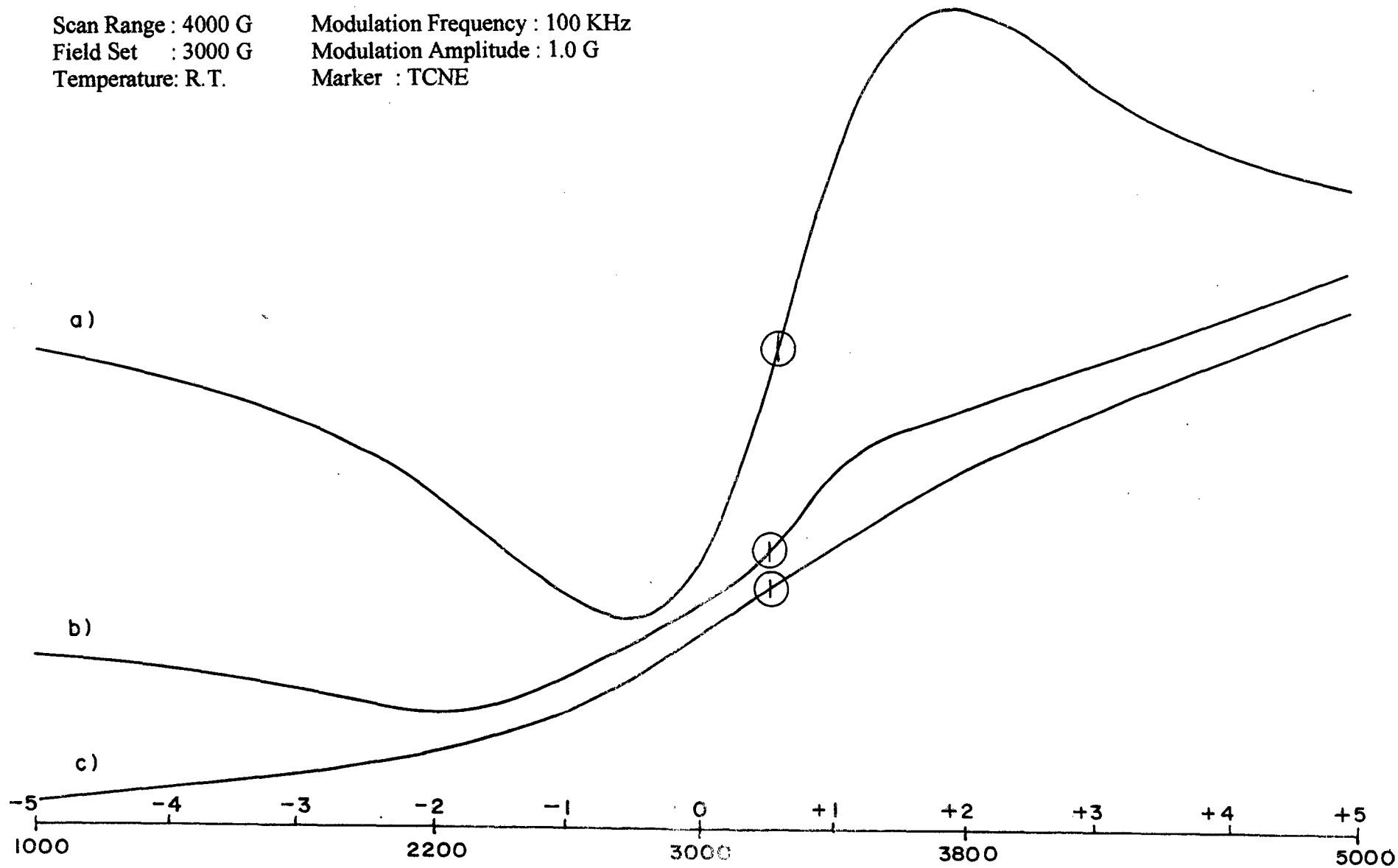In fig. 4.16, the ESR spectrum of $ZnMnO_3$ shows a peak with smaller line-width. With the substitution of Zn by Ni (x = 0.2 and 0.4) in the compositions, the line- widths are observed to be broadened. Thus, for $ZnMnO_3$ at room temperature spin-lattice relaxation time is sufficient to give sharp peak with shorter line-width.

With the substitution by Ni (x = 0.2 and 0.4) increase in the thermal vibrations of the lattice decreases the spin-lattice relaxation time which must be increasing the line-widths of the peaks of these compositions. The g-value is around 2 for the compositions (x = 0.0, 0.2 and 0.4). This may be because of the magnetic moment of the manganites ions with negligible contribution from Ni ions.

Fig. 4.17 shows that the further increase in Ni concentrations, (x = 0.6 and 0.8) reduces the line-widths and increases g-value. Thus, these higher concentrations of Ni must also be contributing towards the magnetic moment of the compositions.

For heavier ions like Sm^{3+} and Nd^{3+} the spin-orbit coupling is strongly coupled to lattice vibrations, reducing the spin relaxation time. Fig. 4.18 shows ESR spectra for $AMnO_3$ (A=Sr, Sm and Nd) system recorded at room temperature.

It is observed that ESR spectrum of $SrMnO_3$ shows comparatively sharper peak with the line-width of around 940 gauss. For the manganites of Sm and Nd the line-widths are broader. For the heavier ions Sm^{3+} and Nd^{3+} the spin-orbit coupling is strongly coupled to the lattice vibrations, reducing the spin relaxation time. This broadens the peaks of the manganites.

From the overall study of ESR spectroscopy, it can be inferred that manganites are ESR active.

Table 4.4 ESR data of different perovskite samples

| Sr.No.	Compound	g-value	Line Width (gauss)
1	$ZnMnO_3$	1.99	530
2	$Zn_{0.8}Ni_{0.2}MnO_3$	1.99	2500
3	$Zn_{0.6}Ni_{0.4}MnO_3$	2.02	2200
4	$Zn_{0.4}Ni_{0.6}MnO_3$	2.57	1640
5	$Zn_{0.2}Ni_{0.8}MnO_3$	2.50	960
6	$SrMnO_3$	1.98	940
7	$SmMnO_3$	2.09	1400
8	$NdMnO_3$	2.11	2080

The lower concentrations of Ni at A site do not contribute towards ESR signal. However, higher concentrations of Ni at A site enhance the ESR signal of the manganites. Heavy rare earth ions at A site in the perovskites broaden the ESR line-widths.

4.7 DIFFUSE REFLECTANCE SPECTROSCOPY (DRS)

This technique is based on the reflection of light in the ultraviolet (10-420 nm), visible (420-700 nm) and near-infrared (700-2500 nm) regions by a powder sample[204]. In a diffuse reflectance spectrum (DRS), the ratio of the lights scattered from thick layer of the sample and an ideal non-absorbing reference sample is measured as a function of the wavelength λ. DRS spectra for all the prepared samples are run between the wavelengths of 300-700 nm. Figures 4.19 and 4.20 show DRS spectra of representative samples. With the help of λ_{max} (nm) from the spectrum, band gap energy [B.G.E. (eV)] of the sample is calculated using the relation:

$$B.G.E. = \frac{1.24 \times 10^3}{\lambda_{max}}$$

Tables 4.5 and 4.6 present band gap energy data of different samples. Band gap energy for the $Zn_{1-x}Ni_xMnO_3$ and $AMnO_3$ (A = Sr, Sm and Nd) series compositions are found to be in the range of 1.72 to 2.12 eV. Band gap energy for $BaCeO_3$ and $ZnSnO_3$ are 3.10 and 3.56 eV respectively. Thus, all the manganites compositions show lower band gap energy.

Fig. 4.19 DRS spectrum of $Zn_{0.6}Ni_{0.4}MnO_3$

Fig. 4.20   DRS   spectrum   of   BaCeO$_3$

100
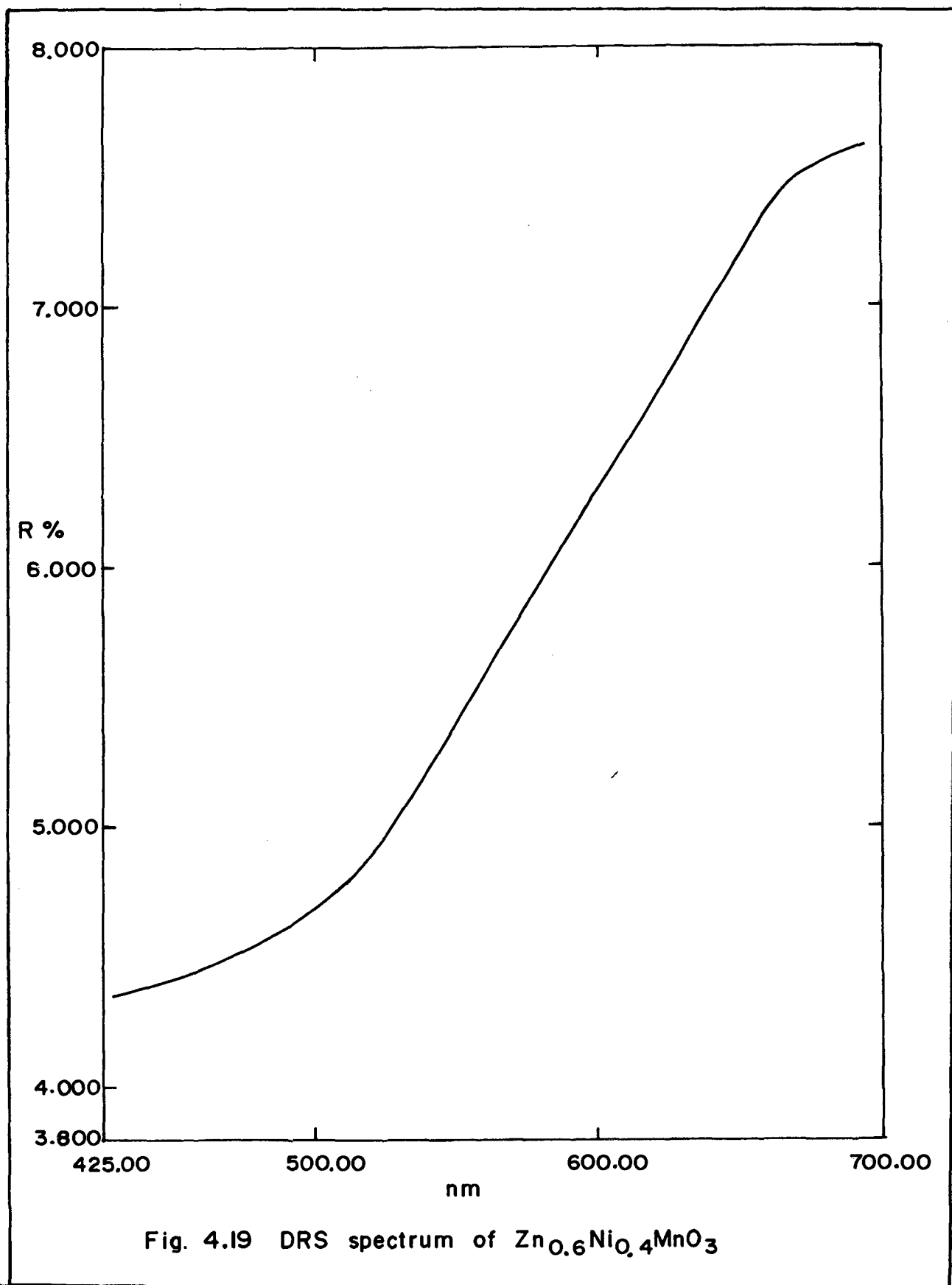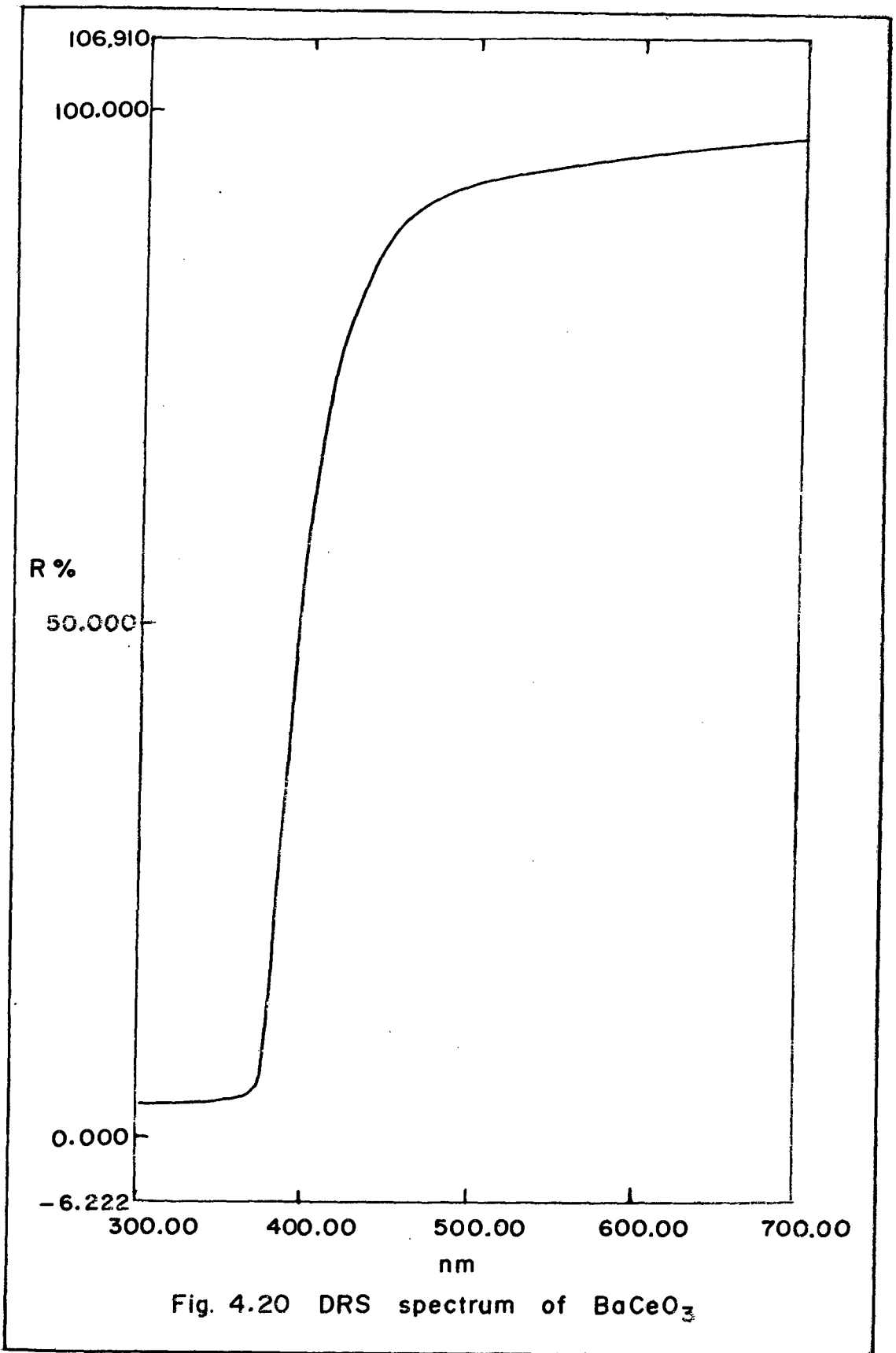
Table 4.5 DRS (Band gap energy) data of Samples

Sr. No.	Compound	λ max (nm)	Band gap energy (ev)
1	$ZnMnO_3$	589	2.11
2	$Zn_{0.8}Ni_{0.2}MnO_3$	584	2.12
3	$Zn_{0.6}Ni_{0.4}MnO_3$	584	2.12
4	$Zn_{0.4}Ni_{0.6}MnO_3$	595	2.08
5	$Zn_{0.2}Ni_{0.8}MnO_3$	602	2.06
6	$NiMnO_3$	588	2.11
7	$SrMnO_3$	719	1.72
8	$SmMnO_3$	679	1.82
9	$NdMnO_3$	697	1.78

Table 4.6 DRS (Band gap energy) data of different Samples

Sr. No.	Catalyst	λ max (nm)	Band gap energy (ev)
1	$BaCeO_3$	400	3.10
2	$ZnSnO_3$	348	3.56
3	ZnO	389	3.18
4	Fe_2O_3	582	2.13
5	NiO	357	3.47

CHAPTER 5

CATALYTIC OXIDATION

OF

CARBON MONOXIDE

CATALYTIC OXIDATION OF CARBON MONOXIDE

The transition metal oxidic perovskites provide an excellent base for correlating catalytic and solid state properties, because they can be well characterized by different techniques. In this chapter the catalytic activity of series of perovskites and supported metal oxides is being discussed with respect to CO oxidation, separately for the series-I ($Zn_{1-x} Ni_x MnO_3$), series-II ($SrMnO_3$, $SmMnO_3$, $NdMnO_3$, $BaCeO_3$ and $ZnSnO_3$), series-III (Fe_2O_3/ZnO) and series-IV (NiO/ZnO). Though CO oxidation reaction is extensively studied over noble metal oxides and other oxide catalysts, it is not well studied over the above compounds. This reaction is important from the point of automobile and industrial exhaust pollution control.

5.1 SURFACE AREA

Surface areas of the samples were measured by BET nitrogen adsorption method at the boiling liquid nitrogen temperature employing SMARTSORB-92/93 model surface area analyzer. The results are summarized in the tables 5.1 - 5.3. The perovskites prepared by co-precipitation precursor technique possessed the surface areas as low as 5.10 m^2/g and as high as 20.91 m^2/g. The catalysts prepared by combustion method have comparatively lower surface areas in the range 2.50 to 5.40 m^2/g.

Table 5.1 Specific surface areas of the series-I perovskite catalysts

Sr. No	Catalyst	BET Surface area (m^2/g)
1	$ZnMnO_3$	5.10
2	$Zn_{0.8}Ni_{0.2}MnO_3$	17.74
3	$Zn_{0.6}Ni_{0.4}MnO_3$	14.28
4	$Zn_{0.4}Ni_{0.6}MnO_3$	3.45
5	$Zn_{0.2}Ni_{0.8}MnO_3$	5.75
6	$NiMnO_3$	20.91

Table 5.2 Specific surface areas of the series-II perovskite catalysts

Sr. No	Catalyst	BET Surface area (m^2/g)
1	$SrMnO_3$	4.00
2	$SmMnO_3$	5.00
3	$NdMnO_3$	5.40
4	$BaCeO_3$	2.50
5	$ZnSnO_3$	2.60

Table 5.3 Specific surface areas of the supported metal oxide catalysts

Sr. No.	Catalyst	BET Surface area (m^2/g)
1	ZnO	2.13
2	5 % Fe_2O_3/ZnO	3.85
3	10 % Fe_2O_3/ZnO	3.88
4	20 % Fe_2O_3/ZnO	6.10
5	Fe_2O_3	14.16
6	5 % NiO/ZnO	3.61
7	10 % NiO/ZnO	5.31
8	20 % NiO/ZnO	5.00
9	NiO	10.00

Supported metal oxide compositions have the surface areas in the range 2.13 to14.16 m^2/g.

The low surface area of some of the compositions may be due to higher temperature of sintering and variance of sintering time to get monophasic compounds. The nitrogen adsorption is not a satisfactory method for absolute measurement of low surface area and as such the variation seen among the different compositions are with in the experimental errors.

5.2 SCANNING ELECTRON MICROSCOPY

SEM micrographs of powdered materials of some samples were taken on JEOL make microscope. Figure 5.1 shows the micrographs of the representative samples prepared by co-precipitation and combustion methods.

The morphology analysis of the micrographs reveal that the particles of the catalyst prepared by wet co-precipitation technique show low tendency towards agglomeration than the particles of the catalysts prepared by combustion method.

With the help of the SEM micrographs, the average particle size of the catalysts is calculated. The average particle size of the catalysts prepared by co-precipitation technique is in the range 80 to 100 nm where as that is of the catalysts prepared by combustion method lies in the range 110 to 130 nm.
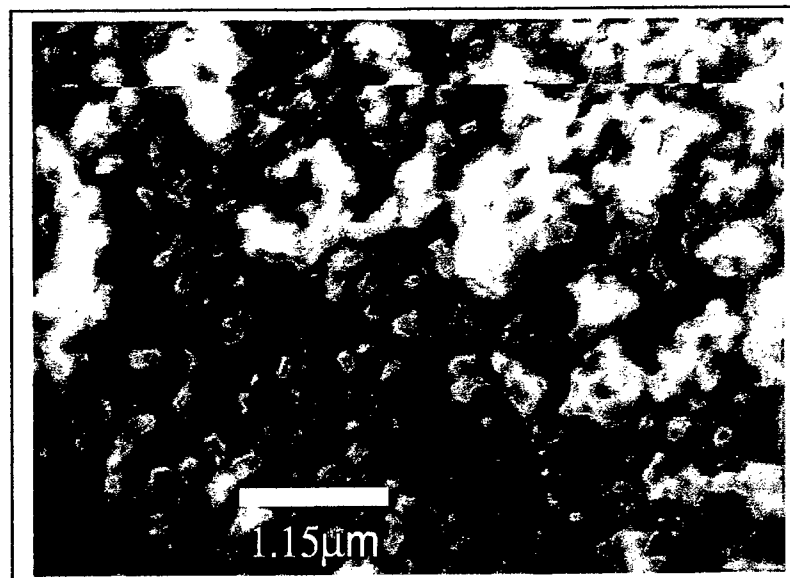
Fig.5.1 (a) SEM micrograph of NiMnO$_3$ (prepared by co-precipitation method)
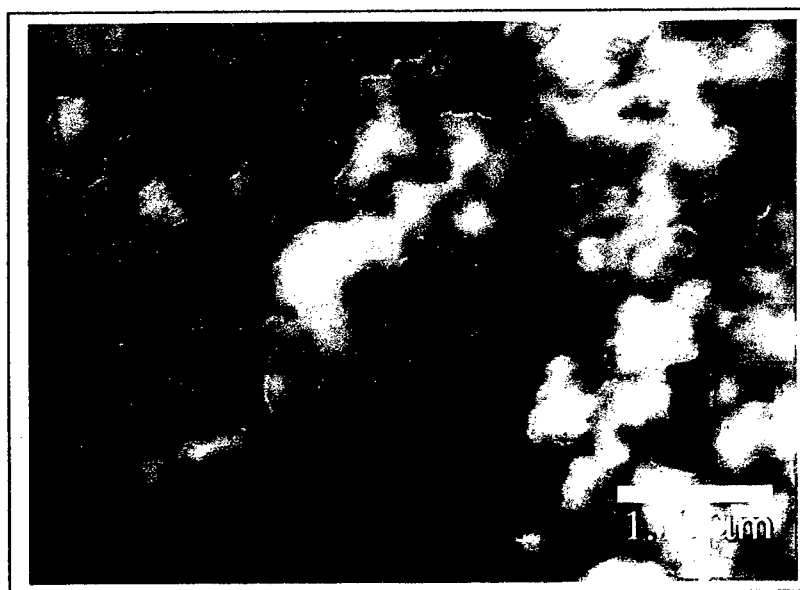
Fig. 5.1 (b) SEM micrograph of SmMnO$_3$ (prepared by combustion method)

5.3 CATALYTIC CO OXIDATION REACTION

All the prepared samples were tested for their catalytic CO oxidation efficiency with respect to temperature variation from room temperature to 400 °C.

5.3.1 Series-I ($Zn_{1-x}Ni_xMnO_3$)

The temperature dependent CO conversion studies over different compositions of $Zn_{1-x}Ni_xMnO_3$ (x = 0.0, 0.2, 0.4, 0.6, 0.8 and 1.0) is shown in fig. 5.2. The rate of CO oxidation is observed to increase with the substitution of Zn by Ni at the A site of $ZnMnO_3$. For x = 0.2 and 0.4 the increase in CO oxidation rates are much higher and close to each other as compared to those for x = 0.6 and 0.8. In the series, CO oxidation rate is the highest for $NiMnO_3$ composition. The surface areas of these compositions may not be the only criteria for the catalytic activity in this series. For arriving at any correlation between catalytic behaviour and other properties, kinetic parameters of CO oxidation were analyzed. CO oxidation rate at a fixed temperature of 240 °C was calculated.

The flow rate used during the catalytic reaction studies was 5 l/h, with 5% CO, 5% O_2 and 90% N_2. The kinetic parameter data is given in table 5.4. The rate of CO molecules oxidation with the inclusion of Ni at A site of the perovskite compositions is found to be increased largely for x = 0.2 and 0.4. For the compositions with x = 0.6 and 0.8 the increase in oxidation rate reduces.
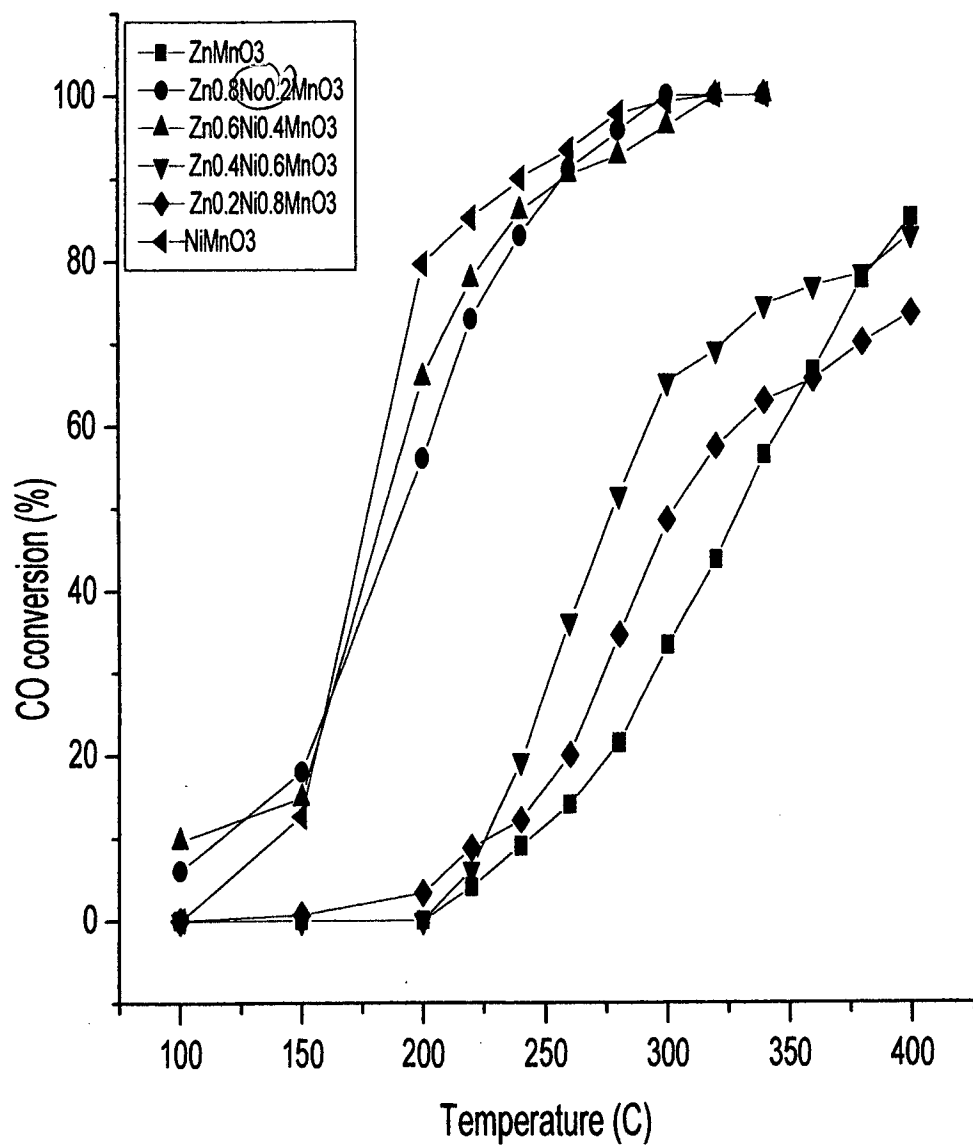
Fig. 5.2 CO conversion as a function of catalyst temperature for series-I catalysts.

Table 5.4 Kinetic parameters of CO oxidation over series-I catalysts

Sr. No.	Catalyst	S.A. (m^2/g)	CO (% con.) (at 240°C)	Rate (molecul./m^2.s) (at 240°C)
1	ZnMnO$_3$	5.10	9.00	3.29 x 10^{16}
2	Zn$_{0.8}$Ni$_{0.2}$MnO$_3$	17.74	83.00	8.73 x 10^{16}
3	Zn$_{0.6}$Ni$_{0.4}$MnO$_3$	14.28	85.00	11.23 x 10^{16}
4	Zn$_{0.4}$Ni$_{0.6}$MnO$_3$	3.45	19.23	10.40 x 10^{16}
5	Zn$_{0.2}$Ni$_{0.8}$MnO$_3$	5.75	12.09	3.92 x 10^{16}
6	NiMnO$_3$	20.91	90.00	8.03 x 10^{16}

Several Authors[15,162,205,206] have reported that in ABO_3 perovskites, the A ions in general are catalytically inactive and the active transition metal ions at the B position are placed at relatively large distances from each other that a gas molecule interacts only with a single site. Hence these are excellent catalytic models for the study of the interaction of CO and O_2 on single surface site. Voorhoeve et.al.[207] have reported that the catalytic activity for the oxidation of CO is closely related with the electronic structure of the surface oxide ions and the electronic properties of perovskite type oxides are mainly determined by the electronic configuration of transition metal ions. Viswanathan[208] mentioned that the catalytic CO oxidation activity is directly or indirectly related to the electronic configuration of B-site ion and B-O bond strength. Shimizu[178] suggested the increase in tolerance factor with the increasing radius of the rare earth ion in the A site or decreasing radius of transition metal ion in the B site. This increase in tolerance factor will lower the interaction of B-O-B bond and promote the formation of oxygen vacancies at the surface. Thus the decrease in B-O B bond interaction increases the activity of CO oxidation. These correlations can be considered to imply that the active sites involved in the oxidation of CO consist of B-O-B clusters which are in agreement with the conclusion reported by Tascon and Tejuca[209-211]. Voorhoeve et. al.[163] in their study of CO oxidation over perovskite-type oxides of the 3d transition metals suggested that over these catalysts, this reaction is an example of suprafacial catalysis, in which the efficiency of the catalyst is determined by the symmetry and energy of the orbitals near the Fermi level. According to Wolfram et.al.[212] the CO oxidation activity increases when the

Fermi level move towards the centre of the lowest e^*_g level at the surface that is the dz^2 anti bonding level. This suggests that the dz^2 level has the right energy and symmetry for the rate determining step in the CO oxidation. Fierro[162] has reported that the maximum CO oxidation activity is attained in both the cases for an occupation of e_g levels of less than one electron and the t_{2g} levels being half-filled or totally filled. Baiker et. al.[51] studied the effect of A - site ion size in $LnCoO_3$ perovskites for oxidation reaction and interpreted that for the smaller A - site ion, the catalytic activity is comparatively higher. Seiyama[213] has said that the most active perovskite catalysts are those which contain Co and Mn at the B - site. According to Voorhoeve[13], the catalytic studies on manganites appear to offer a fruitful field since their electrical and magnetic properties may be varied with in the same structure by compositional variations.

The observed CO oxidation catalytic activity of the series-I catalysts can be explained on the basis of Goldschmidt's tolerance factor, Mn-O-Mn bond interaction, Mn-O binding energy, Mn - ion configuration and Mn^{4+}- Mn^{3+} ion pairs redox potential. Zn ion in the compositions is catalytically inactive. Mn ion is smaller than Zn ion. Thus the tolerance factor value of the perovskite $ZnMnO_3$ accounts for its cubic symmetry. In this symmetry Mn-O-Mn interactions are weak and Mn-O binding energy is low. This promotes the formation of oxygen vacancies at the catalyst surface. The lower binding energy for the surface oxygen species is favourable for $ZnMnO_3$ compound to be more active for CO oxidation. Mn^{4+} ion at the B site of the perovskite has the configuration of $t^3_{2g} e_g^0$. Thus e_g level has less

than one electron and t_{2g} level is half filled. In this configuration Fermi level moves towards the centre of the lowest e^*_g level at the surface. This is also responsible for increasing the CO oxidation activity. In the series-I, $ZnMnO_3$ shows good CO conversion efficiency of about 85% at 400°C. With the substitution of Zn by Ni initially at x = 0.2 and 0.4 there is no much change in the cubic symmetry of the perovskites and binding energy for surface oxygen is almost same. The small amounts of Nickle acts as a p type dope in $ZnMnO_3$ by the formation of Mn^{4+} and Ni^{2+} ions. Therefore at these x values, Ni substituted in $ZnMnO_3$ gives rise to more Mn^{4+}- Mn^{3+} ion pairs, favouring more CO adsorption and increased catalytic activity than $ZnMnO_3$. This is in agreement with the reports of Salker et.al.[175]. Thus at x = 0.2 and 0.4 the CO conversion is close to 100% at 300-320°C. With further increase in Ni, at x = 0.6 and 0.8 there is distortion in the cubic structure which increases the binding energy for surface oxygen. This lessens the catalytic activity effect. Thus at x = 0.6 and 0.8 the increase in CO oxidation activity declines. As reported by Mehandjiev et.al.[214] both Ni^{2+} and Mn^{4+} are in octahedral positions. The concentration of Mn^{4+}- Mn^{3+} ion pairs is very large and as a result high activity of $NiMnO_3$ composition is observed. Thus for $NiMnO_3$, CO conversion is as high as 100% at about 300°C. The analysis of kinetic parameters of CO oxidation over this series of compositions at 240°C show similar trend of variation in catalytic CO oxidation efficiency of the catalysts.

As reported earlier these catalysts are found to have low band gap energy of about 2.1 eV and are good semiconductors. The higher CO oxidation catalytic

activity of these compositions can be attributed to their low band gap energy and semiconducting nature which is in agreement with the reports of Haralambous et. al.[215].

### 5.3.2 Series-II (SrMnO₃, SmMnO₃, NdMnO₃, BaCeO₃ and ZnSnO₃)

The temperature dependent catalytic CO oxidation studies of this series compositions shown by fig.5.3 reveals that the $AMnO_3$ (A = Sr, Sm and Nd) compositions have good catalytic activity. This may be because of the low binding energy of Mn ion for the surface oxygen. Mn^{4+} ion configuration in these manganites with half filled t_{2g} orbitals and empty dz^2 orbitals shifts Fermi level towards the centre of the antibonding e_g orbital at the surface. This promotes CO chemisorption at the surface leading to CO oxidation.

According to Kuroda et. al.[216], alkaline earth metal-manganese oxides are oxygen deficient which significantly affects their crystal structure. Hexagonal stacking of the AO_3 layers in ABO_3 compounds leads to face shared BO_6 octahedra and thus to the possibility of short metal-metal distances and metal-metal bonding. Chamberland et. al.[191] have reported the possibility of short metal-metal bonding in $SrMnO_3$. This must be reducing the number of active sites at the surface of $SrMnO_3$ available for gas molecules. $SrMnO_3$ is found to show comparatively lower catalytic activity, which may be because of its hexagonal structure. $SmMnO_3$ and $NdMnO_3$ have higher catalytic activity because of their orthorhombic structures. Slightly smaller ionic radius of Sm decreases the tolerance factor in $SmMnO_3$. This distorts

its orthorhombic structure slightly and increases the binding energy for surface oxygen. Hence at low temperature of 150 to 260°C, $SmMnO_3$ has slightly smaller activity than $NdMnO_3$. However, at higher temperatures of above 260°C, $SmMnO_3$ and $NdMnO_3$ show almost same activity.

In this series $BaCeO_3$ and $ZnSnO_3$ show low catalytic activity. $ZnSnO_3$ show slightly better catalytic activity than $BaCeO_3$. Both these compounds have orthorhombic structure. Therefore symmetry does not appear to be the criteria for the activity. The low activity of these catalysts can be explained on the basis of metal-oxygen (M-O) bond energy for B site cation and molar free energy of reduction ($\Delta G°$) for the oxides which occupy B site. Varadarajan et. al.[217] have reported bond energy and free energy of reduction as 293.2 and 225.0 KJ/mol respectively for Ce-O bond of $BaCeO_3$. These high values depict the low reducibility of Ce^{4+} ion in $BaCeO_3$. The low reducibility of Ce^{4+} can also be visualized from its stable configuration of $4d^{10}5s^25p^6$. Similarly in $ZnSnO_3$ the reducibility of Sn^{4+} is low because of its stable configuration of $4d^{10}$. Thus in these compositions Ce^{4+}- Ce^{3+} and Sn^{4+}- Sn^{2+} ion pair associations are low and these set low redox potentials at the surface. Hence catalytic activities of these compositions are low. Slightly higher activity of $ZnSnO_3$ may be attributed to its higher surface area.

The analysis of kinetic parameters of CO oxidation over the catalysts of this series at 300°C show that $AMnO_3$ (A = Sr, Sm and Nd) compositions have higher rate of CO conversion than $BaCeO_3$ and $ZnSnO_3$. The kinetic parameter data is shown in table 5.5.
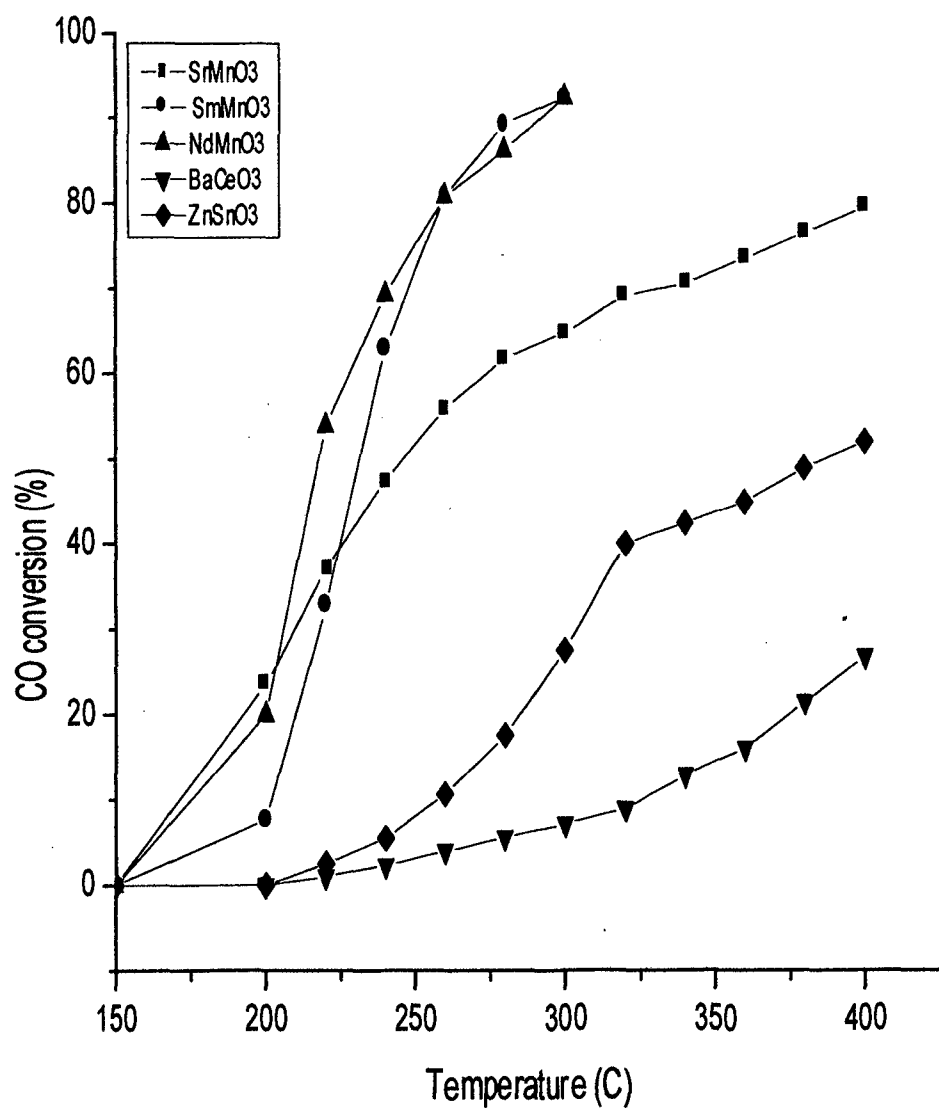
Fig. 5.3 CO conversion as a function of catalyst temperature for Series-II catalysts

Table 5.5 Kinetic parameters of CO oxidation over series-II catalysts

Sr. No.	Catalyst	S.A. (m^2/g)	CO (% con.) (at 300°C)	Rate (molec./m^2.s) (at 300°C)
1	SrMnO$_3$	4.00	64.70	3.01x10^{17}
2	SmMnO$_3$	5.00	92.31	3.43x10^{17}
3	NdMnO$_3$	5.40	92.30	3.18x10^{17}
4	BaCeO$_3$	2.20	7.14	0.60x10^{17}
5	ZnSnO$_3$	2.60	27.50	1.96x10^{17}

The catalytic activity of these catalysts can be correlated with their electrical resistivity. As reported earlier $AMnO_3$ compositions show higher electrical conductivity because of larger Mn^{4+}- Mn^{3+} ion pair concentration. The larger number of Mn^{4+} ions attributes to their higher catalytic activity. The reported lower electrical resistivity of $BaCeO_3$ and $ZnSnO_3$ is due to lower number of Ce^{4+}- Ce^{3+} and Sn^{4+}- Sn^{2+} ion pairs. The smaller number of these ion pairs explains the low catalytic activity shown by them. The magnetic properties of these compounds can also be correlated to their observed catalytic activities. χ_g values of $AMnO_3$ compositions are in the increasing order of $SrMnO_3 < SmMnO_3 < NdMnO_3$. The catalytic activities of the compositions are also observed to increase in the same order. The compounds $BaCeO_3$ and $ZnSnO_3$ having low catalytic activity are found to be diamagnetic. It is observed in this series that with the increase in surface area of the compositions, the catalytic activity is increased. The band gap energy of $AMnO_3$ (A = Sr, Sm, and Nd) compositions having higher catalytic activity are found to be about 1.75 eV, where as that is for $BaCeO_3$ and $ZnSnO_3$ compounds with low catalytic activity is higher at around 3.25 eV.

5.3.3 Series-III (Fe_2O_3/ZnO)

Fig. 5.4 shows the temperature dependent catalytic CO oxidation studies of series-III (Fe_2O_3 = 0%, 5%, 10%, 20% and 100%) compositions. The substrate ZnO has poor CO oxidation catalytic activity.

It is as low as 3.5% at almost all the temperatures of study. With the gradual inclusion of Fe_2O_3 on this support, the catalytic activity gradually increases. At 400°C, the compositions with 10 and 20% Fe_2O_3 show the activity of 44 and 50% respectively. The non-supported Fe_2O_3 at this temperature shows the activity of about 75%. Both ZnO and Fe_2O_3 have hexagonal structure. Thus the difference in their catalytic activity can not be explained on the basis of structure. The poor catalytic activity of ZnO can be explained on the basis of its low surface area of 2.13 m^2/g and low reducibility of Zn^{2+} ion because of its stable configuration of $3d^{10}$. The poor catalytic activity of ZnO may also be due to its diamagnetic behaviour. Fe^{3+} in Fe_2O_3 with $3d^5$ configuration is capable of getting reduced to Fe^{2+} which sets the Fe^{3+}- Fe^{2+} redox potential at the catalyst surface. Fe_2O_3 also has the higher surface area of 14.16 m^2/g. Ion pair redox potential and the higher surface area must be responsible for the higher catalytic activity shown by Fe_2O_3. The electrical resistivity of Fe_2O_3 in this series can be well correlated with its observed CO catalytic activity. As reported earlier, electrical resistivity of Fe_2O_3 up to 200°C is high to the order of 10^9 Ωcm. The observed catalytic activity for this compound at above temperatures is zero. With the further increase in temperature, resistivity drops to the order of about 10^8 Ωcm at 250°C and finally to the order of 10^6 Ωcm. at 400°C. The increased electrical conductivity corresponds to the increased catalytic activity. Thus the increase in redox potential of Fe^{3+}- Fe^{2+} ion pairs begins at above 200°C
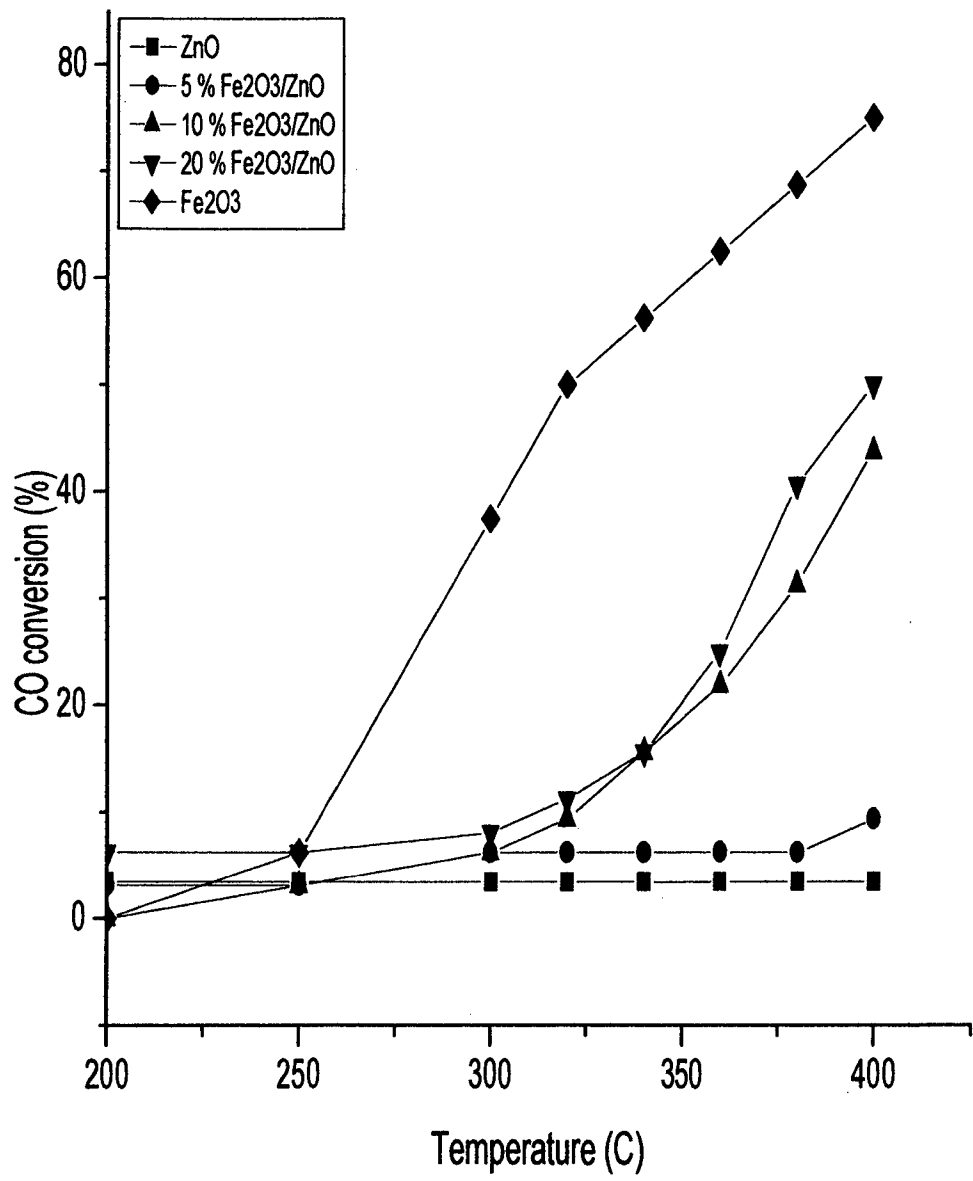
Fig. 5.4 CO conversion as a function of catalyst temperature for Series-III catalysts

Table 5.6 Kinetic parameters of CO oxidation over series-III catalysts

Sr. No.	Catalyst	S.A. (m^2/g)	CO (%conversion) (at 400°C)	Rate (molec./m^2.s) (at 400°C)
1	ZnO	2.13	3.5	3.01×10^{16}
2	5% Fe$_2$O$_3$/ZnO	3.85	9.4	4.53×10^{16}
3	10% Fe$_2$O$_3$/ZnO	3.88	44	20.9×10^{16}
4	20% Fe$_2$O$_3$/ZnO	6.10	50.0	15.2×10^{16}
5	Fe$_2$O$_3$	14.16	75.0	9.8×10^{16}

The kinetic parameters analysis of CO oxidation over the series of catalysts at 400°C also reveals that the rate of CO oxidation over ZnO is low as compared to that over Fe_2O_3/ZnO compositions. The data of kinetic parameters for the series is given in table 5.6.

5.3.4 Series-IV (NiO/ZnO)

The temperature dependent catalytic CO oxidation studies of series-IV (NiO = 0%, 5%, 10%, 20% and 100%) compositions show that the ZnO has a very poor CO oxidation catalytic activity as mentioned earlier. At all the temperatures from 150 to 400°C the activity is low. This low catalytic activity is explained on the basis of its low surface area, low reducibility of Zn^{2+} ion and diamagnetic behaviour. NiO shows catalytic activity of 78% at 400°C. The higher surface area and the higher redox potential of Ni^{3+}- Ni^{2+} ion pairs of this compound attribute to its higher activity. The catalytic activity of NiO at different temperatures can be correlated to its electrical conductivity at these temperatures. At the lower temperature of 50°C the electrical resistivity of NiO is to the order of 10^8 Ωcm. This reflects its low activity at this temperature. With the increasing temperature, resistivity decreases and activity increases. Thus, at 400°C the resistivity is to the order of 10^4 Ωcm and the catalytic CO conversion is 78%.

This reveals that with increase in temperature, Ni^{3+}- Ni^{2+} ion pairs concentration increases which is responsible for its higher electrical conductivity and the higher catalytic activity.
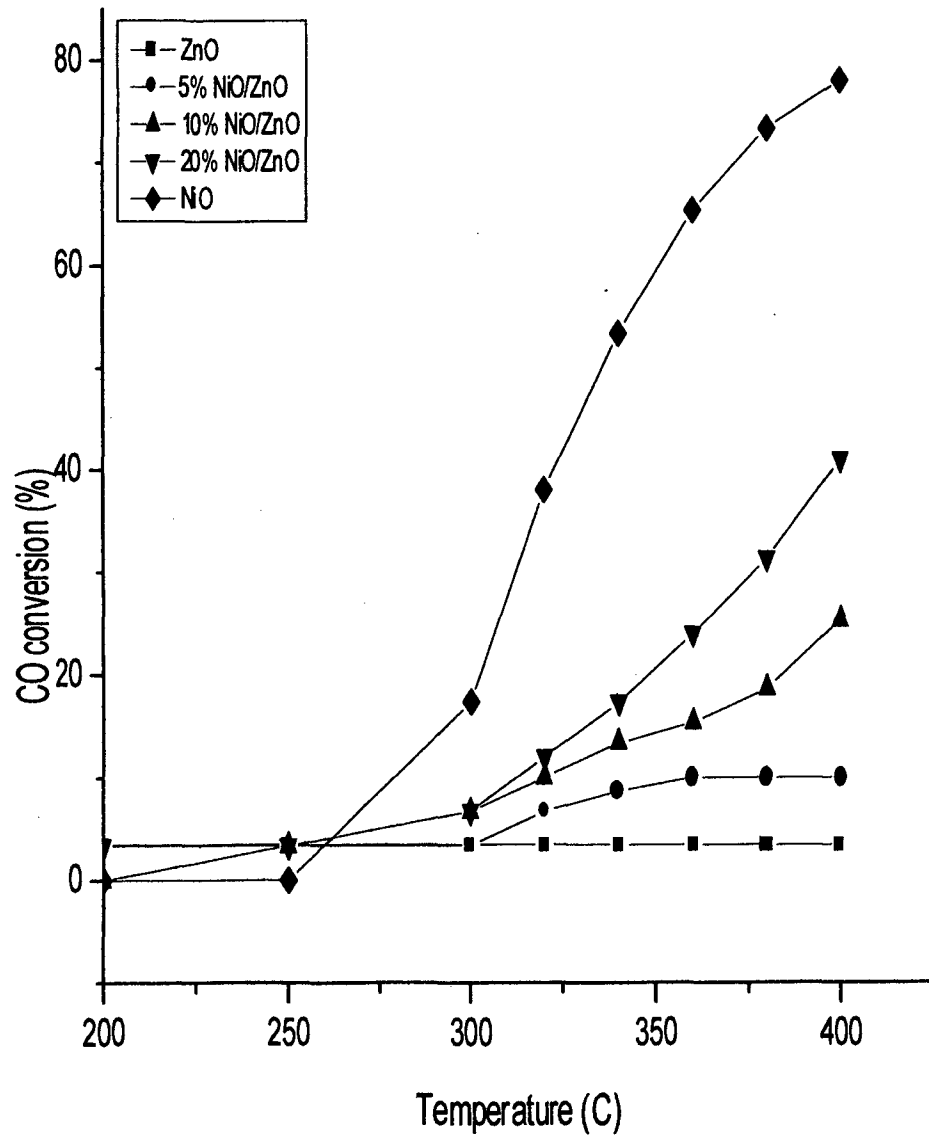
Fig. 5.5 CO conversion as a function of catalyst temperature
for series IV catalysts

Table 5.7 Kinetic parameters of CO oxidation over series-IV catalysts

Sr. No.	Catalyst	S.A. (m^2/g)	CO (% con.) (at 400°C)	Rate (molec./m^2.s) (at 400°C)
1	ZnO	2.13	3.5	3.01×10^{16}
2	5% NiO/ZnO	3.61	10.0	5.15×10^{16}
3	10% NiO/ZnO	5.31	25.3	8.87×10^{16}
4	20% NiO/ZnO	5.00	41.0	15.25×10^{16}
5	NiO	10.00	78.0	14.51×10^{16}
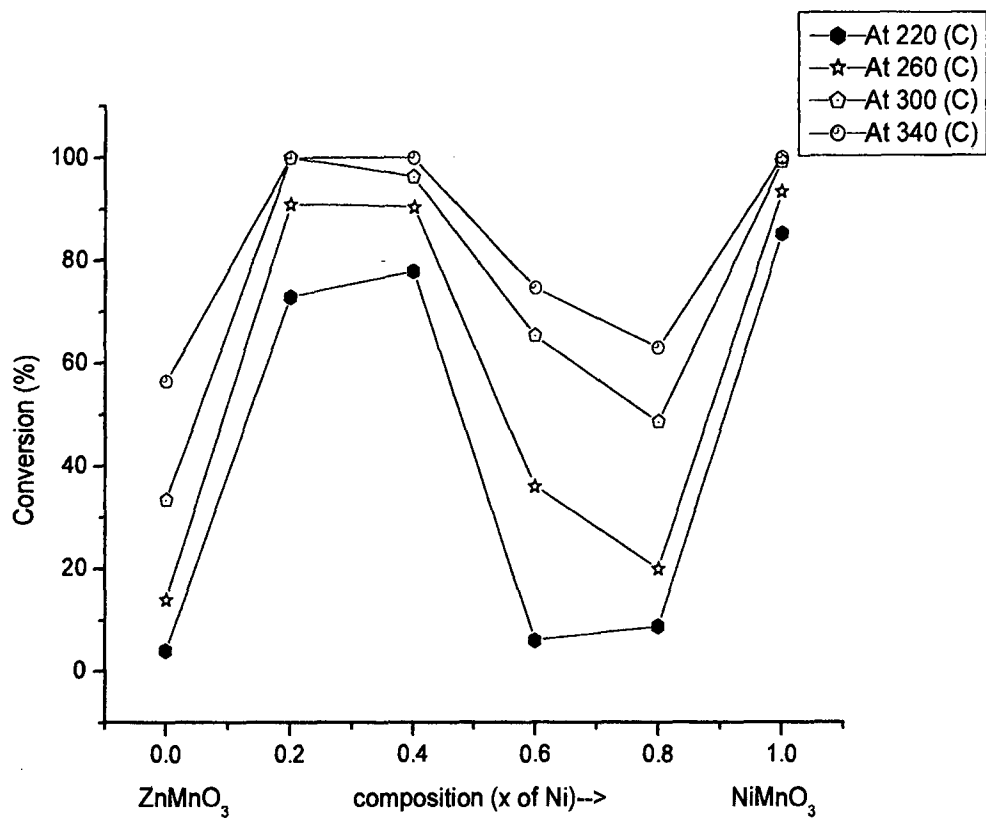
Fig. 5.6 CO Conversion as a function of catalyst
composition for the system $Zn_{1-x}Ni_xMnO3$
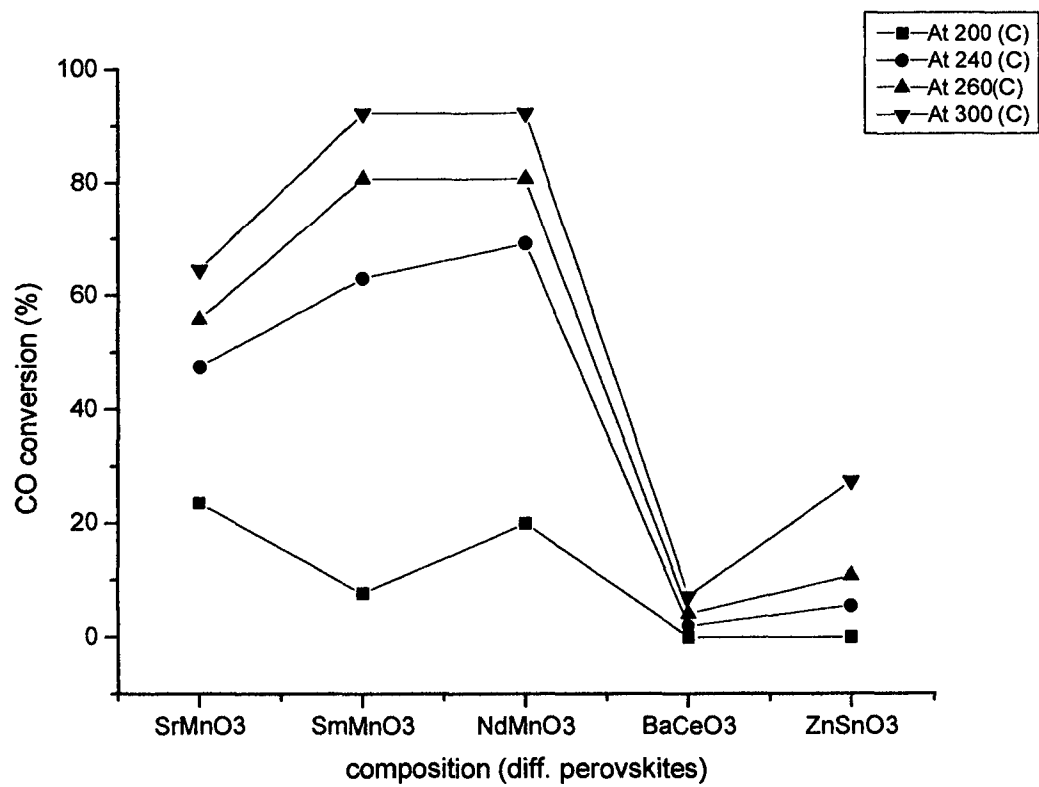
Fig. 5.7 CO conversion as a function of catalyst composition
for the system AMnO₃, BaCeO₃ and ZnSnO₃
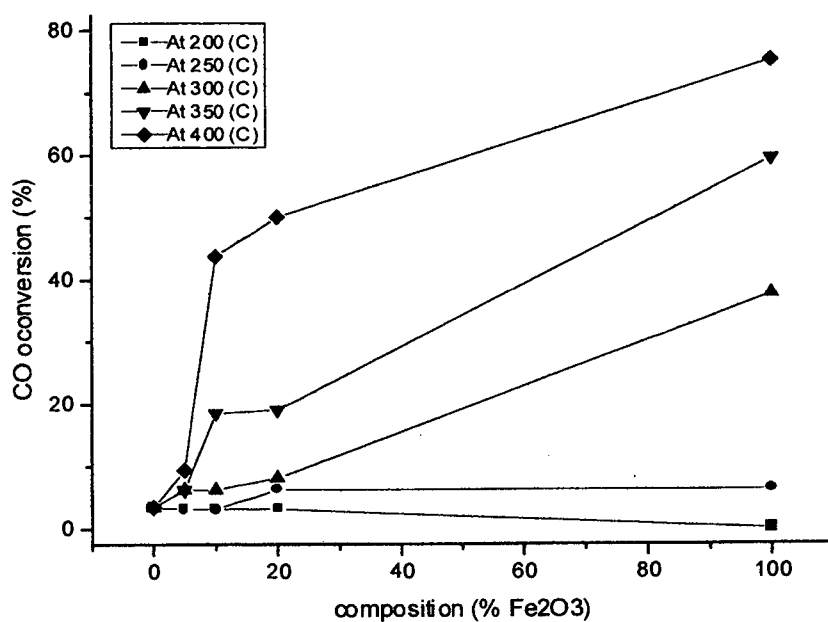
Fig. 5.8 (a) Conversion as a function of Fe_2O_3 in ZnO
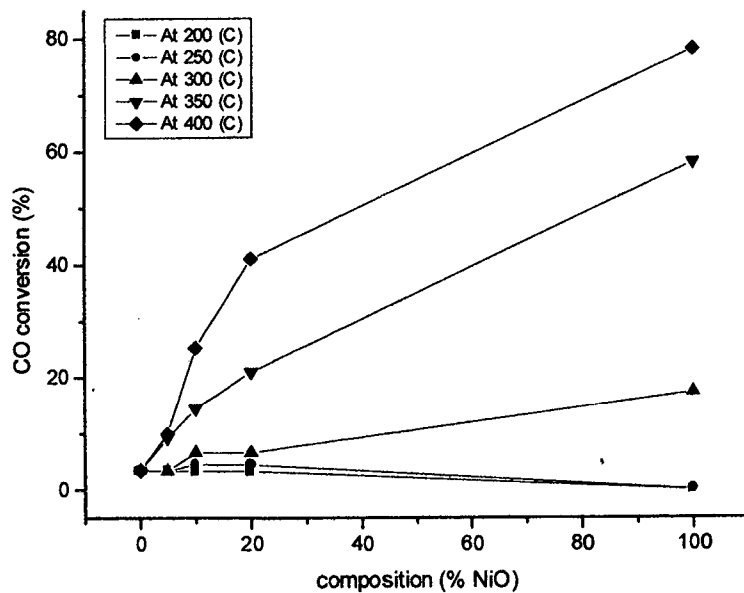
Fig. 5.8 (b) CO conversion as a function of NiO in ZnO

The catalytic activity of all these manganites increases with the increase in temperature from 200 to 300°C. At the lower temperatures of 200 and 240°C, the activity of $NdMnO_3$ is slightly higher than that of $SmMnO_3$. This is due to the distortion in the orthorhombic structure of $SmMnO_3$ because of the smaller Sm ion. However, at the higher temperatures of 260 and 300°C both these manganites have almost same activity. At all these temperatures, $BaCeO_3$ and $ZnSnO_3$ show low activity which is because of the low reducibility of Ce^{4+} and Sn^{4+} ions in these compounds.

In series III and IV the trend of variation of catalytic activity is similar. The substrate ZnO has low activity at all the temperatures. At low temperatures both Fe_2O_3 and NiO has low activity. But at higher temperatures the activity of these compounds increases. Therefore at higher temperatures at above of 300°C the activity of the compositions increases with the increase in the concentrations of Fe_2O_3 and NiO.

5.5 STUDY OF NUMBER OF CO OXIDATION CYCLES

Some of the catalysts were repeatedly used to carry out the CO oxidation reaction over a range of temperatures with a break of one day between each cycle. The comparison of the activities in the different cycles at the respective temperatures of a representative catalyst ($NiMnO_3$) is shown in figures 5.9 and 5.10. Almost same activity in different trials is observed at the corresponding temperatures for $NiMnO_3$ composition.

130
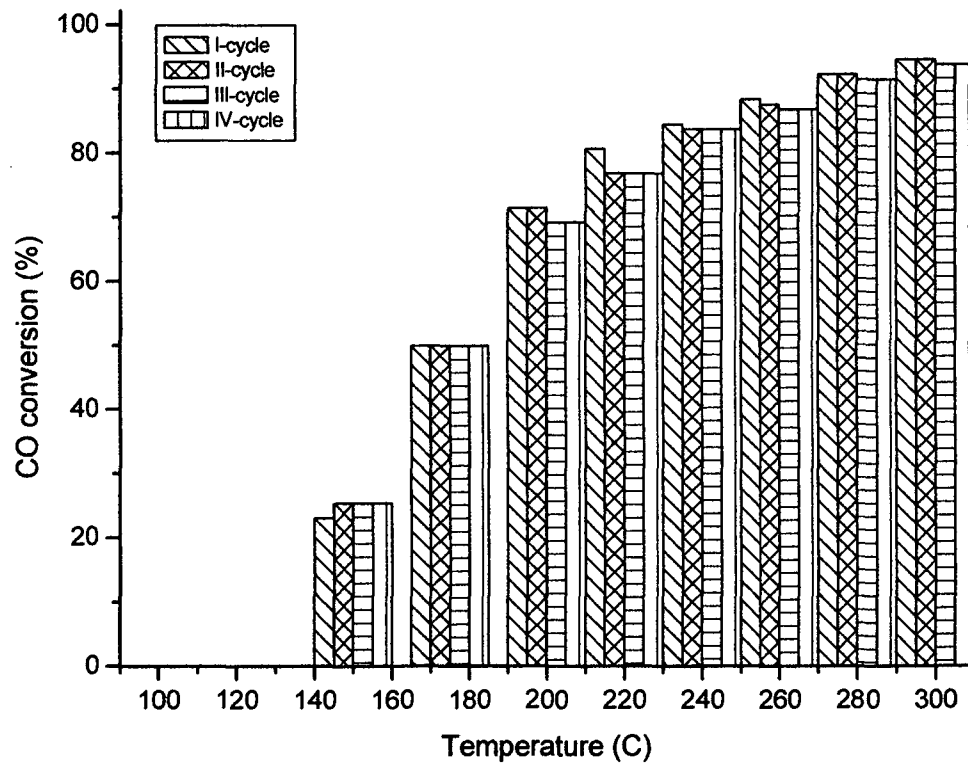
Fig. 5.9 Comparison of CO conversions as a function of temperature in diff. cycles over the catalyst NiMnO₃
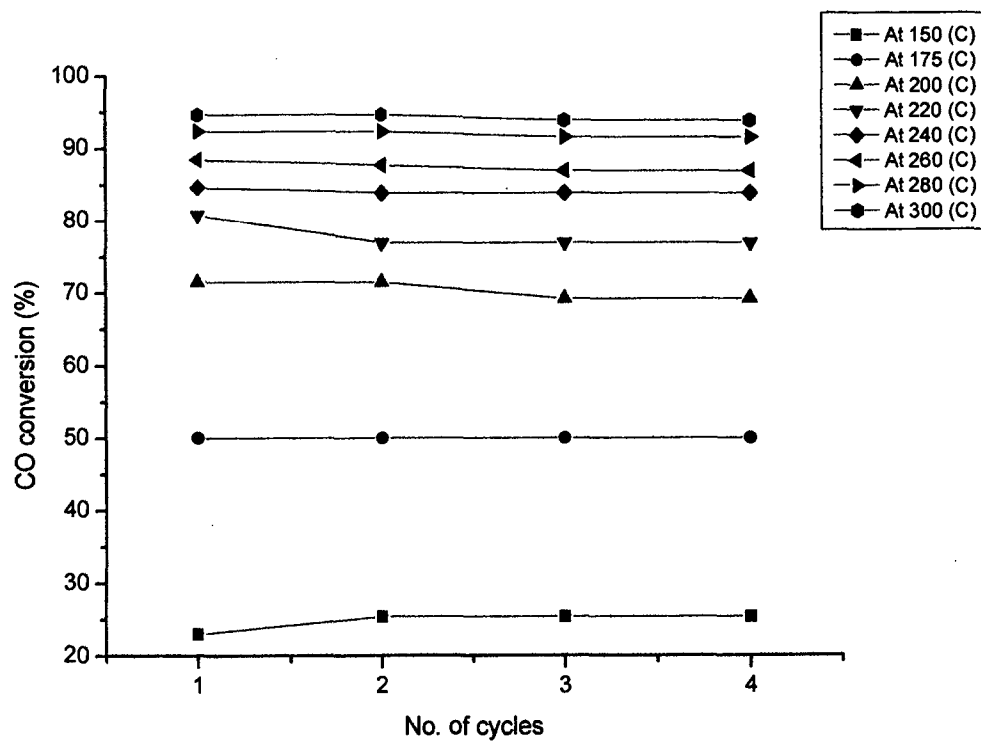
Fig. 5.10 Comparison of CO conversions as a function of
temperature in diff. cycles over the catalyst NiMnO₃

Thus, the different catalysts prepared show good stability over repeated cycles.

5.6 STUDY OF CATALYST LIFE

Catalysts life was attempted to be studied by subjecting some of the catalysts to the CO oxidation reaction at certain temperature for considerable period of about 14 h. Fig. 5.11 shows CO conversion as a function of time for the catalysts $Zn_{0.8}Ni_{0.2}MnO_3$ and $Zn_{0.6}Ni_{0.4}MnO_3$ at the temperature of 225°C. It is observed that initially activity slowly increases for a period of about 1.5 h. From this time onwards the activity almost remains constant toward the end of the period i.e. 14 h. The initial increase in activity may be reflecting the induction time for the attainment of the total activity. The consistency in activity suggests that the catalysts have good life.

From the preceding catalytic CO oxidation studies of the different compositions prepared, it can be concluded that all these compounds show good catalyzing action towards the CO oxidation reaction. In series-I catalysts of Zinc manganites, with the substitution of zinc at A-site by nickel, initially with Ni = 0.2 and 0.4 catalytic activity enhances whereas with the further increase of Ni to 0.6 and 0.8 the activity declines. However, $NiMnO_3$ shows the maximum activity. The manganites of series- II catalysts are found to have very high catalytic activity. $BaCeO_3$ and $ZnSnO_3$ compounds of this series show comparatively lower activity. The substrate ZnO of the supported metal oxide compositions though have poor catalytic activity, the supported metal oxide compositions show better activity.
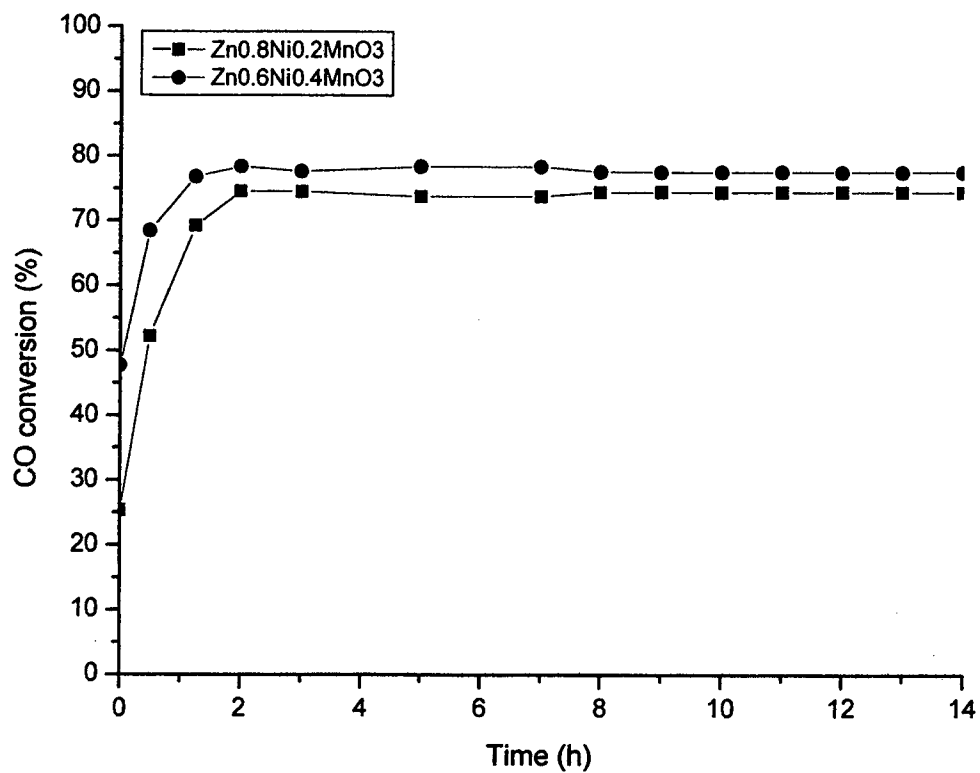
Fig. 5.11 CO conversion as a function of time at 225 °C for the catalysts $Zn_{0.8}Ni_{0.2}MnO_3$ and $Zn_{0.6}Ni_{0.4}MnO_3$

From the study of number of CO oxidation cycles over the catalysts, the catalysts are observed to be stable. The CO oxidation reaction on the catalysts for studying the life showed good and stable activity during the period of study.

CHAPTER 6

CONCLUSION

CONCLUSION

Transition metal oxides (TMO) are well known for their solid state and catalytic properties. However, their mixed oxides of perovskite type compounds are much more active and exhibit better properties with the well-defined bulk structures. Hence these mixed oxides occupy a prominent place in material science and catalysis. Perovskites show the possibility of varying the dimensions by substituting A-site or B-site or both the sites ions with foreign metal ions which make them to behave as chemical chameleons.

In this investigations, the perovskites and supported transition metal oxides prepared by wet co-precipitation and combustion techniques were studied with an aim to correlate their solid-state and catalytic properties.

X-ray studies confirmed that all the prepared perovskite samples are monophasic and well crystalline forms. The XRD patterns reveal that $ZnMnO_3$ is cubic, $NiMnO_3$ is rhombohedral and intermediate compositions showed finger print match with the end compounds. $SmMnO_3$, $NdMnO_3$ and $BaCeO_3$ have orthorhombic structures where as $SrMnO_3$ has hexagonal geometry.

SEM micrographs of the samples showed that the average particle size of the compositions prepared by co-precipitation technique is 80 - 100 nm where as that is

for the compositions prepared by combustion method is 110 - 130 nm. Perovskite samples prepared by hydroxide precursor technique possess considerably better surface areas, as high as 20.9 m^2/g. In these compositions, the surface area is found to influence the catalytic activity directly or indirectly. Comparatively, compositions prepared by combustion method have lower surface area. However, the catalytic activity of these compositions can not be directly correlated with their surface areas. Further, the compounds prepared by wet co-precipitation method showed low tendency towards agglomeration of particles than that prepared by combustion method.

Band gap energy of all the manganite perovskites is found to be low and these perovskites showed higher catalytic activity. The perovskites $BaCeO_3$ and $ZnSnO_3$ having higher band gap energy showed lower catalytic activity. Thus the lower band gap energy of the compositions can be related to their higher activity.

The FTIR study was an important tool in the characterization of the perovskites. It revealed the gradual changes taking place in the crystal structure with the A-site substitution and the resultant metal-oxygen bond covalency. In the $Zn_{1-x}Ni_xMnO_3$ system, with the increase in nickel in the lattice, the Mn-O bond becomes longer and weaker as shown by the gradual shifting of MnO_6 band to the lower frequency. The spectra of $NiMnO_3$ shows that Zn-O covalency in this composition is substituted by Ni-O covalency. A similar explanation holds good for the other compositions.

Thermal studies carried out on the hydroxide precursors for their decomposition behavior revealed that overall decomposition pattern is similar with three distinct steps. The precursor losses moisture at 80 -110°C which is followed by the decomposition of hydroxides to the corresponding oxides at around 300°C. Finally, the solid state diffusion initiates at about 300°C and perovskite is formed at 750 - 800°C.

The electrical resistivity measurements of the catalysts showed linear decrease in resistivity with the increasing temperature. The compounds are found to have the resistivity in the range 10^2 - 10^{10} Ωcm at temperatures from 400 to 30°C. Thus the compounds are typical semiconductors. The lower catalytic activity of some of the compositions like $BaCeO_3$ and $ZnSnO_3$ may be because of their higher electrical resistivity.

Among the compositions prepared, $NiMnO_3$ and NiO are magnetic, $BaCeO_3$, $ZnSnO_3$ and ZnO are diamagnetic where as all other compositions are paramagnetic in nature. It can be said that in diamagnetic samples, the redox potentials due to ion pairs are low which may also affect the catalytic activity. In Fe_2O_3/ZnO series, magnetic susceptibility of the compositions gradually increases with the increase in Fe_2O_3 content in the compositions. Similar changes in magnetic susceptibility of NiO/ZnO series compositions are also observed.

From the ESR study of the perovskites, it can be inferred that the prepared manganites are ESR active. In the series $Zn_{1-x}Ni_xMnO_3$, the inclusion of lower concentration of Ni in the compositions, does not add to the ESR signal. But the

higher concentration of Ni enhances the ESR signal in the manganites. Heavy rare earth ions at A site in the perovskites broadens the ESR line-widths.

The catalytic activity for CO oxidation of $Zn_{1-x}Ni_xMnO_3$ compositions is observed to increase significantly at the initial Ni concentration from 0.2 to 0.4. With the further increase of Ni concentration to 0.6 and 0.8, the catalytic activity falls. The $NiMnO_3$ shows very high catalytic activity. The observed trend of activity is linked with the covalency of metal oxygen bond, the change in crystal structure and the change in the ion pairs redox potentials. $SrMnO_3$, $SmMnO_3$ and $NdMnO_3$ are good CO oxidation catalysts. The difference in the catalytic activity of these catalysts is explained on the basis of the differences in their crystal structures. The low activity of $BaCeO_3$ and $ZnSnO_3$ is correlated to the low reducibility of Ce^{4+} and Sn^{4+} ions. For the supported transition metal oxide series compositions, the catalytic activity increases with the increase in the concentration of transition metal oxide.

Number of CO oxidation reaction cycles study showed that the catalyst prepared have good stability. The consistency in activity observed during the study of catalyst life reveal that the catalysts have good life. From the experimental data, it may be said that Langmuir-Hinshellwood type mechanism for CO oxidation over different perovskites is predominant, which proceeds via carbonyl formation as explained by molecular orbital theory.

It is concluded that to design a catalyst for the abatement of automobile and industrial pollution, for the replacement of conventional noble metal catalysts by oxide catalysts, which is economical, thermally stable and equally efficient, the

following strategies are to be considered. (1) Selecting the B- site element which principally determines the catalytic activity, (2) control of valency and vacancy by selection of A-site element including partial substitution, (3) considering the synergistic effects of constituting elements, mainly B-site transition element and (4) enhancement of surface area by forming fine particles or dispersing on supports.

REFERENCES

1. C.N.R. Rao and B. Raveau, Transition Metal Oxides, 2nd edn., Wiley VCH, New York, (1998).

2. C.N.R. Rao, J. Mater. Chem., 9 (1999) 1.

3. W.F. Libby, Science, 171 (1971) 499.

4. R.J.H. Voorhoeve, J.P. Remeika and D.W. Johnson, Science, 180 (1973) 62.

5. M. Tsujimura, T. Furusava, and D. Kunni, Chem. Eng. Japan, 16 (1983) 132.

6. A.V. Salker, Indian J. Chem., A 40 (2001) 863.

7. L. Laitao, S. Guangxin and D. Zhanhui, Indian J. Chem., A 44 (2005) 1388.

8. Idem Ibid, 51 (1966) 301.

9. A.K. Neyestanaki and L.E. Lindfors, Combust. Sci. Tenhnol., 97 (1994) 121.

10. F. Severin and J. Laine, Proc. 1st Eur. Cong. Catal. Europacat 1, Mountphellier, 2 (1993) 639.

11. V. Mathieu-Determince, J.B. Maggy and J. Verbust, Proc. 1st Eur. Cong. Catal. Europacat 1, Mountphellier, 2 (1993) 789.

12. G. Parravano, Chem. Phys., 20 (1952) 342.

13. R.J.H. Voorhoeve, Adv. Mater. Catal., Chapt. 5, Academic Press, New York, (1977).

14. A. Reller and T. William, Chem. Brit., 25 (1989) 1227.

15. L.G. Tejuca, J.L.G. Fierro and J.M.D. Tascon, Adv. Catal., 36 (1989) 237.

16. T. Nitadori, S. Kurihara and M. Misono, J. Catal., 9 (1967) 38.

17. S. Katz, J.J. Croat and J.V. Laukonia, Ind. Eng. Chem., Prod. Res. Dev., 14 (1975) 274.

18. H. Katzman, L. Pandolfi, L.A. Pedderson and W.F. Libby, Chemteck, (1976) 369.

19. F.F. Wolkenstein, Electronic theory of catalysis on semiconductors, Pergamon Press, Oxford, (1953).

20. A.B. Hart and R.A. Ross, J. Catal. 2 (1963) 251.

21. F.S. Stone, Adv. Catal., 13 (1962) 35.

22. M.D. Lee, T.R. Ling and Z.B. Chen, Appl. Catal., A: 136(2) (1996) 191.

23. D. Klissurski and V. Rives, Appl. Catal. A 109(1) (1994) 1.

24. J. Li, T. He, J. Wang and K. Pan, J. Electron. Spectro. Rel. Phenomena, 42(4) (1987) 293.

25. E.J. Baran, Catalysis Today, 8 (1990) 133.

26. R. Mahesh, K.R. Kannan and C.N.R. Rao, J. Solid State Chem., 114 (1995) 294.

27. R. Mahesh, R. Mahendiran A.K. Raichaudhuri and C.N.R. Rao, Solid State Ionics, 102 (1997) 559.

28. R.J. Bell, G.J. Millar and J. Drennan, J. Solid State Ionics, 131 (2000) 211.

29. T. Ahmad, K.V. Ramanujachary, S.E. Lofland and A.K. Ganguli, J. Chem. Sci., 118(6) (2006) 513.

30. F.S. Galasso, Structure, Properties and Preparation of Perovskite Type Compounds, Pergamon press, Oxford, (1969).

31. R.S. Roth, J. Res. Natl. Bur. Stand., 58 (1957) 75.

32. J.B. Goodenough and J.M. Longo, Zahlen.und Funkt. aus Naturw.und Tech., New Series, Grp. III 4 (1970) 126.

33. N. Ramdass, Mater. Sci. Eng., 36 (1978) 231.

34. O. Fukunaga and T. Fujita, J. Solid State Chem., 8 (1973) 331.

35. A.F. Wells, Structural Inorganic Chemistry, 5th Ed., Clarendon Press, Oxford, (1984).

36. O. Muller and R. Roy, The Major Ternary Structural Families, Springer, Berlin-Heidelberg, New York (1974).

37. Y. J. Mergler, A.V. Aalst, J.V. Delft and B. E. Nieuwenhuys, Appl. Catal. B: Environmental 10 (1996) 245.

38. Y.Y. Yao and J.T. Kummer, J. Catal., 28 (1973) 124.

39. V. Shapovalov and H. Metiu, J. Catal., 245 (2007) 205.

40. H.D. Megaw, Proc. Phys. Soc., 58 (1946) 325.

41. P.D. Battle, T.C. Gibb and C.W. Jones, J. Solid State Chem., 74 (1988) 60.

42. P. Norby, I.G.K. Anderson and E.K. Anderson, J. Solid State Chem., 110 (1995) 191.

43. A. Wold and R.J. Arnott, J. Phys. Chem. Solids., 9 (1959) 176.

44. S. Geller, Acta Crystallogr., 10 (1957) 243.

45. C.N.R. Rao and J. Gopalakrishnan, New Directions in Solid State Chemistry, Cambridge Univ. Press, Cambridge (1986).

46. S. Geller, Acta Crystallogr., 9 (1956) 1019.

47. S. Geller and E.A. Wood Acta Crystallogr., 9 (1956) 563.

48. P.M. Raccah and J.B. Goodenough, Phys. Rev., 155 (1967) 932.

49. M. Marezio, J.P. Remeika and P.D. Dernier, Acta Crystallogr., B 26 (1970) 2008.

50. G. Demazeau, A. Marbeuf, M. Pouchard and P. Hagenmuller, J. Sold State Chem., 3 (1971) 582.

51. A. Baiker, P.E. Marti, P. Keusch and A.J. Reller, J. Catal., 146 (1994) 268.

52. H. Obayanshi and T. Kudo, Denki Kagaku, 44 (1976) 503.

53. V.M. Goldschmidt, Skrifter Norske Videnskaps-Akad. Oslo. I. MatheMater. Naturwiss. Klass No. 8 (1926).

54. J.K. Vassiliou, M. Hornbostel and F.J. Disalvo, J. Solid State Chem., 81 (1989) 208.

55. P. Lacorre, J.B. Torrance and T.C. Huang, J. Solid State Chem., 91 (1991) 225.

56. J.L. Garcia- Munoz, J. Rodriguez-Carvajal, P. Lacorre and J.B. Torrance, Phys. Rev. B 46(8) (1992) 4414.

57. J.A. Alonso, M.J. Martinez-Lope and I. Rasines, J. Solid State State Chem., 120 (1995) 170.

58. J. Tofter and J.B. Goodenough, Chem. Mater., 9 (1997) 1467.

59. Z. El-Fadli, M.R. Metni, F. Sapina and A.J. Beltran, Mater. Chem., 10 (2000) 437.

60. Jr. Yakel and L. Harry, Acta Crystallogr., 8 (1955) 394.

61. S. Geller, Acta Crystallogr., 10 (1957) 248.

62. M. Suzuki, H. Inaba and H. Hayashi, Solid State Ionics, 144(1) (2001) 99.

63. E.O. Wollen and W.C. Koehler, Phys. Rev., 100 (1955) 545.

64. M.H. Whangbo, J.H. Koo and M. Pouchard, Inorg. Chem., 41(7) (2002) 1920.

65. J.B. Goodenough, Phys. Rev., 100 (1955) 564.

66. J.B. Goodenough and P.M. Raccah, J. App. Phys., 36(3) (1965) 1030.

67. J.H. Kuo and H.U. Anderson, J. Solid State Chem., 83 (1989) 52.

68. L.A. Isupova, V.A. Sadykov, V.P. Ivanov and O.F. Kononchuk, React. Kinet. Catal. Lett., 53(1) (1994) 223.

69. J. Tofter and J.B. Goodenough, Solid State Ionics, 103 (1997) 1215.

70. P.K. Gallagher, D.W. Jr. Johnson And F. Schrey, Mater. Res. Bull., 9 (1974) 1345.

71. R.J.H. Voorhoeve, J.P. Remeika, F.J. Disalvo and P.K. Gallagher, J. Solid State Chem., 14 (1975) 395.

72. G.J. McCarthy, P.V. Gallagher and C. Sipe, Mater. Res. Bull., 8 (1973) 1277.

73. S. Gonen, J. Gopalakrishnan and B.W. Eichhoru, Solid State Sciences, 4(6) (2002) 773.

74. M.E. Jorge, A.C.D. Santos and N.R. Nunes, Intl. J. Inorg. Mater., 3(7) (2001) 915.

75. T. Nakamura, Z. Petzow and L.J. Gauckler, Mater. Res. Bull., 14 (1979) 649.

76. K. Sreedhar, J.M. Honig, M. Darwin and J. Spalek, Phys. Rev., B, 46(10) (1992) 6382.

77. J. Blasco, M. Castro and J. Garcia, J. Phys: Condens. Matter, 6 (1994) 5875.

78. D.D. Sharma, N. Shanti, S.R. Barman and P. Mahadevan, J. Solid State Chem., 124 (1995) 285.

79. J.B. Goodenough, J. Solid State Chem., 127 (1996) 126.

80. G. Thorton, B.C. Tofield and D.E. Williams, Solid State Commun., 44(8) (1982) 1213.

81. A. Barman, M. Ghosh, A. Das, S.K. De and S. Chatterjee, Indian J. Phys., A, 71(5) (1997) 517.

82. Z. Yang, L. Ye and X. Xide, Phys. Rev. B., 59(10) (1999) 7051.

83. M.L. Medarde, J. Phys: Condens. Matter., 9 (1997) 1679.

84. J.B. Goodenough, Mater. Res. Bull., 6 (1971) 967.

85. V.G. Bhide, D.S. Rajoria, G. Rama Rao and C.N.R. Rao, Phys. Rev. B., 6(3) (1972) 1021.

86. H. Watanabe, J. Phy. Soc. Jpn., 16 (1961) 433.

87. C.N.R. Rao, Om Prakash and P. Ganguly, J. Solid State Chem., 15 (1975) 186.

88. J.B. Goodenough, A. Wold, R.J. Arnott and N. Menyuk, Phys. Rev., 124 (1961) 373.

89. G.H. Jonker, J. Appl. Phys., 37 (1966) 1424.

90. X.Q. Xu, J.L. Peng and R.L. Greene, Phys. Rev. B., 48 (1993) 1112.

91. J. Blasco, M. Castro and J. Garcia, J. Phys: Condens. Matter, 6 (1994) 10759.

92. J.L. Garcia-Munoz, J. Rodriguez-Carvajal and P. Lacorre, Europhys. Lett., 20 (1992) 241.

93. S. Quezel-Ambrunaz, Bull. Soc. Fr. Min. Cristallogr., 91 (1968) 339.

94. S. Rosenkranz, LNS Report., Zurich (1992) 165.

95. M. Couzi and P.V. Huong, J. Chem. Phys., 69 (1972) 1339.

96. M. Couzi and P.V. Huong, Ann. Chim., 9 (1974) 19.

97. E.J. Baran, J. Naturforsch, B 30 (1975) 136.

98. P. Alain and B. Pirion, C. R. Acad. Sc. Paris, 270 (1970) 1687.

99. P. Alain, J.P. Coutures and B. Pirion, Phys. Stat. Sol., 43 (1971) 669.

100. M.C. Sain, E. Husson and H. Brusset, Spectrochim. Acta., A 37(11) (1981) 985.

101. D.D. Agarwal, React. Kin. Cat. Lett., 53(2) (1994) 441.

102. K. Li, R. Cheng, S. Wang and Y. Zhang, J. Phys: Condens. Matter, 10 (1998) 4315.

103. P. Ganguly and N.Y. Vasanthacharya, J. Solid State Chem., 61 (1986)164.

104. G.V. Subharao, Appl. Spectrose., 24 (1970) 436.

105. J.T. Last, Phys. Rev. 105 (1970) 1740.

106. A.P. Lane, D.W.A. Sharp, D.H. Brown and D.A. Paterson, J. Chem. Soc., A (1971) 94.

107. C.H. Perry, J. Appl. Phys., 4(1) (1665) 564.

108. E.J. Baran and I.L. Botto, Inorg. Allg. Chem. 465 (1980) 186.

109. K.K. Singh, P. Ganguly and J.B. Goodenough, J. Solid State Chem., 52 (1984) 254.

110. K.K. Singh and P. Ganguly, Spectrochim. Acta., A 40 (1981) 539.

111. N. Ogita, M. Udgawa and K. ohbayashi, J. Phy. Soc. Jpn., 57 (1988) 3932.

112. V.I. Savchenko, Russ. Chem. Rev., 55 (1986) 222.

113. S. Rajadurai and J.J. Carberry, Proc. Faraday Discus., No. 87 (1989).

114. T. Jin, T. Okuhara, G.J. Mains and J.M. White, J. Phys. Chem., 91 (1987) 3310.

115. C. Sung-Ho, P. Jong-Soo, C. Seung-Hoon and K. Sung-Hyun, J. Power Sources 156 (2006) 260.

116. K.H. Kim, S.H. Lee, Y.R. Kim and J.S. Choi, J. Catal., 88 (1984) 283.

117. L. Meng-Fei, Z. Xiao-Ming and Z. Yi-Jun, Indian J. Chem., A 38 (1999) 703.

118. S.G. Gagarin and M.O. Rozovskii, Kinet. Catal., 24 (1983) 1126.

119. V. Indoniva, A. Cimino and F. Pepe. Acta Sim. Ieoram Catal., 9th 2   (1988) 846.

120. M. Kobayashi, T. Kanno and J. Kimura, J. Chem. Soc. Fara. Trans., 1(84) (1988) 2099.

121. S.F. Jen and A.B. Anderson, Surf. Science, 223 (1989) 119.

122. T.J. Huang and T.C. Yu, Appl. Catal., 71 (1991) 275.

123. K.I. Kapteijn, S. Stegenga and J.A. Moulijn, Catal. Today, 16 (1993) 273.

124. R.K. Hertz, A. Badlani, D.R. Schryer and B.T. Upchurch, J. Catal.141 (1993) 219.

125. J. Szanyi and D.W. Goodman, Catal. Lett., 21 (1993) 165.

126. G.G. Jernigan and G.A. Somorjai, J. Catal., 147 (1994) 567.

127. F. Boccuzi, A. Chiorino, S. Tsubota and M. Haruta, Catal. Lett., 29 (1994) 225.

128. Y.J. Mergler, Rh-free automotive catalysts, Proefschrift., 5 (1995) 50.

129. G.B. Hoflund, in 'Catalysis:Modern Trends', N.M. Gupta and D.K. Chakrabarty Eds., Narosa Pub. House, New Delhi, (1995).

130. S.M. Gurav and A.V. Salker, Indian J. Chem. Tech., 5 (1998) 286.

131. S.M. Gurav and A.V. Salker, J. Mater. Sci., 35 (2000) 4713.

132. G. Blyholder, J. Phys. Chem., 68 (1964) 2772.

133. P. Politzer and S.D. Kaster, Surface Sci., 36 (1973) 186.

134. V.F. Kiselev and O.V. Krylov in 'Adsorption and Catalysis on transition metals and their oxides' (Robert Gomes Ed.) Springer Verlag, Springer series of surf. Sci., 9 (1989) 230.

135. L.H. Little, IR Spectra of Adsorbed Species, Academic Press, New York, (1966).

136. J.W. London and A.T. Bell, J. Catal., 31 (1973) 32.

137. W. Hertl, J. Catal., 31 (1973) 232.

138. H.G. Tompkins and R.G. Greenler, Surf. Sci., 28 (1971) 194.

139. J.B. Peri, J. Phys.Chem., 78 (1974) 588.

140. S.Z. Roginskii, Acta. Physico. Chem., USSR, 9 (1938) 475.

141. W.E. Garner and F.J. Veal, J. Chem. Soc., (1935) 1487.

142. E.D. Pierron, J.A. Raskin and J.P. Roth, J. Catal., 9 (1967) 38.

143. E.R.S. Winter, Adv. Catal., 10 (1958) 196.

144. K. Hirota, Y. Kera and S. Teratum, J. Phys. Chem., 72 (1968) 133.

145. M.F. Hughest and G.P. Hill, J. Phys. Chem., 59 (1955) 388.

146. V.I. Marshneva, G.K. Boreskov and V.D. Sokolovskii, Kinet. Catal., 13 (1972) 1209.

147. F.S. Stone, Adv. Catal., 13 (1962) 1.

148. W.E. Garner, T.J. Gray and F.S. Stone, Disc. Faraday Soc. 8 (1950) 246.

149. W.E. Garner, T.J. Gray and F.S. Stone, Proc. Royal Soc., (London), A 211(1952) 472.

150. R.M. Dell and F.S. Stone, Trans. Faraday Soc., 50 (1954) 50.

151. R. Rudham and F.S. Stone, Chemisorption, Proc. Chem. Soc. Sympo., 1956 (W.E. Garner eds) Academic Press, New York, (1957) 205.

152. G. Blyholder, Proc. 3rd Int. Cong. Catal., North Holland Publish. Co., (1964).

153. W. Hartal and R.J. Ferrauto, Catal., 29 (1973) 352.

154. W.J. Morgan and R.J. Ferrauto, J. Catal., 31 (1973) 140.

155. W.F. Libby, Science, 171 (1983) 499.

156. L.A. Pedersen and W.F. Libby, Science, 176 (1972) 1355.

157. H. Arai, T. Yamada and T. Seiyama, Appl. Catal., 26 (1986) 265.

158. T. Seiyama, N. Yamazoe and K. Yuguchi, Ind. Eng. Chem., Prod. Res. Dev., 24 (1985) 19.

159. M. Misono and T. Nitadori, Adsorption and Catalysis on Oxide Surfaces, (Che and Bond eds.) Elsevier, Amsterdam, (1985).

160. T. Nitadori and M. Misono, J. Catal., 93 (1985) 459.

161. T. Nitadori, S. Kurihara and M. Misono, J. Catal., 98 (1986) 221.

162. J.L.G. Fierro, Catal. Today, 8 (1990) 153.

163. R.J.H. Voorhoeve, J.P. Remeika and L.E. Trimble, Ann. N. Y. Acad. Sci., 272 (1976) 3.

164. G. Parravano, J. Am. Chem. Soc., 75 (1953) 1497.

165. D.W. Meadowcroft, Nature, 226 (1970) 847.

166. R.J.H. Voorhoeve, J.P. Remeika and P.K. Gallagher, Science, 195 (1977) 827.

167. D.Y. Rao and D.K. Chakrabarty, Indian J. Chem., A 23 (1984) 375.

168. B. Vishwanathan and S.S. George, Indian J. Techn., 22 (1984) 388.

169. P.K. Gallagher, D.W. Johnson and E.M. Vogel, J. Am. Ceram. Soc., 60 (1977) 28.

170. Om Parkash, C.N.R. Rao and P. Ganguly, Mater. Res. Bull., 9 (1974) 1173.

171. N. Gunasekaran, A. Meenakshisundaram and V. Srinivasan, Surf. Tech. 22 (1984) 89.

172. D.Y. Rao and D.K. Chakrabarty, React. Kinet. Catal. Lett., 33 (1987) 131.

173. R.G. Shetkar and A.V. Salker, Proc. Intl. Symp. Mater. Chem., BARC-Mumbai, (2006) 586-588.

174. A.V. Salker, D.K. Chakrabarty and H.V. Keer, Indian J. Chem., A 28 (1989) 458.

175. A.V. Salker and T. Vaz, Indian J. Chem., A 43 (2004) 710.

176. K.S. Chan, J. Ma and G.K. Chuah, Appl. Catal., A 107 (1994) 1.

177. S. Jaenicke, G.K. Chuah and J.Y. Lee, Environ. Monit. Assess, 19(1) (1991) 131.

178. T. Shimizu, The Chemical Soc. Japan, Chem. Lett., 1 (1980).

179. R. Hildrum, Aasland and Ø Jahannesen, Solid State Ionics,66 (1993) 208.

180. L. Sebastian, A.K. Shukla and J. Gopalakrishnan, Bull. Mater. Sci., 23(3) (2000) 169.

181. P. Salomonsson, T. Griffin and B. Kasemo, Appl. Catal., A: General, 104 (1993) 175.

182. G.M. Pajonk, Heterogeneous Chem. Reviews, 2 (1995) 129.

183. Y.X. Chen, L.P. Lou, X.Y. Ziang, R.X. Chou and X.M. Zheng, Indian J. Chem., A 42 (2003) 460.

184. J. Kingsley and K.C. Patil, Mater. Lett., 6(11,12) (1988) 427.

185. G. Kremenic, J.M.L. Nieto, J.M.D. Tascon and L.G. Tejuca, J. Chem. Soc. Faraday Trans., 81 (1985) 939.

186. T.L. Nguyen, M. Dokiya, S. Wang, H. Tagawa and T. Hashimoto, Solid State Ionics, 130 (2000) 230.

187. V. Samuel, A.B. Gaikwad and V. Ravi, Bull. Mater. Sci., 29(2) (2006) 123.

188. M.T. Weller, Inorg. Mater. Chem., Oxford University Press, (1994).

189. M.T. Escote, A.M.L. da Silva and R.F. Jardian, J. Solid State Chem., 151 (2000) 298.

190. S.D. Likhite, C. Radhakrishnamurthy and Sahasrabudhe, Rev. Sci. Instr., 25 (1965) 302.

191. B.L. Chamberland, A.W. Sleight and J.F. Weiher, J. Solid State Chem.,   1 (1970) 506.

192. Whittingham, S. and Sunny, ICDD Grant-in aid, (1997).

193. Feltz, A., Topfer and J., J. Alloys Compds., 196 (1993) 75.

194. T. Negas, and R.S. Roth, Solid State Chem., 1 (1970) 409.

195. E.J.W. Verwey, P.B. Braun, E.W. Gorter, F.C. Romeijn and J.H. Van Santen, Z. Phys. Chem., 198 (1951) 6.

196. A.P.B. Sinha, N.R. Sanjana and A.B. Biswas, J. Phys. Chem., 62 (1958) 191.

197. C.D. Sabane, A.P.B. Sinha and A.B. Biswas, Indian J. Pure Appl. Phys.,   4 (1966) 187.

198. J.B. Goodenough, J. Phys. Radium, Paris, 20 (1959) 155.

199. A.P.B. Sinha and K.P. Sinha, Indian J. Pure Appl. Phys., 1 (1963) 286.

200. D.B. Ghare, A.P.B. Sinha and A.L. Singh, J. Mater. Sci., 3 (1968) 389.

201. G.H. Jonker and J.H. Van Santen, Physica XIX, (1953) 120.

202. G.H. Jonker, Physica XXII, (1956) 707.

203. K.M. Creer, I.G. Hedley and W.O. Reilly, Mag. Oxides Part 2, Edited by D.J. Craik, A Wiley-Interscience Publication, London, (1975) 664.

204. G.R. Rao and H.R. Sahu, Proc. Ind. Acad. Sci. (Chem. Sci.), 113(5,6) (2001) 651.

205. J.L.G. Fierro, J.M.D. Tascon and L.G. Tejuca, J. Catal., 89 (1984) 209.

206. J.L.G. Fierro, J.M.D. Tascon and L.G. Tejuca, J. Solid State Chem., (1984) 83.

207. R.J.H. Voorhoeve, J.P. Remeika and L.E. Trimble, in 'The Catalytic Chemistry of Nitrogen Oxide' Plenum, New York, (1975).

208. B. Vishwanathan, Catal. Rev.-Sci. Eng., 34(4) (1992) 337.

209. J.M.D. Tascon and L.G. Tejuca, Z. Phys. Chem. N. F., 121 (1980) 63.

210. J.M.D. Tascon and L.G. Tejuca, Z. Phys. Chem. N.F., 121 (1980) 79.

211. J.M.D. Tascon, J.L.G. Fierro and L.G. Tejuca, Z. Phys. Chem., 124 (1981) 249.

212. Wolfram, T., E.A. Kraut and F.J. Morin, Phys. Rev., B7 (1973) 1677.

213. T. Seiyama, Catal. Rev.-Sci. Eng., 34(4) (1992) 281.

214. D. Mehandjiev, E. Zhecheva, G. Ivanov and R. Ioncheva, Appl. Catal. A: General 167 (1998) 277.

215. K.J. Haralambous, Z. Loizos and N. Spyrellis, Mater. Letters, 11(3,4) (1991) 133.

216. K. Kuroda, N. Ishizawa, N. Mizutani and M. Kato, J. Solid State Chem., 38 (1981) 297.

217. T.K. Varadarajan, R. Sumathi and B. Vishwanathan, Indian J. Chem., A 40 (2001) 1033.

APPENDIX – I

Publications

1. Preparation, Characterization and Catalytic CO oxidation Studies over Sr, Nd and Sm Manganites

   R.G. Shetkar and A.V. Salker

   Proc. Intl. Symp. Mater. Chem., BARC – Mumbai (2006) 586 – 588.

2. Catalytic Oxidation of Carbon Monoxide over Fe_2O_3 supported on ZnO

   R.G. Shetkar and A.V. Salker

   Intl. Conf. Emerg. Trends in Chem. Sci., Mumbai University (2007) 53.

3. Solid state and Catalytic CO oxidation studies on $Zn_{1-x}Ni_xMnO_3$ system.

   R.G. Shetkar and A.V. Salker

   Mater. Chem. Phys. (2007) Accepted.

4. Electrical, Magnetic and Catalytic carbon monoxide oxidation studies over some perovskites prepared by combustion method.

   R.G. Shetkar and A.V. Salker

   J. Mater. Sci. Tech. (2007) communicated.

361

155